JGR Planets

RESEARCH ARTICLE
10.1029/2020JE006752

Large Eddy Simulations of the Dusty Martian Convective Boundary Layer With MarsWRF

Zhaopeng Wu[1,2], Mark I. Richardson[3], Xi Zhang[4], Jun Cui[1,2,5], Nicholas G. Heavens[6,7], Christopher Lee[3,8], Tao Li[2,9], Yuan Lian[3], Claire E. Newman[3], Alejandro Soto[10], Orkun Temel[11,12], Anthony D. Toigo[13], and Marcin Witek[14]

[1]School of Atmospheric Sciences, Planetary Environmental and Astrobiological Research Laboratory, Sun Yat-Sen University, Zhuhai, China, [2]CAS Center for Excellence in Comparative Planetology, Hefei, China, [3]Aeolis Research, Chandler, AZ, USA, [4]Department of Earth and Planetary Sciences, University of California Santa Cruz, Santa Cruz, CA, USA, [5]CAS Key Laboratory of Lunar and Deep Space Exploration, Chinese Academy of Sciences, National Astronomical Observatories, Beijing, China, [6]Space Science Institute, Boulder, CO, USA, [7]Department of Earth Science and Engineering, Imperial College, London, UK, [8]Department of Physics, University of Toronto, Toronto, ON, Canada, [9]CAS Key Laboratory of Geospace Environment, School of Earth and Space Sciences, University of Science and Technology of China, Hefei, China, [10]Southwest Research Institute, Boulder, CO, USA, [11]KU Leuven, Institute of Astronomy, Leuven, Belgium, [12]Royal Observatory of Belgium, Brussels, Belgium, [13]Johns Hopkins University Applied Physics Laboratory, Laurel, MD, USA, [14]Jet Propulsion Laboratory, Pasadena, CA, USA

Key Points:

- Dust radiative-dynamical feedback upon turbulent mixing in the Martian convective boundary layer is demonstrated by Large Eddy Simulation
- The destabilizing effect of dust lateral heating contrasts is found to augment convection and deepen the boundary layer
- Under some circumstances a positive feedback may exist between dust radiative heating, the intensity of boundary layer mixing, and dust lifting

Correspondence to:
Z. Wu,
wuzhp9@mail.sysu.edu.cn

Citation:
Wu, Z., Richardson, M. I., Zhang, X., Cui, J., Heavens, N. G., Lee, C., et al. (2021). Large eddy simulations of the dusty Martian convective boundary layer with MarsWRF. *Journal of Geophysical Research: Planets*, *126*, e2020JE006752. https://doi.org/10.1029/2020JE006752

Received 10 DEC 2020
Accepted 21 JUL 2021

Abstract Large eddy simulation (LES) of the Martian convective boundary layer (CBL) with a Mars-adapted version of the Weather Research and Forecasting model is used to examine the impact of aerosol dust radiative-dynamical feedbacks on turbulent mixing. The LES is validated against spacecraft observations and prior modeling. To study dust redistribution by coherent dynamical structures within the CBL, two radiatively active dust distribution scenarios are used: one in which the dust distribution remains fixed and another in which dust is freely transported by CBL motions. In the fixed dust scenario, increasing atmospheric dust loading shades the surface from sunlight and weakens convection. However, a competing effect emerges in the free dust scenario, resulting from the lateral concentration of dust in updrafts. The resulting enhancement of dust radiative heating in upwelling plumes both generates horizontal thermal contrasts in the CBL and increases buoyancy production, jointly enhancing CBL convection. We define a dust inhomogeneity index (DII) to quantify how much dust is concentrated in upwelling plumes. If the DII is large enough, the destabilizing effect of lateral heating contrasts can exceed the stabilizing effect of surface shading such that the CBL depth increases with increasing dust optical depth. Thus, under certain combinations of total dust optical depth and the lateral inhomogeneity of dust, a positive feedback exists between dust optical depth, the vigor and depth of CBL mixing, and—to the extent that dust lifting is controlled by the depth and vigor of CBL mixing—the further lifting of dust from the surface.

Plain Language Summary We use a very high-resolution atmospheric model (Mars-adapted version of the Weather Research and Forecasting model) to study the interaction between dust and turbulent motions at the bottom of the Martian atmosphere. The model is validated against satellite observations and previously validated model results. Two types of experiment are conducted to test the effect of the horizontal dust distribution. With horizontally uniform dust levels, increasing the total dust amount reduces solar heating reaching the surface and thus cools the surface and weakens upward motions. However, if the dust is allowed to move horizontally in the region, upward-moving air tends to concentrate the dust and these plumes hence become dustier than average. Dust contained in the upward plumes is then heated by the Sun, increasing the speed of upward motion. Thus, the stronger temperature differences may result in faster upward plumes as the amount of atmospheric dust increases. Stronger vertical plumes require stronger horizontal motions at the surface, due to mass conservation within a convection cell. These stronger surface winds may lead to greater dust lifting, and thus this study suggests that dust storms on Mars may grow in their early stages through a natural positive feedback between dust inhomogeneity, radiative heating, and accelerated winds.

1. Introduction

Suspended mineral aerosol dust provides a significant contribution to the meteorological and climatological forcing on Mars, due to the widespread availability of dust on the surface, the frequent occurrence of dust lifting events (due to surface wind stress, dust devils, or other processes), the relative inefficiency of dust deposition processes when little water is present, and the strong interaction of dust with both visible and thermal infrared radiation in the thin Martian atmosphere (e.g., Kahre et al., 2017; Martinez et al., 2017). The dust thermal forcing and the dynamics of the atmosphere are coupled through the fact that atmospheric motions both change the distribution of dust in the atmosphere and the rate of dust injection from the surface, and that the distribution and amount of dust modifies atmospheric motions through its influence on radiative heating (e.g., Guzewich et al., 2013; Newman et al., 2002; Wu et al., 2020).

Some of the atmospheric transport of dust and all of the lifting of dust from the surface occurs within the planetary boundary layer (PBL). The PBL is the atmospheric layer, typically within 10 km of the surface, where thermally and mechanically forced turbulence (free, natural, or buoyancy-driven and forced or shear-driven convection, respectively) dominates atmospheric dynamics (Goody & Belton, 1967; Petrosyan et al., 2011; Spiga, 2019). See Appendix A for a more detailed discussion of the PBL terminology used in this study. Due to the large diurnal variation of ground temperatures and the strong coupling between the surface and the lower atmosphere, there is a much more exaggerated diurnal evolution of the Martian PBL relative to that of the Earth (e.g., Spiridonov & Ćurić, 2021; Stull, 1988). At night, the PBL can become very shallow and highly stable (e.g., Petrosyan et al., 2011; Spiga, 2019), but during the day deep, thermally driven, natural convection dominates. As our interest in this study is upon how dust radiative heating interacts with thermal convection, we will henceforth use the more specific term convective boundary layer (CBL) when discussing the daytime PBL.

Strong vertical motions within the CBL can occur on multiple horizontal scales, ranging from many kilometers down to meters. The largest lateral scales of several tens of kilometers correspond to quasi-cellular thermal convection for the deepest CBL depths and cell aspect ratios of 1–4 (e.g., Zhou et al., 2014). These cellular structures approximate idealized Rayleigh-Bénard convection cells (or simply Bénard cells), especially in the lower CBL, and are the eponymous "large eddies" that are fully resolved with large eddy simulation (LES). As in Richardson and Newman (2018), we define scales of atmospheric motion to be "microscale" for <5 km, "mesoscale" for 5–500 km, and "synoptic scale" for >500 km. Some of the strongest vertical motions at microscales develop into tight vortices, these strongest of updrafts correspond to the cores of small convective vortices (usually with diameters less than 1 kilometer), which, if dusty, are called dust devils (e.g., Michaels & Rafkin, 2004; Spiga & Forget, 2009; Toigo et al., 2003). However, these tight, rapidly rotating updrafts represent only a tiny fraction (by area) of the total updrafts within CBL convective cells. Some fraction of the convective vortex size spectrum may be captured by LES—but generally not all, depending on the specific LES resolution chosen (Nishizawa et al., 2016).

While the Martian CBL has been examined in some detailed with LES and, to a more limited degree, with observations (e.g., Petrosyan et al., 2011; Spiga, 2019), the LES studies thus far have used laterally uniform dust heating. However, dust in the lower Martian atmosphere often exhibits lateral structure, from distinct dust devils to implied convective granularity in dust clouds (e.g., Fisher et al., 2005; Guzewich et al., 2015; Inada et al., 2007; Määttänen et al., 2009). These observations and the known radiative properties of dust motivate the question of whether the spatial distribution of dust can feed back onto the dynamics of dust transport through the radiative effects of dust modifying the CBL and hence also the injection of dust from the surface into the atmosphere (e.g., Daerden et al., 2015; Fuerstenau, 2006; Heavens et al., 2011; Rafkin, 2009; Spiga et al., 2013). Of specific importance are the questions of whether the radiative heating due to the lateral concentration of dust modifies: (a) the altitudes to which dust can be transported; (b) the vigor and depth of the CBL circulation; and, (c) the distribution of surface wind stresses that drive dust lifting from the surface. Current parameterizations of PBL physics used in global and mesoscale models do not include the effects of lateral dust variations—and consequent radiative feedback—within CBL circulation structures and thus may incorrectly represent the response of the CBL, and dust vertical mixing and lifting, to a given vertical atmospheric temperature and wind profile, or to atmospheric dust loading. The purpose of this study is to investigate the degree and nature of the feedback between dust lateral inhomogeneity and CBL motions.

In this study, we use the Mars Weather Research and Forecasting (MarsWRF) model (Lee et al., 2018; Richardson et al., 2007; Toigo et al., 2012) in its LES configuration in order to directly resolve much of the spectrum of motions in the CBL. LES is designed to capture the largest scales of motion within the CBL (i.e., largest-scale motions within the microscale range) but is not designed to represent motions on larger scales such as mesoscale or synoptic/global scales, which are either ignored or imposed as uniform boundary conditions. Since real atmospheric motions occur over a continuum of length scales, it is not possible to perfectly categorize motions into distinct scales. However, the two dividing lines between the micro-, meso-, and synoptic scales represent real "clustering" of motions on scales determined on the lower end by the maximum size of CBL convection (in this study, we take this to be roughly 10 km) and at the larger end, by the minimum scale of baroclinic eddies (which is unimportant for this study, but which we take to be roughly 500 km). LES is also not designed to represent motions on the smallest scales of motion (i.e., Kolmogorov scales, typically <1 cm) that are important for thermal and mechanical dissipation. This distinguishes LES from direct numerical simulation and means that LES still requires parameterization of unresolved, subgrid scale eddy diffusion. In practice, the grid spacing of LES on Mars is typically set at 1–100 m, and this is done in order to make LES of meaningful CBL dynamics computationally tractable.

In this study, the MarsWRF model run in LES mode is described in Section 2, where we discuss the model configuration, physics parameterizations including the treatment of aerosols, and the two specific dust distribution scenarios used in this study. In Section 3, we describe LES cases with a fixed dust scenario matching the times and locations of radio science observations described by Hinson et al. (2008) (specifically their cases *a*, *b*, *c*, and *i*). These observations have also been simulated with the LMD-LES model (Spiga et al., 2010) and we use the comparison to validate the performance of MarsWRF-LES. In Section 4, we set up several experiments to explore the effects of our two dust distribution scenarios—the fixed dust scenario and the variable scenario—on the CBL evolution. In Section 5, we examine the effect of dust concentration in the CBL on the distributions of radiative heating and on the vertical and horizontal winds. We specifically quantify the response of the CBL in terms of a Dust Inhomogeneity Index (DII). Finally, in Section 6, we summarize the major findings of this work and provide some discussion.

2. Model Description

We simulate the Martian CBL using the MarsWRF model (Richardson et al., 2007), a Mars-adapted version of National Center for Atmospheric Research (NCAR) WRF model that has been used for terrestrial LES extensively over the last decade (Powers et al., 2017). Richardson et al. (2007) showed a limited set of LES using MarsWRF, but the model setup and the model performance were not described in detail. WRF also functions as the dynamical core for the Laboratoire de Météorologie Dynamique (LMD) Mars LES but using independently developed physics (Colaïtis et al., 2013; Spiga et al., 2010).

The MarsWRF model used in this study is based on the WRF release version 3.3.1 (see the NCAR WRF website http://wrf-model.org for more information on model versioning). The model is essentially identical to that used most recently for simulating winds and surface pressure at the Curiosity landing site (Newman et al., 2017; Richardson & Newman, 2018), and the synoptic-scale "solstitial pause" of high-latitude transient eddy activities (Lee et al., 2018). The MarsWRF model is capable of simulating atmospheric dynamics with a wide range of length scales across the micro-, meso- and synoptic scales. The structured "Arakawa C-grid" WRF mesh can be configured to cover the whole planet as a traditional General Circulation Model (GCM), with or without nested mesoscale domains, or as limited area mesoscale or microscale (LES) domain. In this study, the LES mesh is treated as an idealized domain with doubly periodic boundary conditions. This can be thought of as creating an effectively boundaryless infinite plane, although motions on scales larger than half the mesh extent are suppressed by the periodicity.

The model includes a two-stream radiative transfer code that simultaneously provides atmospheric and surface heating rates due to gases and aerosols in both visible and thermal infrared wavelengths (Mischna et al., 2012). The surface temperature and the sensible heat flux may be either prescribed or evolved prognostically by the model. The prognostic scheme treats the surface energy balance and the diffusion of heat within a multi-layer subsurface model (Richardson et al., 2007). Topography, surface albedo, thermal emissivity, and subsurface thermal diffusivity may be set as constants or using maps generated from orbiter data

sets. While in this study, we use laterally uniform surface and subsurface properties, the LES-configured model is also able to ingest high resolution digital terrain elevation products.

While LES is designed to capture the largest scales of CBL motions, it does not resolve all motions down to the scales of dissipation, which are far smaller than ~1 m. Instead, a Sub-Grid Scale (SGS) (often also referred to as Sub-Filter Scale [SFS]) parameterization is used, which in the simulations described in this study is implemented as a diffusion of heat, momentum, and tracers. The scheme calculates the diffusivity and viscosity based on a prognostic value of turbulence kinetic energy (TKE) evolved using resolved variables. The SGS TKE scheme is discussed in more detail in Appendix B, as is its relationship to the other widely used SGS in WRF, the three-dimensional Smagorinsky scheme.

2.1. Fixed and Variable Atmospheric Dust

The atmospheric radiative transfer code requires information on the spatial distribution, composition, and size distribution of aerosols in the atmosphere. This information can be either prescribed or evolved prognostically in the model. In this work, we use a prescribed "fixed dust scenario" to provide control cases, and a prognostic simulation in order to examine the importance of spatial variation of dust, the "variable dust scenario." In both cases, the optical properties of dust remain fixed in the simulations. They are calculated using Mie scattering and assuming a fixed dust size distribution employing a modified gamma size distribution with effective radius, $r_{\text{eff}} = 1.7$ μm, and effective variance, $\nu_{\text{eff}} = 0.4$ (these are reasonable values based on observations of the Martian lower atmosphere e.g., Tomasko et al., 1999), and using indices of refraction from Wolff and Clancy (2003). In this study, optical depth is always taken to be the visible optical depth, and specifically the value at 0.67 μm.

In the "fixed dust" (FD) cases, dust is prescribed to vary in the vertical according to a modified Conrath distribution (Conrath, 1975; Montmessin et al., 2004) which corresponds to constant dust mass mixing ratio up to a capping altitude, and with the dust uniformly distributed in the horizontal and not varying with time. In this study the LES model top is generally placed at 12–15 km, which is below typical capping altitudes, thus the Conrath profile yields an almost uniform vertical dust mass mixing ratio profile. While the dynamical model top is placed at 12–15 km, the radiative transfer scheme treats absorption, scattering, and (for the infrared) emission through the full column depth. However, dust opacity is only present within the depth covered by the dynamical model, and thus the optical depths reported here correspond to the total optical depths between the surface and the dynamical model top at 12–15 km.

The "variable dust" (VD) cases allows the dust distribution to evolve spatio-temporally by parameterizing dust lifting, transport, and sedimentation. For this scenario, a single dust tracer bin is used to perform sedimentation, transport by resolved winds, and diffusion by subgrid scale turbulence (the single dust bin scheme is the same as that used and described by Newman & Richardson, 2015). A representative size of 2 μm radius is chosen for the dust particles for the purposes of sedimentation and radiative properties. The simulations are initialized with a modified Conrath profile of dust, which except where stated corresponds to a visible column optical depth of 0.3. In these simulations, microphysical interactions with water are not used; the LES cases described here are dry, that is, there is no water ice or water vapor in the model.

At the surface, resolved winds are used to lift dust via the wind stress lifting parameterization described in Newman and Richardson (2015), in which dust is injected into the lowest model layer whenever the wind stress exceeds a constant threshold. The rate of dust injection, Q_s, is determined following the scheme of Lettau and Lettau (1978) and as shown in Newman and Richardson (2015) as:

$$Q_s = \max\left[0, \left(\alpha_N \frac{\rho}{g} u_{drag}^3 \left(1 - \frac{u_{drag}^t}{u_{drag}}\right)\left(1 + \frac{u_{drag}^t}{u_{drag}}\right)^2\right)\right] \quad (1)$$

where ρ is the near-surface air density, g is the acceleration due to gravity, u_{drag} is the frictional velocity, and u_{drag}^t is the threshold frictional velocity; and where $u_{\text{drag}} = (\tau/\rho)^{1/2}$, with τ being the atmospheric shear stress at the surface. For our experiments, we choose the value of τ^t, the threshold wind stress, and then determine the u_{drag}^t value used in Equation 1 based on the value of ρ at that time and location. The lifting rate parameter, α_N, is a free parameter that we choose and then hold constant for a given simulation. We select values of

Table 1
Four LES Simulations (Cases a, b, c and i in Hinson et al., 2008) Carried Out for Comparison With Spiga et al. (2010)

	L_s (°)	Lat (°N)	Long (°E)	Thc (tiu)	Albedo	Znt (m)	$T_{s,max}$ (K)	θ_{mix} (K)	P_s (Pa)
a	47.1	21.8	205.0	55	0.27	0.01	278	221	868
b	51.2	13.7	204.6	50	0.30	0.01	275	220	854
c	52.1	12.3	237.2	60	0.30	0.01	275	250	482
i[a]	47.8	20.6	74.0	300	0.13	0.01	270	233	630

Note. L_s is the areocentric longitude, Lat is the north latitude, Long is the east longitude, Thc is the thermal inertia (1 tiu = 1 J m^{-2} K^{-1} s$^{-1/2}$), Znt is the surface roughness, $T_{s,max}$ is the maximum surface temperature in the daytime (between roughly 12 to 13 p.m.), θ_{mix} is the potential temperature in the mixed layer at 5 p.m. and P_s is the surface pressure.

LES, large eddy simulation.

[a]Indicates that this case location and time is used as the baseline reference for our "Fixed Dust" and "Variable Dust" experiments in this study.

α_N so as to generate different total optical depths. It is not clear, how well α_N would compare between different models due to its sensitivity to the unresolved surface layer processes. For simplicity, we do not include any parameterization for lifting of dust associated with the rapid change of surface pressure within convective vortices (the "delta-p" or "suction" effect; e.g., Neakrase et al., 2006, 2016), the contributions of which remain unclear. As with the FD cases, there is no dust optical depth above the dynamical model top in the VD cases.

3. Model Consistency and Observational Validation

High vertical resolution measurements covering the entire vertical extent of the CBL are rare on Mars, which limits efforts to directly validate LES. *In situ* near surface and tower observations, which are crucial for LES validation on Earth, are very limited or nonexistent, respectively, on Mars. Of the remotely sounded observations from orbit, radio occultation measurements of thermal structure provide one of the best constraints due to their relatively high vertical resolution (roughly 100 m), albeit with extremely long lateral sampling lengths through the limb (roughly 400 km) (e.g., Hinson et al., 2008). Hinson et al. (2008) use Mars Express radio occultation measurements, isolating profiles that provided good coverage of the well-developed CBL in tropical latitudes and located sufficiently far from large topographic relief that the profiles could be taken as representative of a relatively uniform CBL over the long lateral observational path. Based on these observations, Hinson et al. (2008) investigated the depth of the CBL in the low-latitude regions. Specifically, the observations highlighted a dependence of the CBL depth on the background thermal structure, the surface temperature, and the surface air density that is, extremely useful for our purposes as the dependence can be used to quantitatively validate (or invalidate) the performance of the LES. Indeed, Spiga et al. (2010) conducted an extensive analysis of these radio occultation profiles with the LMD-LES model—which also uses the WRF dynamical core but is forced with a completely different set of physics—and thus the combination of the Hinson et al. (2008) observations and the Spiga et al. (2010) profile simulations and derived model quantities provides a very convient means of testing both the degree to which MarsWRF LES can reproduce observations and the degree to which MarsWRF LES is consistent with other published LES performance.

In this section, we describe simulations undertaken with fixed dust scenarios and with the physical parameterizations as described in Section 2, including the prognostic treatment of ground temperature and surface layer mixing. We specifically describe simulations designed to replicate the times and locations labeled cases a, b, c, and i by Hinson et al. (2008) and as also used by Spiga et al. (2010). For ease of comparison with those prior works, the location and forcing information for the four cases are given in Table 1 along with a limited sample of prognostic summary information from our LES.

The default LES numerical mesh uses 145 × 145 × 100 grid points (the two horizonal directions and finally the vertical direction) with 100 m horizontal resolution and a 15 km model top, similar to that used by Spiga et al. (2010). The mesh lateral and vertical extents were chosen to accommodate the largest expected convective cell sizes based on the radio science estimates of the CBL depth (Hinson et al., 2008) and expected aspect ratios of 1–4 for Rayleigh-Bénard-like convection. In the vertical, we adopted an increasingly stretched grid with each layer 3.5% thicker than the one below it so that the grid depth near the surface is on the order of 10 m, to ensure high enough vertical resolution for the simulation of the shallow surface layer. The time step *dt* is 1 s. Table 1 shows the solar longitude (*Ls*), latitude, longitude, thermal inertia, albedo, and surface roughness of the four cases, and these were chosen to be the same as those used by Spiga et al. (2010). The LES was set up with doubly periodic lateral boundary conditions, no externally imposed wind was applied (i.e., the background wind was zero), and the dust was set up such that the visible dust optical depth was 0.3. The model was initialized using the Mars Express radio occultation pressure-temperature profiles as retrieved by Hinson et al. (2008). Each run was initialized at 17 Local Time (LT), where this is local true solar time. In order to seed the model with some initial turbulence, slight random perturbations were added to the temperature (with a maximum amplitude of 0.2% of the full temperature). Each simulation was then

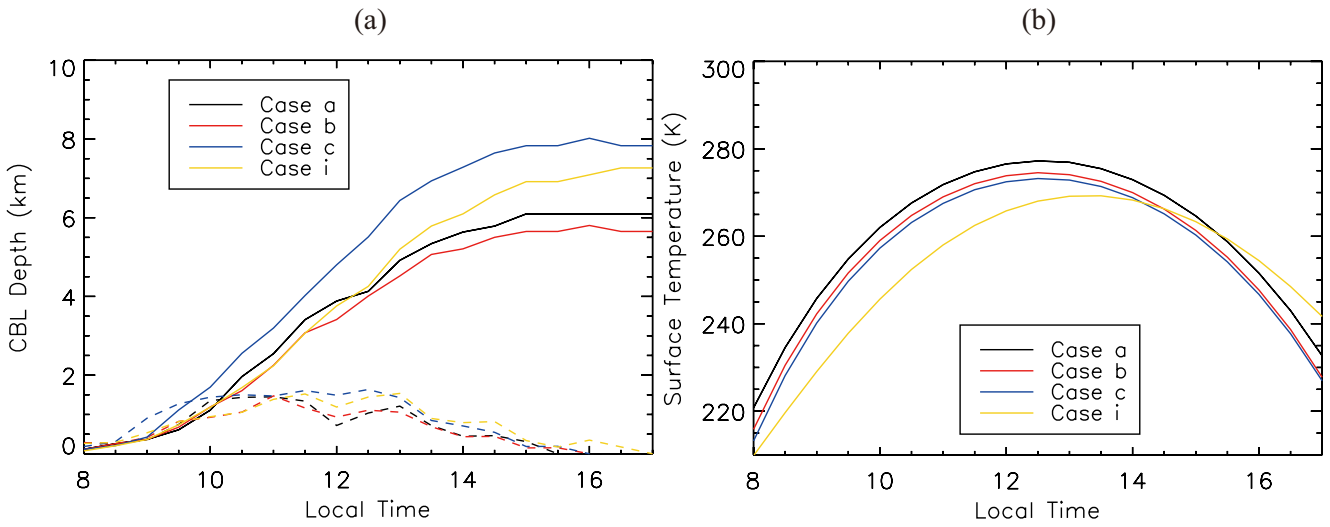

Figure 1. Evolutions of (a) Convective boundary layer (CBL) depth (km) and (b) Surface temperature (K) with time in the Martian daytime for the four Hinson cases. Dashed lines in (a) are the corresponding time derivatives of the CBL depths (km/h) with time.

allowed to run through the Martian night to allow the LES to "spin up" (i.e., to allow the model to establish a diurnally varying quasi-equilibrium less dependent upon imposed initial conditions) and we examined output from the following simulated Sol.

To determine the CBL depth from the model thermal profile, we follow the method used in Hinson et al. (2008) and Spiga et al. (2010). The static stability, S, is defined as:

$$S(z) = \frac{\partial T}{\partial z} + \frac{g}{c_p} \tag{2}$$

where T is the air temperature, z is the vertical height, g is the acceleration due to gravity and c_p is the specific heat capacity of air at constant pressure. Using Equation 2, S is the calculated from the mean atmospheric temperature profiles. The CBL depth, z_i, is the defined as the altitude above the surface where S first reaches 1.5 K/km. The evolution of the CBL depth with local time during the four cases is shown in Figure 1a. All four cases exhibit typical CBL daytime growth. The CBL depth grows very slowly before 9 LT as the overlaying nocturnal stable layer is progressively eroded and overcome. After that, the CBL begins to entrain the residual layer and grows rapidly until about 15 LT, after which time it maintains a reasonably constant maximum depth until the observation (or "forecast") time at 17 LT.

Table 2
CBL Depths in Kilometers Predicted By MarsWRF, Estimated From Radio Science Occultation Retrievals By Hinson et al. (2008), and Predicted By the LMD-LES By Spiga et al. (2010) for the Profile Cases a, b, c and i as Defined By Hinson et al. (2008)

Case	MarsWRF	Observations	LMD-LES
a	6.1 (19.6%)	5.1	5.9 (15.7%)
b	5.7 (35.7%)	4.2	5.3 (26.2%)
c	7.9 (−3.66%)	8.2	7.8 (−4.88%)
i	7.3 (−27%)	10	7.4 (−26%)

Note. The error of the MarsWRF and LMD-LES estimates compared to the observations is shown as a percentage of the observationally inferred CBL depth in parenthesis for both models, that is, error = (model-observation)/observation.

CBL, Convective boundary layer; LES, large eddy simulation; LMD, Laboratoire de Météorologie Dynamique; MarsWRF, Mars Weather Research and Forecasting.

The CBL top heights (or "CBL depths"; the two terms are equivalent in this context) of cases a, b, c, and i predicted by MarsWRF at 17 LT are about 6.1, 5.7, 7.9 and 7.3 km, respectively (Table 2). These compare with Hinson et al. (2008) observational estimates of 5.1, 4.2, 8.2, and 10 km, respectively, for the real atmospheric profiles. We can see dramatic variations of CBL depth in different locations which was even more dramatically indicated in Hinson et al. (2008). This site-to-site variability is caused by the very different elevations of the two groups of sites, with a and b at much lower elevation than c and i (Hinson et al., 2008). The elevation has two primary effects: (a) A site at higher elevation means a lower surface pressure (the surface pressure in our case c is only about 55% of that in our case a), and hence a similar amount of (sensible and thermal infrared) heat flux from the surface into a much thinner atmosphere would lead to a much larger heating rate, and hence a deeper CBL than a low elevation site; (b) The atmosphere a few kilometers above the surface into which the CBL is expanding will generally be cooler at the

higher geopotential over a high elevation surface than it will at the same relative altitude over a low elevation surface (see Figure 5a from Hinson et al., 2008). As a result of these effects, the convective available potential energy of CBL thermals is larger over higher elevation surfaces which means convection can reach a higher altitude and produce a deeper CBL at these sites.

Despite similar trends, LES predicts a more limited range of CBL depths than is inferred from the observations (Table 2). The observations suggest an almost 6 km difference in depth between the minimum and maximum cases (b and i, respectively), with the i case observationally inferred to be almost 2.4 times deeper than the b case, while MarsWRF suggests it is only 1.8 km or 30% deeper. However, this under-prediction of the influence of surface elevation on the CBL depth is also present in the LMD-LES results presented by Spiga et al. (2010) and included for reference in Table 2. Spiga et al. (2010) find the case a, b, c, and i CBL to be 5.9, 5.3, 7.8 and 7.4 km, respectively. MarsWRF thus is in much better agreement with the LMD-LES (showing only a 100–400 m discrepancy between the models) than either LES is with the observational inference (discrepancies of 300 m–2.7 km); though it should be noted that both models show the same sign of the behavior as the observations (i.e., lower elevation surfaces have shallower CBL depths).

The similar model behavior regarding CBL depth is also reflected directly in the thermal predictions: the maximum surface temperatures of the four MarsWRF cases shown in Table 1 are close to those predicted by Spiga et al. (2010) (within 4–9 K), and the mixed layer potential temperatures at 17 LT are similar to those in Spiga et al. (2010) except for case c. Note that potential temperature in this study is calculated using $P_0 = 610$ Pa. Modest discrepancies between the models may result from several factors. First, while a dust optical depth, $\tau = 0.3$, was used both here and by Spiga et al. (2010), the radiative transfer schemes, the dust optical properties, and the specific details of the vertical distribution of dust were slightly different between the LMD-LES and MarsWRF-LES. The daytime maximum ground temperature is especially sensitive to the amount of sunlight reflected by the atmospheric dust. Second, we have used the Mars Express radio occultation profiles for the initial model thermal structure while Spiga et al. (2010) used output from a GCM, and our simulations are started in the late afternoon, and thus have a longer spin-up period that covers the whole night. While the evening collapse of the CBL and the subsequent reestablishment after dawn mean that the MarsWRF case is likely less dependent upon the initialization, this may or may not be an advantage depending on a number of factors, including the degree to which the model mean state drifts away from the observed state.

Despite very minor differences, our results reveal essentially the same qualitative and quantitative behavior when the two models simulate the four cases. The CBL depth trends shown in Figure 1a for the MarsWRF-LES compare well with those from the LMD-LES shown in Figure 2 from Spiga et al. (2010). Picking one case as an illustrative example, the increase of the CBL depth in case i is slower than the other cases in the morning, but faster at noon and in the early afternoon. This is consistent with the evolution of surface temperatures shown in Figure 1b, which supports the Spiga et al. (2010) suggestion that the slower growth of the CBL for case i before 14 LT is due to the larger surface thermal inertia at this site. We also compared the MarsWRF- and LMD-LES turbulent kinetic energy, vertical eddy heat flux, and the updraft maximum vertical velocities for cases where plots were available in Spiga et al. (2010), with the models agreeing well (detailed comparisons are not shown here for the sake of brevity). From a purely modeling perspective, we conclude that the MarsWRF- and LMD-LES produce very similar simulations of the CBL under similar conditions. This similarity in performance likely results from (a) the use of a nearly identical dynamical core in both models, and (b) the use of physics suites that, while different in concept and implementation, were both developed and tuned to simulate available observations of Mars.

The quantitative differences between the CBL depths produced by either LES model and the observations suggests a consistent error in one or more of: (a) the estimated surface properties (albedo, thermal inertia, etc.), (b) the specification of aerosol atmospheric radiative heating (or other radiative heating rate errors), (c) the representation of the surface layer fluxes into the lowest model layer, (d) the fidelity of the WRF dynamical core and/or SGS parameterization in simulating large PBL eddies in the Martian atmosphere or (e) the influence of mesoscale circulations beyond the scale of the LES domain (Hinson et al., 2019). The second and third sources of error would require correlated errors between the separate MarsWRF and LMD physics, which may seem less likely, but might result from the "herd effect" that might influence physics package development as groups tend not to want to be the "outlier" group in intercomparison efforts. The

Table 3
Sensitivity of the Modeled Martian Boundary Layer Depth z_i (Average Value Between 17 and 17.5 LT) to the LES Resolution, Domain Size, and Model Top

Mesh Name	Grid $N_x \times N_y \times N_z$	dx (m)	dz_1 (m)	dz_t (m)	x (km)	z (km)	z_i (km)
1	290 × 290 × 100	50	8	242	14.5	12	7.29
2	145 × 145 × 100	100	8	242	14.5	12	7.23
3[a]	145 × 145 × 100	100	10	247	14.5	15	7.27
4	50 × 50 × 75	100	25	260	5	15	6.91
5	125 × 125 × 75	100	25	268	12.5	15	7.18
6	50 × 50 × 50	100	66	327	5	15	6.72
7	200 × 200 × 100	100	10	247	20	15	7.31
8	100 × 100 × 100	200	10	247	20	15	7.31
9	100 × 100 × 100	200	120	120	20	12	6.70
10	100 × 100 × 600	200	20	20	20	12	7.21

Note. *Nx*, *Ny*, and *Nz* are the number of grid points in the mesh in the two horizontal (*x* and *y*) and vertical (*z*) directions. *dx* is the horizontal grid spacing (which always equals *dy* in all LES presented in this study). dz_1 is the model layer thickness at the base of the column (i.e., the layer closest to the surface). *zi*, is the predicted height of the top of the CBL at the forecast time (17–17.5 LT). dz_t is model layer thickness at *zi*. *x* is the total domain extent in both the x and *y* (horizontal) directions. *z* is the total domain extent in the vertical.

CBL, Convective boundary layer; LES, large eddy simulation.

[a]Indicates that mesh 3 is the selected default mesh used in most experiments described in this study.

fourth source of error seems the least likely of the four due to the extensive testing of the dynamical core by the terrestrial community (but we cannot rule out a consistent misapplication of the core to Mars in terms of choice of grid setup, etc.) Notwithstanding these concerns, we agree with the Spiga et al. (2010) conclusion that, given the uncertainty in the observations of both the atmospheric state and forcing, LES does an acceptably good job at quantitatively representing the CBL, and a much better job qualitatively, and that we can thus reasonably use the MarsWRF LES as a calibrated tool with which to gain quantitative insight into the behavior of the CBL.

3.1. Sensitivity of LES to Mesh Extent and Spacing

To evaluate the effect of different model grid setups on the LES, we used the Hinson/Spiga case i to carry out a sensitivity study for MarsWRF using the seven numerical mesh definitions shown in Table 3. Using the predicted thickness of the CBL, z_i, at 17 LT as the primary diagnostic (see the last column of the table), Table 3 allows us to draw several conclusions regarding the sensitivities of the model to the mesh setup. First, the results are insensitive to the horizontal resolution within a range between 10 and 100 m (see meshes 1 and 2) and to the model top height as long as the model top is sufficiently higher than the CBL depth (see meshes 2 and 3). Second, while meshes 2 and 4 share similar horizontal resolution, the CBL depth of mesh 4 is ∼300 m lower than mesh 2, which results from the horizontal domain extent being smaller than the maximum CBL depth. Because the width-to-depth aspect ratio of the largest CBL eddies (which are hence the CBL maximum scale setting eddies) is expected to have values between about 1 and 4, this tells us the horizontal domain extent should ideally be more than four times larger than (or at the very minimum, comparable to Willis & Deardorff, 1979) the maximum CBL depth in order to ensure that the CBL is not being numerically compressed (see meshes for which $x \geq z_i$). Note that while this might paradoxically seem to suggest that the maximum CBL depth needs to be known before the domain extent can be chosen, the minimum domain extent can in fact be found by increasing the domain extent until the maximum CBL depth no longer increases. Third, too coarse vertical resolution will lower the CBL depth (compare meshes 4 and 6). The above findings are in agreement with the sensitivity study of different extent and resolution of the LES grid by Spiga et al. (2010). As a result, we use numerical mesh 3 as the default configuration for the rest of this work in order to obtain accurate results with the lowest computational cost. For our implementation of the Hinson/Spiga case i using numerical mesh 3, the dynamical model top pressure, $p_{top} = 142.889$ Pa.

It should be noted that the vertical structure used in this study differs from Spiga et al. (2010), who use a constant value of the vertical layer spacing, Δz, in each run and with test cases where the grid horizontal to vertical aspect ratio, $\Delta x/\Delta z$, was varied from 0.71 to 1.33 between the runs. Our choice of variable (increasing with height) vertical layer spacing is designed to accomplish two things: (a) to provide better resolution of the superadiabatic layer at the bottom of the CBL, in part to allow more accurate radiative calculations (and hence better resolution of the radiative forcing of the CBL), and (b) to not waste computational cycles in the upper CBL and free atmosphere where the eddy scales will be larger (e.g., Stull, 1988). The result is smaller aspect ratios in the upper CBL in all cases. Across the full range of cases shown in Table 3, the grid cell aspect ratios thus vary from about 0.2 to 12.5 over the full domains. This is not consequential to the LES for a few conceptual reasons. First, the high vertical resolution near the surface is effectively "dynamically wasted" computation since the scale of resolvable eddies, with typical dynamical aspect ratios between 1 and 4, is controlled by the horizontal resolution: the extra vertical resolution does not gain the simulation any extra resolved eddy motion as the horizontal mesh will not allow any of these smaller scale motions to evolve (note that in this study we are limiting ourselves to consideration of daytime thermally driven convection in an unstable boundary layer, and thus consideration of small near-surface eddies is much less

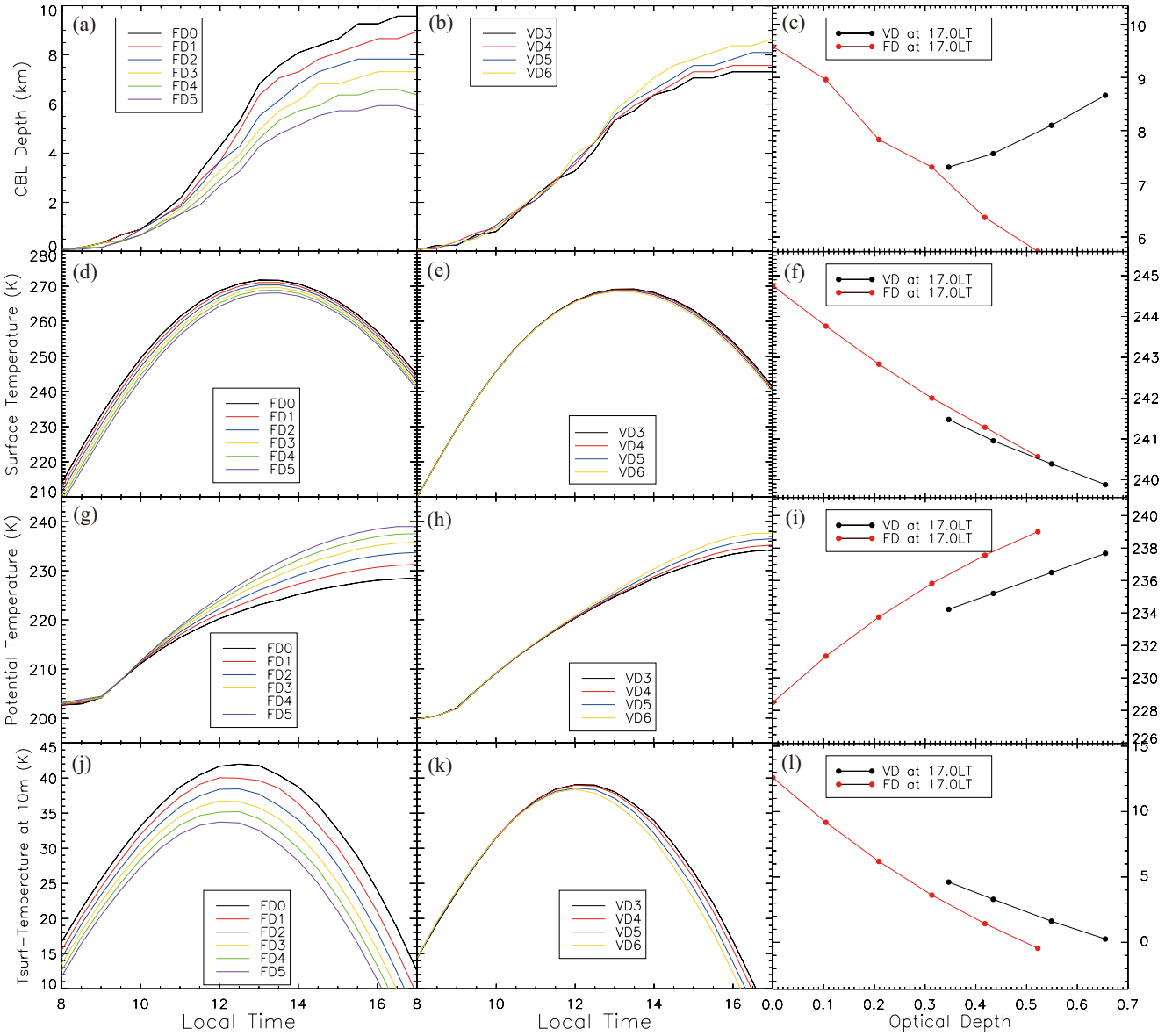

Figure 2. The evolution of (top row) the convective boundary layer depth, (second row) the surface temperature, (third row) the mixed layer average potential temperature, and (bottom row) the difference between the surface temperature and the (kinetic) air temperature at 10 m. All plots in the left-hand column show output as a function of local time for the Fixed Dust (FD) cases (see key for the meaning of line color), in the central column are for the Variable Dust (VD) cases as a function of local time, and in the right-hand column show both the FD and VD cases at 17 LT as a function of the instantaneous optical depth. Note that the *y*-axis ranges for the left and middle columns are the same but different from those of the right column. In all cases, lateral domain averages are shown. See text for meaning of the FD and VD labels. The time varying domain mean optical depths for the VD cases is shown in Figure 4.

important that it would be for a nighttime PBL simulation). Second, the smallest eddies in the CBL will generally develop near the surface as it is here that convective motions are forced and CBL motions tend to have roughly 1–4 aspect ratios (e.g., Stull, 1988). Thus, the smallest horizontal scale eddies cannot reach very far upwards into the CBL. Ideally, our grid cell spacing in the horizontal would also increase with height, but it is not possible to change Δx as a function of height. We instead increase only Δz and accept that Δx is constrained by the need to resolve lower atmosphere activity. Our limiting resolution changes from the horizontal to the vertical as we ascend the CBL, and our simulations can better resolve processes in the lower CBL than the free atmosphere, because this is where smaller scale dynamical structures of interest to us exist.

Despite the effort to craft better vertical resolution of the lower CBL and better computational performance in the upper CBL and free atmosphere, comparison of the MarsWRF LES and the LMD-LES (using

essentially the same WRF dynamical core) cases suggests that it makes little-to-no difference in terms of the simulated behavior of the CBL. For similar horizontal resolutions and model forcing and initial conditions, our comparisons show that results from the MarsWRF-LES using our stretched vertical grid are very similar to those using the fixed LMD-LES vertical grid. Additionally, we modified the horizontal-vertical aspect ratio in MarsWRF to keep $\Delta x > 0.8\Delta z$ throughout the CBL, and also ran one case with a uniform Δz and $\Delta x = 10\Delta z$ throughout the domain (meshes 8 and 10 in Table 3, respectively). These cases also showed essentially identical performance with our traditional vertical grid (mesh 7). However, our chosen vertical grid enables us to run with fewer total vertical layers and hence is computationally more efficient. As found by Spiga et al. (2010), if the vertical resolution of the lower CBL is inadequate (which appears to be true for $\Delta z \geq 100$ m for tropical daytime convection), then the CBL mixing appears to be underrepresented and the CBL depth is underpredicted (mesh 9). Combining our results with those of Spiga et al. (2010), the choice of (a) lateral and vertical domain extent (so as not to limit the maximum large eddy scale), (b) sufficient lower CBL vertical resolution (to capture the near surface thermal gradient), and (c) sufficient lower CBL horizontal resolution (to capture a sufficient fraction of the eddy spectrum, $\Delta x < 200$ m), thus appears to be much more important than the precise aspect ratio choice, or constancy of this choice across the domain, for at least the regime of roughly $0.1 < \Delta x/\Delta z < 10$.

4. CBL Development as a Function of Optical Depth in Fixed and Variable Dust LES

The primary question motivating this study is whether lateral heterogeneity of dust within the CBL during active dust lifting causes any changes in the strength and/or depth of the CBL from that which would occur if the dust were uniform. Such differences in behavior might provide a better guide into how deep into the atmosphere dust is lofted from the surface, and into potential radiative-dynamical feedback processes involving dust lifting and the CBL. In order to address this question, in this section we devise two sets of LES experiments, one in which dust is uniformly distributed, and one in which the dust is injected at the surface and the dust distributions are allowed to freely evolve based on model resolved winds and SGS diffusion (see Section 2). In the fixed dust cases, the total dust optical depth is the only free parameter, with all remaining parameters being set following the Hinson/Spiga case i settings described in Section 3 (Tables 1 and 2) and using numerical mesh 3 (Table 3). In the variable dust cases, only the injection rate constant used in the stress lifting scheme is used as a free parameter (see Section 4.2), again with all other parameters being held fixed at values from Hinson/Spiga case i and numerical mesh 3. The injection rate parameter is also held constant with time in each variable dust simulation. For comparison between fixed and variable dust cases, we select the variable dust LES case from an ensemble that has the desired total column optical depth at a given local time in order to compare with a given fixed dust case.

Since the goal of this study is to provide a first examination of aerosol-radiative-dynamical feedbacks in the Martian CBL, we are interested in a representative location and season on Mars; it is beyond the scope of this study to explore seasonal and spatial variations in the detail of the behavior. As such, we have somewhat arbitrarily chosen the Hinson/Spiga case i location and season (northern tropics and northern spring, see Table 1) to be representative and have chosen to use fixed dust optical properties (including a fixed particle size distribution) and have considered plausibly valid dust optical depths for relatively clear to relatively dusty, non-dust storm atmospheres. Details related to variations in dust optical properties, locations, and seasons are deferred to future studies. As we are primarily interested in the behavior of the CBL in isolation, we do not impose any larger-scale winds or examine topography within the domain. Our goal is to examine an almost idealized flat, infinite plane exposed to roughly Mars-like forcing and with Mars-like atmospheric properties.

4.1. Fixed Dust Cases

For fixed dust LES, we vary only the prescribed and non-time varying abundance of atmospheric dust, which modifies the total column dust optical depth at all wavelengths. The six-member "fixed dust" ensemble comprises cases yielding visible optical depth values of 0 (i.e., clear or "dust free"), 0.1, 0.2, 0.3, 0.4, and 0.5. We label these cases FD0, FD1, FD2, FD3, FD4, and FD5, respectively. We decided to limit our attention to optical depths characteristic of "normal" to moderately dusty atmospheres for three main reasons. (a)

This interval already requires a relatively large number of LES cases, considering both the fixed and variable dust cases in this study, and (b) Since the purpose of this study is to determine if there are any microscale aerosol-radiative-dynamical feedbacks between, we reasoned that if they were detected at these lowest dust optical depths, they plausibly would also extent to higher dust optical depths, and (c) In the event of aerosol-radiative-dynamical feedbacks being found, a separate study at higher optical depths investigating the potentially more complex dynamics of small scale dust storm growth would likely be warranted.

The left column of Figure 2 shows the diurnal variation of CBL depth and temperatures for cases FD0-5, while the right column shows the variation of those quantities with dust optical depth at 17 LT for all six cases. Figures 2a and 2c show that the net effect of increasing the dust loading is to significantly decrease the depth of the mature CBL. At 17 LT, the clear atmosphere CBL (case FD) is just over 9.5 km deep. With each increment of 0.1 of optical depth, the 17 LT CBL depth decreases to 9.0, 7.8, 7.3, 6.3, and 5.7 km, respectively. Thus, the CBL depth decreases by about 40% when the visible optical depth is increased from 0 to 0.5 (Figure 2c).

The surface temperature decreases (Figures 2d and 2f) while the mixed layer potential temperature increases (Figures 2g and 2i) with dust optical depth. Thus, the decrease in the mature CBL depth results from the rather straightforward combined effect of: (a) increased atmospheric dust radiative heating of the atmosphere due to the increased atmospheric absorption of sunlight, and (b) cooling of the surface due to the increased shading of the ground from solar insolation by atmospheric dust scattering and absorption. These related effects act to increase the static stability of the atmosphere and decrease the sensible and thermal infrared heat flux from the ground as optical depth increases (Figure 2l), and hence decrease the buoyant production of turbulence.

The left column of Figure 3 shows the diurnal variation of updraft wind speed, TKE, and u_{drag} for cases FD0-5, while the right column shows the variation of those quantities with dust optical depth at 17 LT for all six cases. Following the method discussed in Couvreux et al. (2009), we define a model grid box to be in an updraft whenever the vertical wind speed is >1 standard deviation above the layer mean vertical wind speed. Note that the lateral domain average vertical wind speed is small at all levels in the model because there is only a very modest net upward motion due to thermal expansion as the domain average atmosphere warms during the day. Figure 3a shows that the peak vigor of CBL mixing (at about 13.5–14 LT) is decreased as a result of increased optical depth, with the average strength of updrafts decreasing by over 25% (from a little over 6.5 m/s to below 4.75 m/s) as the optical depth increases from 0 to 0.5. By 17 LT, there is a very strong decrease of updraft speed with optical depth, falling by about 80% as the optical depth increases from 0 to 0.5 (Figure 3c). This demonstrates that increased optical depth does more than simply decrease the depth of the CBL.

The energy involved in CBL turbulent motions is quantified as the turbulence kinetic energy (TKE). The resolved TKE is calculated from the resolved perturbation velocity components, u', v', and w' as:

$$\mathrm{TKE}_{\mathrm{resolved}} = 0.5 \times \left(\langle u'^2 \rangle + \langle v'^2 \rangle + \langle w'^2 \rangle \right) \tag{3}$$

The turbulent component used in this study is calculated by $\varphi' = \varphi - \langle \varphi \rangle$ at each altitude for each local time, where "$\langle\rangle$" indicates horizontal domain averaging and φ can be wind fields u, v, w, pressure, p, or potential temperature, θ. The number of lateral model grid points used in the analysis in this study is large enough to satisfy the ergodic principle that time and spatial averaging yield similar statistical results (Stull, 1988). The TKE used in our analysis is the sum of the resolved TKE (Equation 3) and the prognostic unresolved TKE from the SGS parameterization (see Appendix B; note that the SGS TKE is generally less than 20% of the total TKE). Also note that TKE is defined as an intensive property such that it is not actually an energy but an energy per unit mass of air (units of m^2/s^2 are the same as J/kg).

Figures 3d and 3f show that the mass-weighted average TKE over the CBL depth decreases with dust optical depth, similar to the updraft speeds. The maximum TKE value (between 14 and 15 LT) decreases by more than a factor of 2 as the optical depth increases from 0 to 0.5. At 17 LT the decline is nearer 90%. This is a much larger fractional decrease than for either the CBL depth or the updraft speed, suggesting that the CBL becomes much less turbulent as the optical depth increases (which is also reflected in the vertical eddy heat flux, not shown). The total turbulent kinetic energy (TTKE) in the CBL can be obtained as the

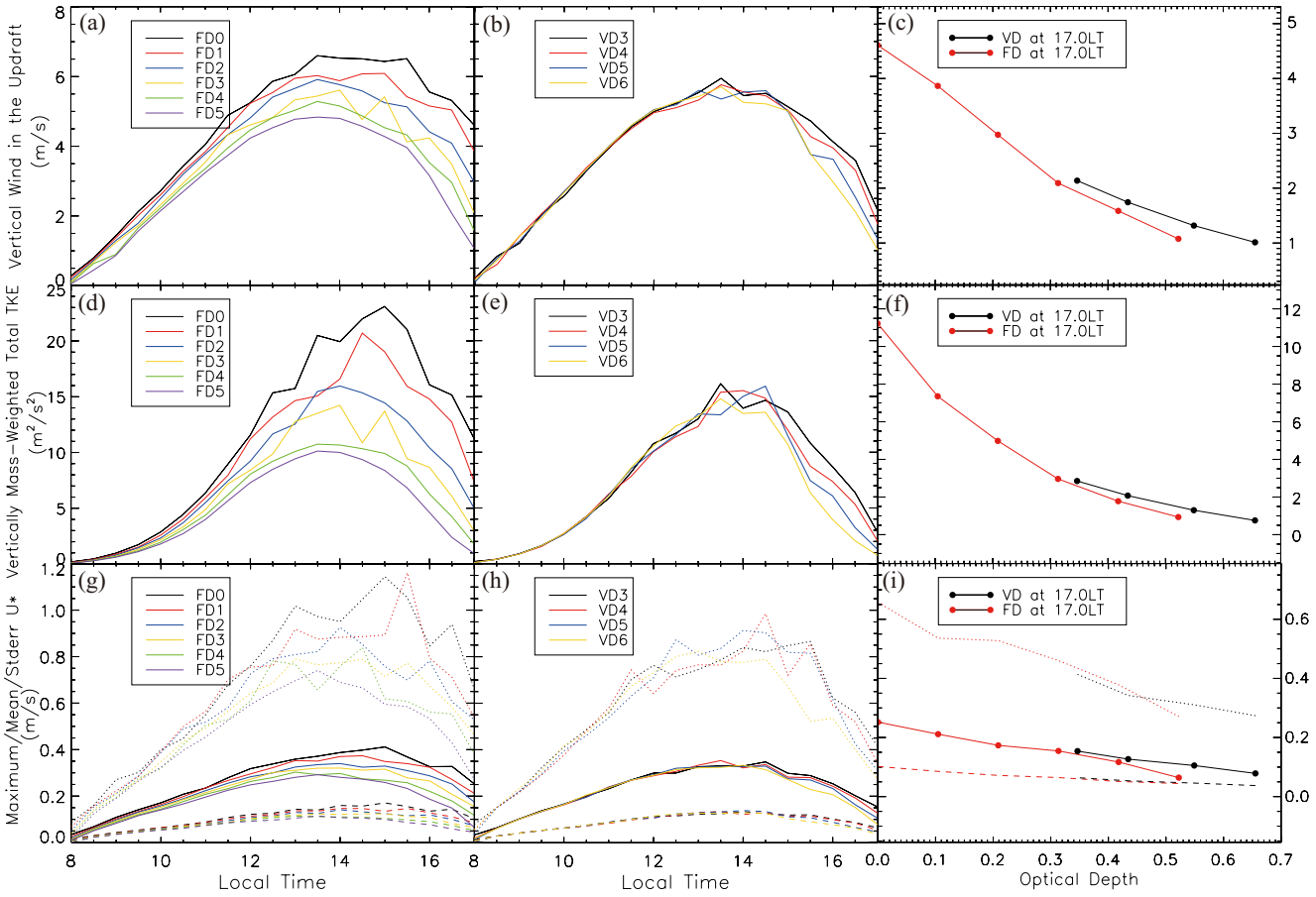

Figure 3. The evolution of (top row) updraft wind speeds, (second row) the Mixed Layer average turbulence kinetic energy, (third row) the mean (dashed line), maximum (dotted line), and standard deviation (solid line) of the surface frictional velocity (u_{drag}). The meaning of the columns and of the line colors is otherwise the same as for Figure 2. Note that the *y*-axis ranges for the left and middle columns are the same but different from those of the right column.

vertically integrated mass-weighted TKE in units of J/m^2 within the CBL. The TTKE also dramatically decreases with increasing optical depth, reflecting the much lower convective mixing due to the reduced surface-atmosphere temperature contrast. This marked negative feedback of dust on CBL convection suggests a significant negative feedback between atmospheric dust optical depth and dust lifting from the surface via convective processes at CBL length scales. Such a negative feedback effect is noted in numerical models that parameterize dust lifting on such scales (e.g., by "dust devils"; Newman et al., 2002).

Figures 3g and 3i show the evolution of the surface wind drag velocity with local time and optical depth, where the drag velocity, u_{drag}, is related to the shear stress, σ_{stress}, of the wind acting on the surface and air density ρ by:

$$\sigma_{stress} = \rho u_{drag}^2 \quad (4)$$

The plots show that the mean, standard deviation, and maximum friction velocity all decrease with the increasing optical depth. Because u_{drag} and wind stress is an important contributor to dust lifting (Section 2.1), likely dominating over other affects associated with convective turbulence (e.g., the vortex delta-p effect; see Section 2.1), the decrease again suggests a strong negative feedback between increased optical depth and dust lifting at CBL length scales.

4.2. Variable Dust Cases

In order to examine the impact of radiatively active dust heterogeneity within the CBL while dust is being lifted, we conducted four LES experiments with a single, fixed value of the wind stress lifting threshold (τ^t)

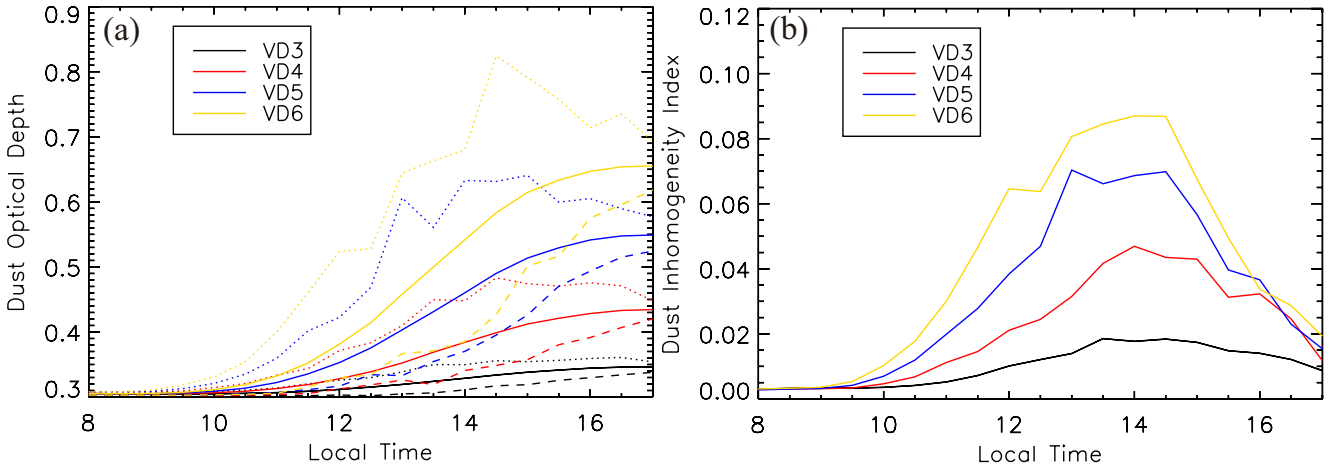

Figure 4. The variation of (a) the mean (solid lines), maximum (dotted lines), and minimum (dashed lines) dust optical depth and (b) the dust inhomogeneity index (DII, which we define as the standard deviation of dust optical depth for the domain divided by the averaged dust optical depth) in the variable dust (VD) cases as a function of local time. For reference, the domain average total visible column optical depth at 14.5 LT for cases VD3, VD4, VD5, and VD6 is roughly 0.3, 0.4, 0.5, and 0.6, respectively. The optical depth is not constant in time due to the interactive injection of dust into the atmosphere from the surface.

but with different lifting rate parameters (α_N) (see Section 2.1 and Equation 1). As with the fixed dust cases, all other settings were those from Hinson/Spiga case i, (see Section 3 and Table 1) and numerical mesh 3 (Table 3). The dust mass mixing ratio was initialized such that the total visible column depth $\tau = 0.3$. The dust was uniformly distributed in the horizontal, and in the vertical the dust was distributed using a Conrath profile (see Section 2). The lifting threshold (τ' in Equation 1, not to be confused with the optical depth, τ) was tuned to be small (0.0001 Pa) so as to allow dust lifting activity to commence with only LES-resolved winds (and no imposed background winds) as soon as the CBL began to grow at 8 LT. The dust lifting rate parameters, α_N, for the four simulations were tuned such that the peak dust optical depth in the late afternoon during the simulations fell within increments comparable to those of the fixed dust cases ($\tau = 0.3$–0.4 for the case labeled VD3, $\tau = 0.4$–0.5 for case VD4, $\tau = 0.5$–0.6 for case VD5 and $\tau = 0.6$–0.7 for case VD6). The values of α_N required were on the order of 10^{-5} in each case. Summary results for the four variable dust cases are presented in Figures 2b, 2e, 2h, 2k, 3b, 3e and 3h. The evolution of the dust optical depth is shown in Figure 4.

Figure 2b shows the evolution of CBL depths for the four variable dust cases. The CBL depths of all the cases are roughly the same before about 11.5 LT but start to differ thereafter. Figure 2b shows that the maximum CBL depth for the VD cases increases with increasing dust optical depth. It is important to note that this is the opposite sign of the trend to that shown in Figure 2a for the FD cases. Indeed, Figure 2c shows that between $\tau = 0.3$ and 0.6, the maximum CBL depth for the VD cases increases from about 7.25 km to about 8.75 km (or about a 20% increase in depth). Directly comparing the FD and VD cases for $\tau = 0.3$ and $\tau = 0.5$: while the FD cases showed a 22% *decrease* in CBL depth for an increase of 0.2 in optical depth, the VD cases showed instead an *increase* in CBL depth of about 7% (Figure 2c). Thus, the VD case CBL depths respond in a completely opposite manner to the increase in optical depth relative to the FD case CBL depths.

Figures 2e and 2h show that the VD cases have a very slightly reduced sensitivity of the surface temperature and the mixed layer potential temperature to the total dust optical depth as compared to the FD cases (also Figures 2f and 2i). For the ground temperature, the increased optical depth from $\tau = 0.3$ to 0.5 produced less than 1 K decrease for the VD case, while for the FD case ground temperature decreased by about 1.5 K (Figure 2f). For the mixed layer potential temperature, decreased sensitivity to optical depth increase is also apparent (Figure 2i). Thus, the dramatic change in the magnitude and sign of the change of the CBL depth for a given change of optical depth between FD and VD cases is not controlled by a significant change in the spatial average boundary forcing (i.e., the surface-atmosphere temperature contrast) nor the mean atmospheric static stability (Figures 2j–2l). While the surface-atmosphere temperature contrasts are larger in the VD cases (Figure 2l), they vary with optical depth with the same sense as the FD cases. In short, while all of the spatial average thermal metrics in the VD cases show a similar response to increasing optical depth as in

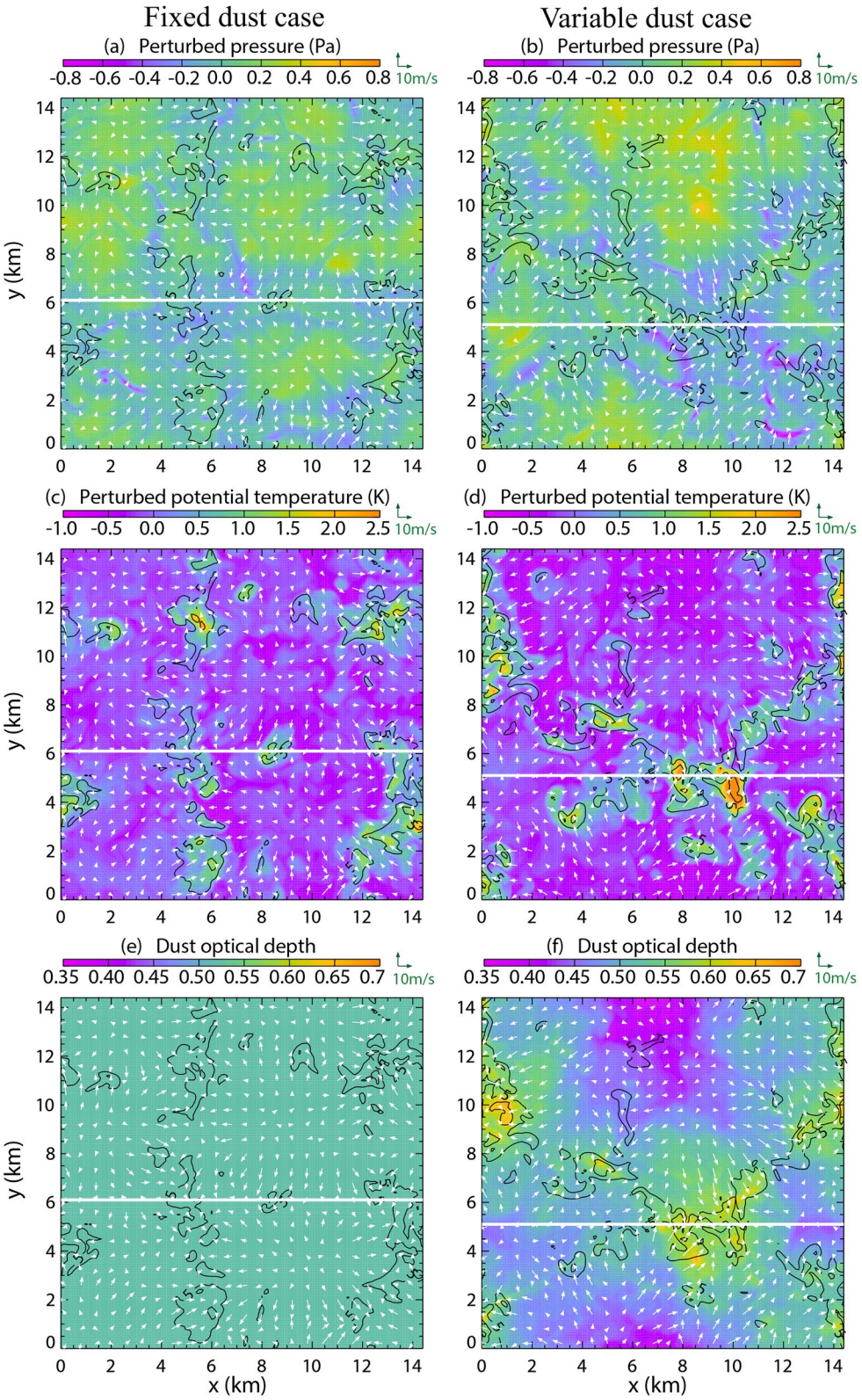
Fixed dust case
Variable dust case
(a) Perturbed pressure (Pa)
(b) Perturbed pressure (Pa)
-0.8 -0.6 -0.4 -0.2 0.0 0.2 0.4 0.6 0.8
10m/s
(c) Perturbed potential temperature (K)
(d) Perturbed potential temperature (K)
-1.0 -0.5 0.0 0.5 1.0 1.5 2.0 2.5
(e) Dust optical depth
(f) Dust optical depth
0.35 0.40 0.45 0.50 0.55 0.60 0.65 0.7
y (km)
x (km)
0 2 4 6 8 10 12 14

Figure 5.

the FD cases, the spatial average CBL depth shows the opposite, demonstrating that more complex behavior exists than is captured by spatial averages.

Figures 3b and 3e show the domain average updraft velocity and the mass-weighted TKE within the mixed layer, respectively, for the VD cases. Throughout the development of the CBL, from roughly 8 LT to about 14.5 LT, both the updraft velocity and the TKE show a weak trend with increasing optical depth. While by 14.5 LT, the CBL depth is already 1 km higher for VD6 than for VD3 (7.5 vs. 6.5 km: an increase of 15% for a doubling of optical depth). In the mature CBL after 14.5 LT, both the updraft speeds and TKE fall rapidly with local time. By late afternoon (17 LT), the updraft speeds and TKE both also fall rapidly with optical depth (Figures 3c and 3f). The trends before 14.5 LT suggest that unlike for the FD cases (c.f., Figure 3a vs. Figure 3b and Figure 3d vs. Figure 3e), the vigor of CBL turbulence is largely insensitive to the dust optical depth (for the intermediate optical depths examined) during the period of free convection onset and the strongest thermal forcing. Since the mass-weighted TKE is nearly insensitive to the optical depth and the CBL depth increases significantly with increasing optical depth, more TTKE is involved in thermal turbulence as the optical depth increases. The insensitivity of the updraft speed and TKE to optical depth, and the increase in total CBL TTKE with increasing optical depth suggest that the inhomogeneous dust cases have more energy flowing into CBL turbulence as the dust optical depth increases, whereas the energy flowing into CBL turbulence strongly decreases with increasing optical depth in the FD cases. This in turn suggests that the dust inhomogeneity has an impact that is, sufficient to more than offset the effect of shading of the surface.

Before examining variable dust in the LES in more detail, it is useful to take a closer look at how the dust optical depth is changing in these simulations and to provide a quantification for the inhomogeneity of the dust. As described in Section 2, dust is injected at the surface based on the surface wind stress, transported/mixed by resolved winds and diffusively mixed by the SGS eddy parameterization. As such, the dust optical depth changes over time in the simulations. The evolution of the domain average optical depth is shown in Figure 4a as the solid lines. For all cases, the average optical depth increases over the course of the day. Also shown in Figure 4a, as the dashed and dotted lines are the domain minimum and maximum column optical depth across all columns (2D grid). For VD6, the spatial differences in column optical depth can be quite dramatic: for example, at 14 LT the minimum optical depth is <0.4 while the maximum is almost 0.7. The differences between the maximum and minimum column dust opacity for the four cases (VD3, VD4, VD5, and VD6) are ~0.04, ~0.15, ~0.25 and ~0.4 at 14.5 LT. In all cases, the inhomogeneity decreases after about 14.5 LT as the TKE and updraft speeds decrease (c.f., Figures 3b and 3e). In order to more conveniently compare cases with different lateral dust inhomogeneity, we have defined a Dust Inhomogeneity Index (DII):

$$\mathrm{DII} = \frac{\sigma}{\tau_{\mathrm{avg}}} \tag{5}$$

Where σ is the standard deviation of the column dust optical depth over the whole domain at a given time, and τ_{avg} is the corresponding average optical depth. The DII is shown as in Figure 4b. The DII grows as the CBL TKE increases and as the CBL develops stronger vertical plumes, reaching peak values of 0.02, 0.05, 0.08 and 0.1 at 14 LT. The DII then falls as CBL mixing strength and the rate of dust lifting from the surface (not shown) decrease. This trend reflects the increasing concentration of freshly mixed dust into increasingly strong plumes during the morning and early afternoon development of the CBL followed by the lateral mixing and diffusion of this dust in the later afternoon.

5. Feedback Between Dust Inhomogeneity and CBL Dynamics

The simulations described in Section 4 shows that the presence of laterally inhomogeneous dust significantly modifies the CBL compared to simulations with similar total optical depths but with the dust uniformly distributed. In this section, we take a closer look at one of these cases to examine how the dust is distribut-

Figure 5. Comparison of large eddy simulation (LES) output at 13.5 LT from (left column) the fixed dust "FD5" case and (right column) variable dust "VD6" case (see text for the case label definitions), both with domain average $\tau = 0.5$ optical depth. Panels (a) and (b) Show the perturbation pressure at ~70 m above the surface, (c) and (d) Show the perturbation potential temperature at ~2 km above the surface, and (e) and (f) Show the column-integrated dust optical depth. In all cases, the white vectors indicate the horizontal wind at ~70 m above the surface. The black contour lines show areas of strong updrafts at ~2 km above the surface, with the outer contours showing areas with >5 m/s upwelling (inner contours are at >10 and >15 m/s). The horizontal white lines across each plot indicate the location of the cross sections through each LES shown in Figure 6.

ed in the variable dust cases relative to CBL dynamical structures, how the CBL large eddy structures are modified, how the presence of the variable dust changes the radiative heating rates, and how these radiative heating rate changes modify the CBL TKE budgets.

To more closely compare the fixed and variable dust LES, in this section we show results from the fixed dust scenario case FD5 and the variable dust scenario case VD6 at 13.5 LT. At this local time, both simulations have the same domain-average optical depth (and the same top-of-atmosphere insolation), and the DII for the variable dust scenario is at its maximum (Figure 4). This specific example pairing is shown for illustrative purposes, but similarly controlled comparisons at different local times during CBL development and for different total optical depths exhibit similar qualitative behavior to that described here.

5.1. CBL Large Eddy Structures in Fixed and Variable Dust Cases

Figure 5 shows the full lateral extent of the LES domains for the FD5 and VD6 cases, with Figures 5a and 5b showing the perturbation pressure at about 70 m above the surface, where the perturbation is the deviation from the horizontal domain average. The relatively thin, blue-to-purple regions in these plots indicate the lower pressure at the base of the CBL quasi-cellular convection, within the upwelling cell walls. The redder areas indicate higher pressure within the downwelling centers of the cells. The white vectors illustrate the lateral wind field at 70 m altitude, showing flow converging toward the low-pressure lines and diverging away from the high-pressure centers. The black contours on these plots show the coincident locations of the cellular updrafts above the low-pressure lines (the contours in Figure 5 are the vertical updraft speeds at 2 km). The significantly larger range of the perturbation pressure values in Figures 5a vs. 5b, the generally larger wind vectors (whose length indicates wind speed, also refer to Figure 11 for the statistics of the wind speed frequency of occurrence), and the tighter definition of the updraft speed contours, all suggest the large eddy cellular convection is significantly more vigorous in VD6 *vs*. FD5. This more vigorous convection is also associated with a larger scale of the Bénard-like convection cell structures (illustrated by the greater depth of the CBL).

The increased vigor of the cellular convection apparent in Figures 5a vs. 5b are directly related to the higher perturbation potential temperatures at 70 m (shown in Figures 5c and 5d) within the low-pressure regions of the cells (again, perturbation is the deviation from the lateral domain average). The perturbation potential temperatures show a greater fraction of the low-pressure cell boundary having higher perturbation potential temperatures and a larger area of peak values in the VD6 case *vs*. FD5. In turn, the higher peak potential temperatures are associated with high total column optical depths (shown in Figures 5e and 5f). While both cases have the same domain average optical depth (0.5), the VD6 case has peak dust optical depths aligned along the convergent, upwelling walls of the cellular convection, with peak values up to 0.7, while in the broader downwelling and divergent high-pressure cellular centers, the atmosphere is much clearer, with optical depths as low as 0.35.

The effect of the cellular convection in concentrating dust into the upwelling walls of the cell is better illustrated in Figure 6, which shows lateral (x-z axis) slices from FD5 and VD6 along the white lines indicated on Figure 5. For FD5 (shown in Figure 6a), the incremental optical depth (the optical depth from the top of the atmosphere down to each height) is prescribed hence is by definition uncorrelated with the vertical cellular motions, which are illustrated with the white vectors. By contrast, significant concentration of the incremental dust optical depth in the updraft of a large eddy convection cell for case VD6 is very clearly evident in Figure 6b. An instantaneous snapshot of the dust mass mixing ratio behind the optical depth distribution provides a clearer indication of the connection between the convection cell and the dust (Figure 6c). Near the surface, the wind both lifts dust into the atmosphere (due to the wind stress lifting parameterization, Section 2) and concentrates this dust into the base of the upwelling plumes along the convergence zones of the base of the upwelling cellular walls. The dust then rises with the thermals (plumes) in the updraft areas. Indeed, at this local time, the mean CBL depth in VD6 is 6.5 km, and thus Figure 6c shows that some of the dust can rise all the way up to the top of the CBL and overshoot into the free atmosphere above. In reaching the upper part of the CBL, the air begins to diverge and then to subside. The dust is laterally spread in the upper CBL by these divergent winds and is mixed with the air in the subsiding portion of the CBL under the influence of smaller scale resolved and SGS unresolved turbulence. During the period of strongest development of the CBL, the lofting and entrainment of dust within the upwelling zones is more efficient than the

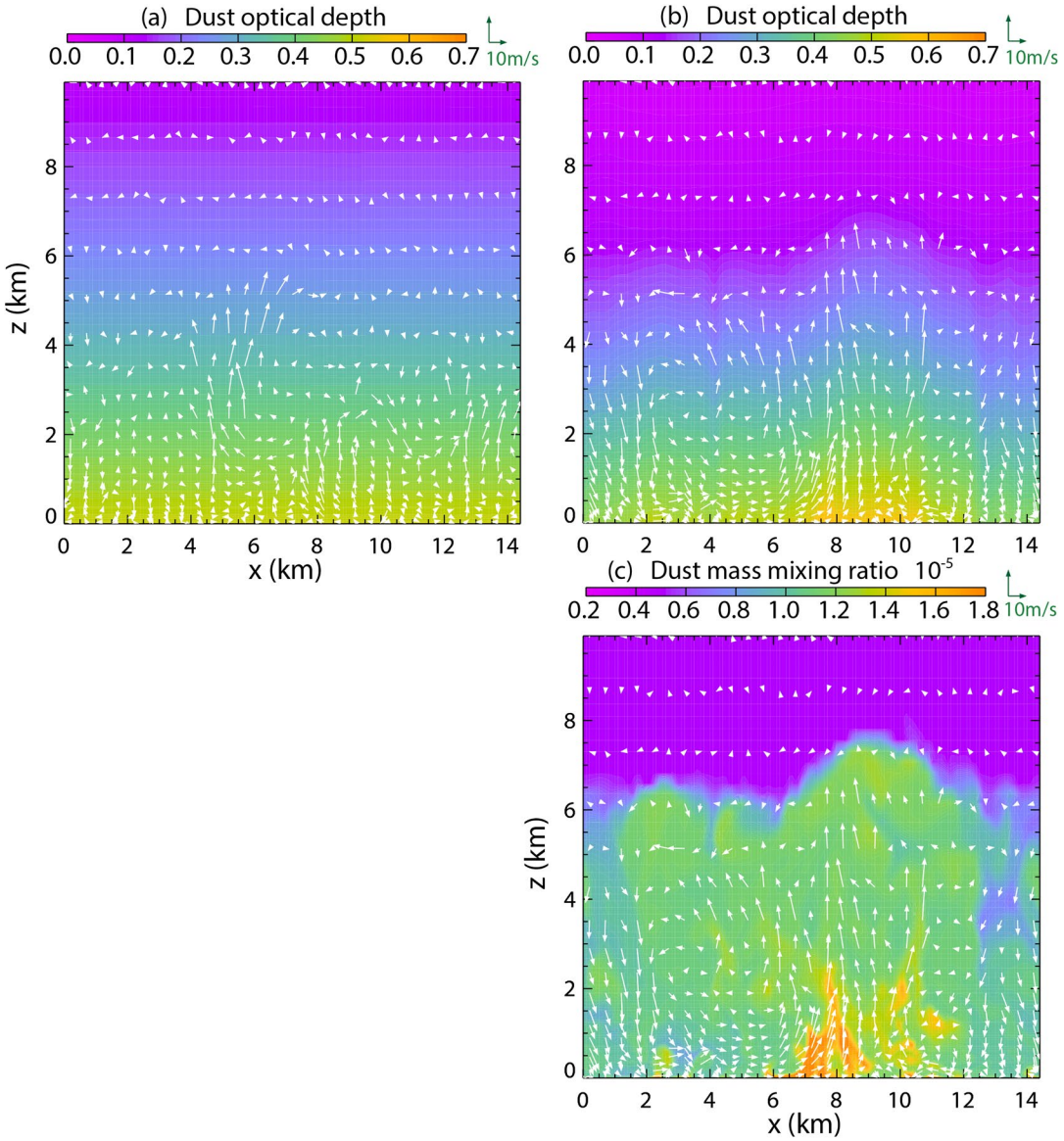

Figure 6. Cross sections of (a) and (b) the incremental dust optical depth (i.e., the value in each plot indicates the total visible optical depth of dust from the top of the atmosphere down to that point in the atmosphere), and (c) the dust mass mixing ratio. Panel (a) is for the fixed dust FD5 case while panels (b) and (c) are for the variable dust VD6 case. The mass mixing ratio is not shown for the fixed dust case since it is by definition laterally uniform and nearly uniform in the vertical. The white vectors in each plot represent the horizontal and vertical (x-z) wind field. The cases shown are from the same large eddy simulation at the same local time as Figure 5. The location of the cross sections are indicated in Figure 5 by the white horizontal lines.

lateral mixing, and very significant (factor of 4–5) lateral contrasts of dust mass mixing ratio can develop within the lowest few 100 m of the CBL (Figure 6c). These relative contrasts are sufficiently large that they may be observable from a rover or lander camera with suitable image processing when active dust lifting is ongoing, and indeed several such dust lifting events may recently have been captured by the Perseverance rover.

The degree of dust concentration within the large eddy updrafts can be statistically evaluated by performing a correlation analysis between perturbation dust mass mixing ratio and the perturbation vertical wind speed for each point in the horizontal domain, at each altitude, and for each local time. Figure 7 shows the variation of this correlation index with local time and altitude for the VD6 case. We can see that the correlation region with index values larger than 0.5 grows with the CBL depth until 15 LT, after which it

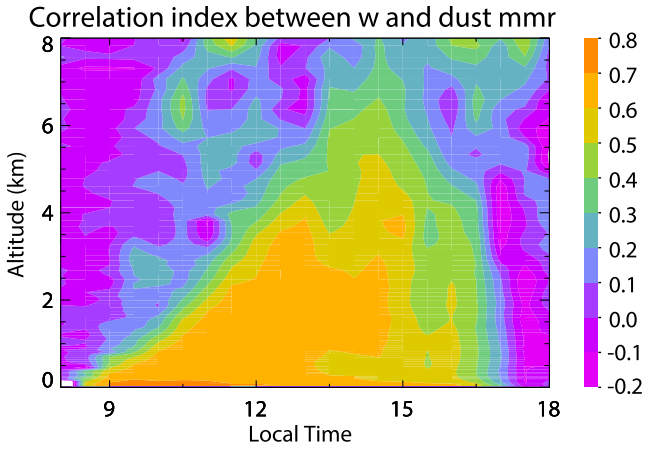

Figure 7. The correlation index between the vertical wind speed and the dust mass mixing ratio for the VD6 case as a function of local time and altitude.

begins to decrease. This corresponds to the evolution of the DII shown in Figure 4, which also starts to fall after 15 LT. Figure 7 demonstrates that throughout the domain dust tends to concentrate in the updrafts during the entire growth period of the CBL.

5.2. Direct Radiative-Dynamical Feedback Associated With Inhomogeneous Dust Radiative Heating

The Martian CBL is much more strongly radiatively driven than is that of the Earth due to the lower atmospheric density and heat capacity (Gierasch & Goody, 1968; Michaels & Rafkin, 2004; Spiga et al., 2010). In addition, unlike the Earth, latent heating due to water exchange is negligible compared to the sensible and radiative heating in the energy budget of the Martian CBL. Hence, radiative-dynamical feedbacks due to the kind of dynamical concentration of dust described in Section 5.1 could be significant in the CBL. It is important to note that while thermal emission dominates over the sensible cooling of the *solid surface* during the daytime on Mars (Kieffer et al., 1976), the corresponding heating of the *lower atmosphere* is much more equally accomplished by sensible and thermal infrared exchange. The reason for this near equal role of sensible and infrared radiative heating for the lower CBL is that while all the sensible heat loss from the surface is deposited in the lower atmosphere, much of the thermal emission from the surface is at wavelengths that pass through the atmosphere with little or no further interaction (i.e., at wavelengths outside of the CO_2 15-micron band). We discuss the heating of the lowest layer of the atmosphere more completely and quantitatively in Section 6.5, below. Here, we simply note that the Martian CBL is typically roughly equally radiatively and convectively driven and it is not generally dominantly radiatively driven.

In order to quantitatively illustrate the importance of radiative heating due to dust inhomogeneity, Figure 8 shows the total visible heating rate at roughly 1 km above the surface and at 13.5 LT for both the FD5 and VD6 cases. Since the visible heating is due almost exclusively to dust absorption, the FD5 case (Figure 8a) shows essentially no lateral variations, with a heating rate of ~1.6 K/h that varies by less than 1% across the lateral domain. The VD6 case (Figure 8b), on the other hand, shows significant variations in the heating rate consistent with the large variations in optical depth (Figure 5f). The heating rate varies from about 1.6 K/h to about 3.5 K/h, thus yielding a peak heating rate in the domain at this level and local time that is, about a factor of 3 higher than the minimum heating rate (i.e., there exists a maximum lateral horizontal heating contrast of about 2 K/h or a factor of 3 in total magnitude). The heating maxima and minima occur in close association with the perturbation potential temperatures that are also shown in Figure 8b, again showing that the lateral dust distribution (which controls the visible heating rate) is strongly correlated with the warm upwelling plumes/upwelling walls of the large eddy CBL convection.

Figure 9 shows cross sections of the visible, infrared, and total heating rates at the locations indicated on Figure 8 by the white horizontal lines. The FD5 case illustrates some general features of the lower atmospheric energy budget. With a nearly uniform horizontal and vertical distribution of dust opacity, and only a very minimal amount of solar absorption by atmospheric gases, the visible heating rate is also rather uniform. By contrast, the infrared heating rate is dominated by the strong net absorption of the upwelling infrared radiation from the surface by the cooler atmospheric CO_2 in the lowest reaches of the CBL (Gierasch & Goody, 1968; Savijarvi, 1999; Savijarvi et al., 2004). During this portion of the day (13.5 LT), the net heating rate shows the rapidly vertically decaying signature of the infrared heating by absorption of surface radiation within the lowest 1–2 km, superposed on the much more vertically uniform and weaker solar heating of suspended dust (Figures 9a, 9c and 9e).

The presence of dust concentration in the plumes is illustrated by the structure in the visible heating rate from the VD6 case (Figure 9b). The visible heating rate also dominates the total heating rate above about 500 m–1 km (Figure 9f). Here, there is significant enhanced solar heating within the thermal plumes, generating the factor of 3 difference in visible heating rate magnitude between the upwelling thermal plume

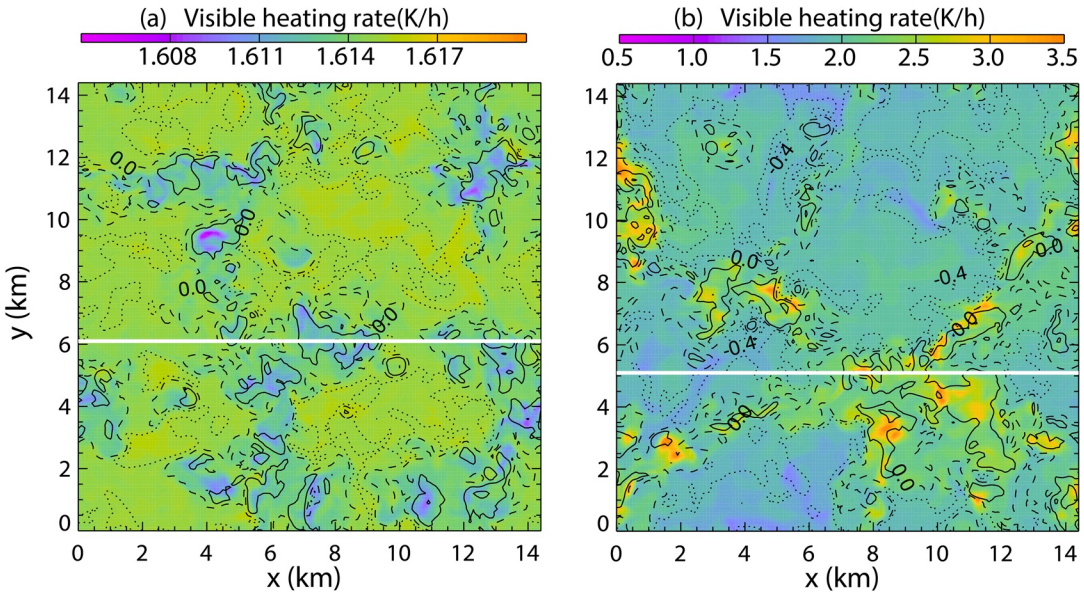

Figure 8. Visible heating rate in units of Kelvin per hour (K/h) (color shading) and perturbation potential temperature (contour) at roughly 1 km above the surface from (a) The fixed dust FD5 case and (b) The variable dust VD6 case at 13.5 LT. For the potential temperature, dotted, dashed and solid lines indicate negative, 0, and positive values, respectively. The white horizontal lines indicate the location of the cross sections displayed in Figure 9. Note that the color scales between panels (a and b) are vastly different (a covers a range of 0.015 K/h, while b covers 3 K/h).

core and the downwelling zone mentioned previously at the roughly 1 km level. As with the horizontal slices through the model (comparing Figure 5f and Figure 8b), the large values of the visible heating rate are highly correlated with large values of the dust mass mixing ratio in vertical cross section (Figures 6c vs. 9b).

The lateral differences in heating rates are only of consequence for convection intensity if they generate a significant augmentation of the potential temperature differences between the upwelling versus the downwelling portions of the convection cells. This depends not only on the heating rate but also the length of time that the air spends in the region experiencing the excess heating, which in turn depends upon the overturning timescales of the large eddies. We can estimate the uplift timescale from the CBL vertical velocity scale, W^*, modified from its traditional form (e.g., Stull, 1988) to account for the more volumetric heating of the lower CBL by Spiga et al. (2010). The modification simply relaxes the traditional assumption that this heat is predominated injected by the sensible heat flux directly at the surface interface. The modified Deardorff velocity is given by:

$$W_* = \left[g z_t \frac{\langle w'\theta' \rangle_{\max}}{\langle \theta \rangle} \right]^{1/3} \tag{6}$$

where z_t is the CBL top height, $\langle w'\theta' \rangle_{\max}$ is the maximum (as opposed to the traditional near surface) buoyancy flux (where primes indicate the perturbation from the horizontal average), and $\langle \theta \rangle$ is the domain average mixed layer potential temperature. Taking the value of 4–6.5 m/s as shown in Figures 13a and 13b, the time for air to cycle from the surface to the top of the CBL (about 6 km in this case) is ~20 min. For a heating rate contrast between the warm and cool branches of the large eddy cell of ~2 K/h, this yields about 0.5–1 K lateral contrast due solely to the differences in visible radiative heating rates in the upwelling and downwelling thermals. The range of 0.5–1 K can be compared to the observed potential temperatures in Figures 5d, 9b, 9d and 9f. Above about 1 km, most of the positive potential temperature perturbation is clearly associated with the visible dust heating. The reduction of the thermal contrasts in the upper portion of the plumes is due to mixing (entrainment) between air in the thermal plume and the background atmosphere.

The warming of the dusty updrafts in the VD cases increases their positive buoyancy relative to the FD cases, which leads to a strengthening of the vertical motions in the CBL for VD cases relative to the FD cases at the same domain-average optical depth. Figure 10 shows the vertical wind speed distribution (the

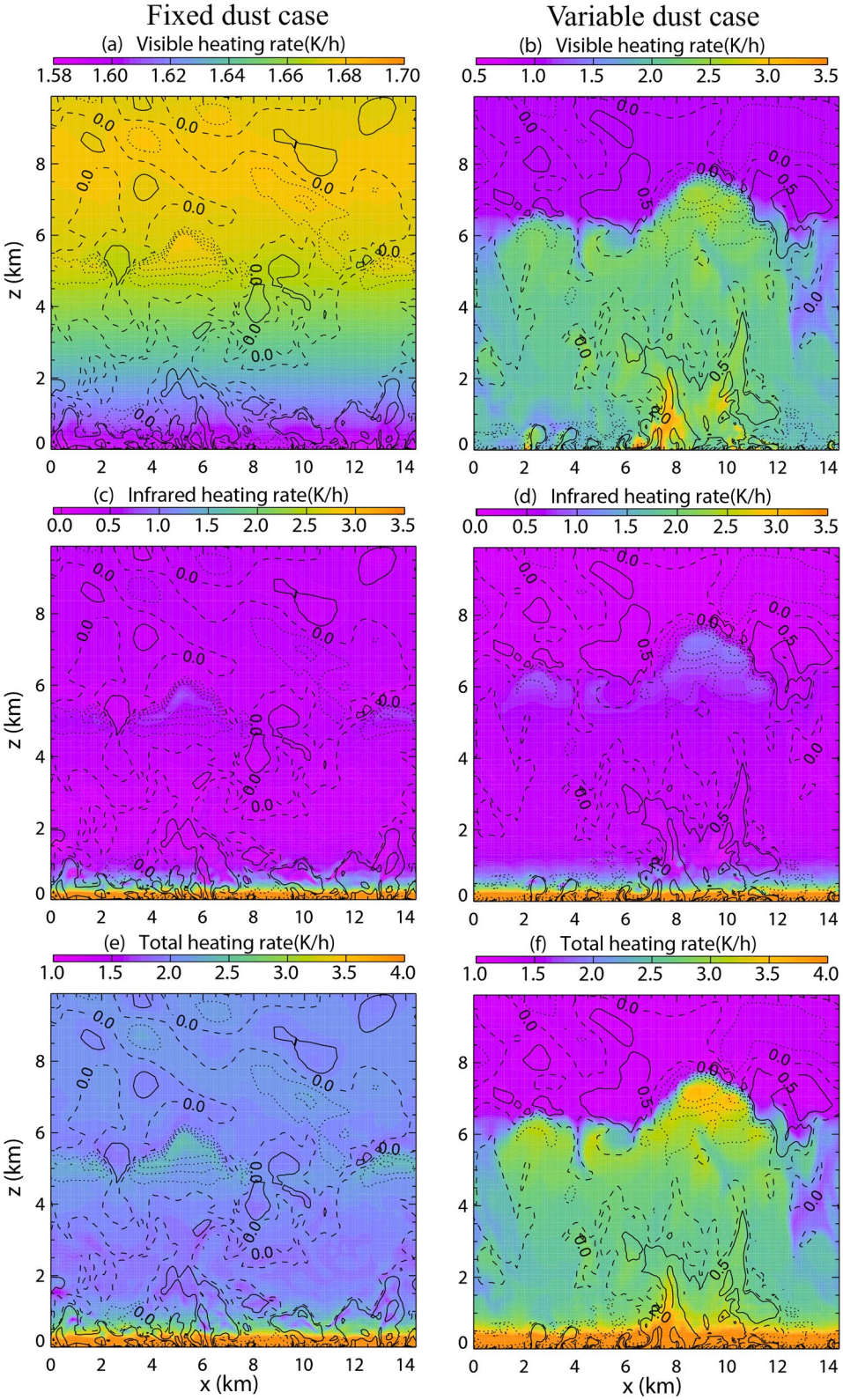

Figure 9. Cross sections of the (a) and (b) Visible, (c) and (d) Infrared, and total radiative (e) and (f) Heating rates for the FD5 (left column) and VD6 (right column) cases. For all plots, the contours show the perturbation potential temperature, with dotted, dashed and solid lines indicating negative, 0, and positive values, respectively. The profiles are located within the domains shown in Figure 8 and their locations are indicated by the white horizontal lines. Note that the color scales between panels (a and b) are vastly different (a covers a range of 0.12 K/h, while b covers 3 K/h).

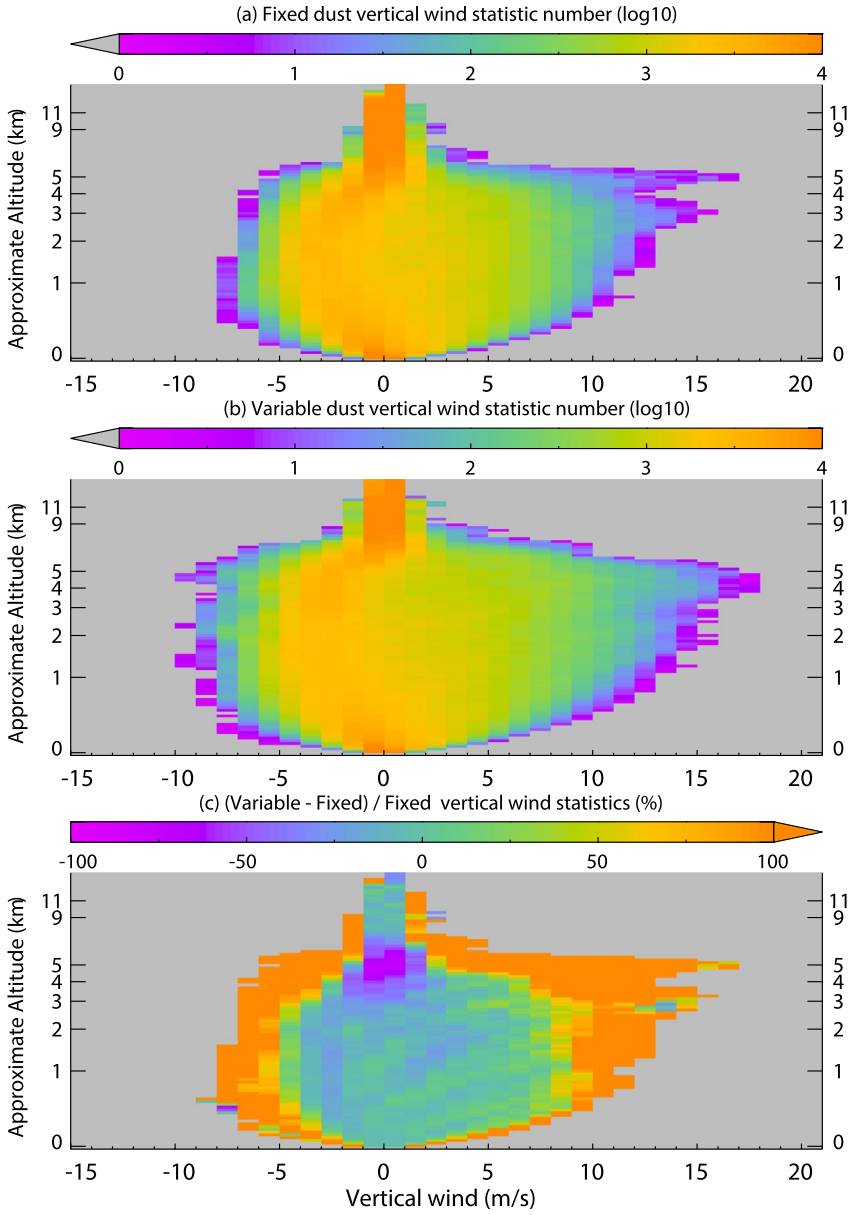

Figure 10. Variation of the vertical wind speed frequency of occurrence with altitude and vertical wind speed at local time 13.5 LT, using a bin size of 1 m/s. (a) Fixed dust scenario with dust optical depth of 0.5, (b) Variable dust scenario with averaged dust optical depth of ~0.5 and (c) The relative variable minus fixed case difference in percentage normalized by the fixed dust case. The vertical wind speed frequency of occurrence is simply the number of grid cells at each level that have vertical wind within a given speed bin, plotted on a log10 scale (there are 21,025 total grid cells at each model level). The speed is binned with an increment of 1 m/s.

number of grid cells at a given level within a given vertical wind speed bin) as a function of altitude. The vertical discretization in Figure 10 corresponds to the model vertical mesh, while the vertical wind speed is sorted into 1 m/s bins. Both the FD5 (Figure 10a) and VD6 (Figure 10b) cases are shown for 13.5 LT. Both panels show that the vertical wind is generally small near the surface, where buoyancy has not yet had a chance to vertically accelerate the air, and in the free atmosphere above the CBL top. Within the interior of the CBL, the positive and negative vertical wind speed extremes correspond to the upwelling plumes and the downwelling zones of the convection cells, respectively. The largest vertical wind speed magnitudes appear within the upwelling plumes in the upper part of the CBL, with maximum values of 17 m/s for FD5 and 18 m/s for VD6.

Figure 10c shows the relative difference between the two simulations and demonstrates the greater occurrence of higher wind speed magnitudes of both signs in the VD6 case versus the fixed dust FD5 case. Wind speeds larger than +10 m/s (upward) and less than −5 m/s (downwards) are more prevalent in VD6 than FD5 at most altitudes, suggesting that both the updrafts and downdrafts are stronger in the variable dust case. Specifically, we can see a significant difference in the upward wind between 1 and 2 km altitude, corresponding to the maximum VD6 dust visible heating rates in the updrafts shown in Figure 9b. The large difference at 4–6 km, however, is due to the difference of the CBL depths between the two cases (∼6 km for VD6 but ∼5 km for FD5). The lateral domain average vertical wind speed of the updrafts for VD6 is also much larger than that for FD5 at all altitudes.

Stronger vertical motion in the VD6 up- and downdrafts must be supported by more rapid horizontal motions near the base and tops of the large eddies. This is indeed illustrated by the frequency spectrum of horizontal wind speed shown in Figure 11. The larger horizontal wind speeds for VD6 suggests that the whole Bénard-like convection cell circulation is enhanced. The higher frequency of occurrence of large horizontal wind speeds near the surface (8–13 m/s as shown in Figure 11c) suggests that more dust may be lifted and concentrated into updrafts when radiatively interactive dust is treated. This would create a positive feedback for the dust lifting process, but it is strictly the wind stress at the surface that is, important for dust lifting rather than just the wind speed, and we will return to this issue in the discussion section. It should also be noted that as a background wind is applied, the convection tends to change from polygonal Bénard cells into convective roll (or street) structures. These rolls have greater anisotropy than Bénard cells and hence high rates of turbulent mixing (e.g., Stull, 1988), and thus the feedback on dust lifting may have even greater potential when there is a background wind in which the convection is embedded.

5.3. Indirect Radiative-Dynamical Feedback Associated With Surface Shading

Figure 12 shows the lateral distribution of the ground and lowest layer air potential temperatures in the FD5 and VD6 cases at 13.5 LT. While the lateral average ground temperature is very slightly cooler in FD5 (268.1 K) versus VD6 (268.4 K), comparison of Figures 12a and 12b show that there is a much greater variation within VD6 (about 1.4 K variation vs. about 0.8 K for FD5). The areas of enhanced ground temperature in VD6 are under the downwelling regions of the open cellular convection, for reasons described below. The excess thermal emission from the surface in the downwelling regions of VD6 versus FD5 is thus about 1% and given that most of the atmospheric heating in the lowest ∼500 m of the atmosphere is due to thermal infrared radiative exchange with the surface, this corresponds to an augmentation of lowest layer atmospheric heating by this same factor. Within the convection cell, this corresponds to augmented surface-to-atmosphere exchange of heat in VD6 versus FD5, despite the fact that the lateral domain average dust optical depths and the resulting lateral domain average ground temperatures are nearly identical.

The reason that augmented ground temperatures occur under the downwelling centers of the convection cells in VD6 (*vs.* FD5) is that these regions are relatively clear of dust (Figure 5f) and hence receive more solar insolation. The relative concentration of dust in the upwelling plumes means that, for the domain average optical depth in VD6 to equal that in FD5 ($\tau = 0.5$), there must be a lower dust optical depth in the downwelling regions. Indeed, above the area of maximum ground temperature, the optical depth is as low as 0.35. Since the clearer downwelling regions have higher ground temperature and hence higher rates of near-surface atmospheric heating, the dust inhomogeneity generates a separate, secondary means of augmenting the thermal forcing of convection (in addition to direct heating of the dusty upwelling plumes, Section 5.2). The reason that the heating augments the circulation despite being under the downwelling regions is due to the fact that surface-atmosphere sensible and thermal infrared heat exchange occurs over a short vertical distance, and thus only significantly heats the lowest portion of the CBL (e.g., Figure 9d). Within this very lowest portion of the atmosphere, the air is strongly divergent away from the downwelling zones and convergent into the upwelling cellular edge sheets and plumes. The extra buoyancy deposited into the air due to the heating is thus advected into the upwelling zones where it enhances the cellular overturning. This lateral advection of buoyancy happens sufficiently quickly that vertical propagation of the buoyancy within the downwelling zone is overwhelmed, otherwise the heating distribution would instead act to slow the downwelling.

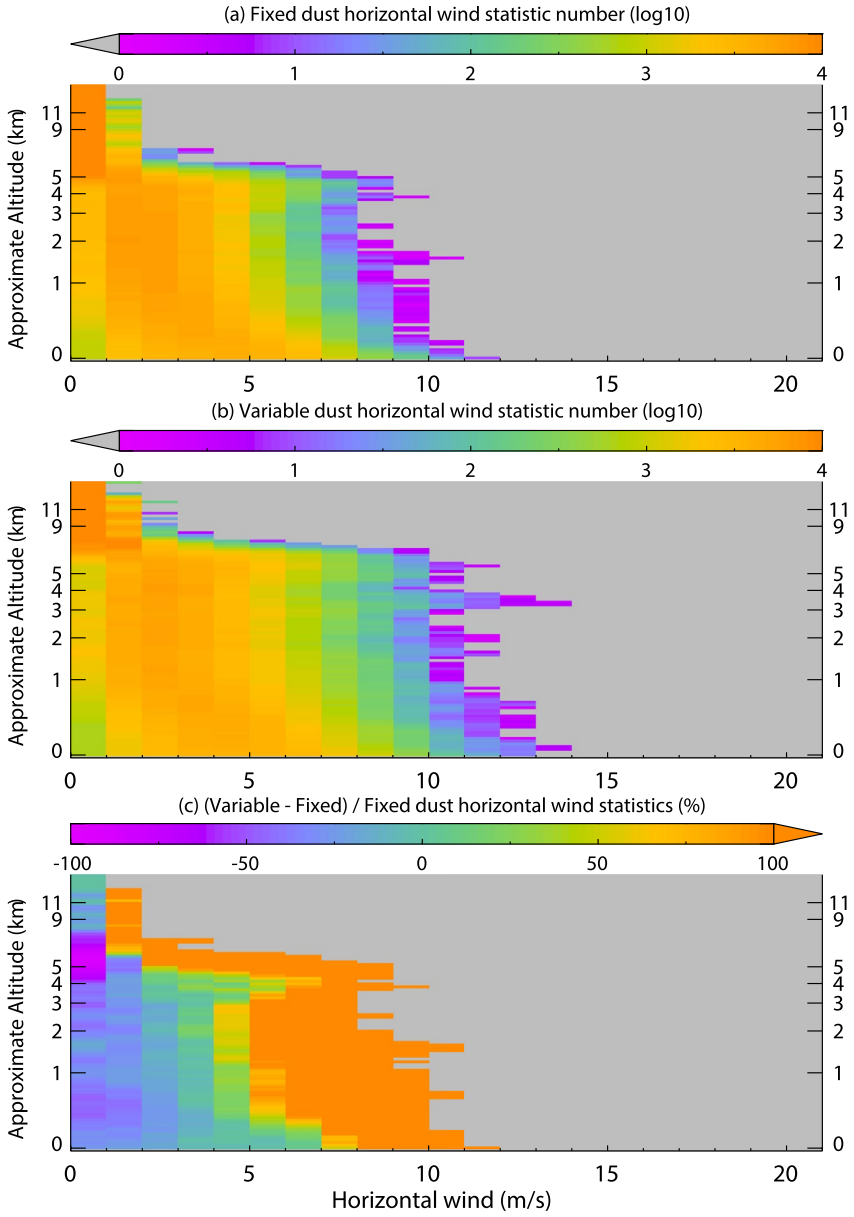

Figure 11. Same as Figure 10 but for the horizontal wind.

5.4. Efficiency of Surface-Atmosphere Heat Transfer

The lowest atmospheric layer domain average potential temperature in the FD5 is significantly higher (235.5 K) versus that in the VD6 case (232.2 K) at 13.5 LT (Figures 12c and 12d, respectively), despite VD6 having a very slightly higher ground temperature (the potential temperature difference is +3.3 K while the ground temperature difference is −0.3 K). The relative coolness of the VD6 near surface air is a result of the stronger convective motions (more vigorous overturning and faster near surface winds) and clearer downwelling regions in the variable dust case: with clearer and more vigorous downwelling, the VD6 Bénard-like cells are able to more effectively ventilate cool air down into the near surface divergence zones, and the air spends less time traveling horizontally within the near surface portion of the cell and thus has less time to absorb heat from the surface.

The increased downwelling of cool air we find in this case can be explained by looking at the radiative forcing of the inhomogeneous air. As the air from the upwelling plume laterally spreads and mixes at the

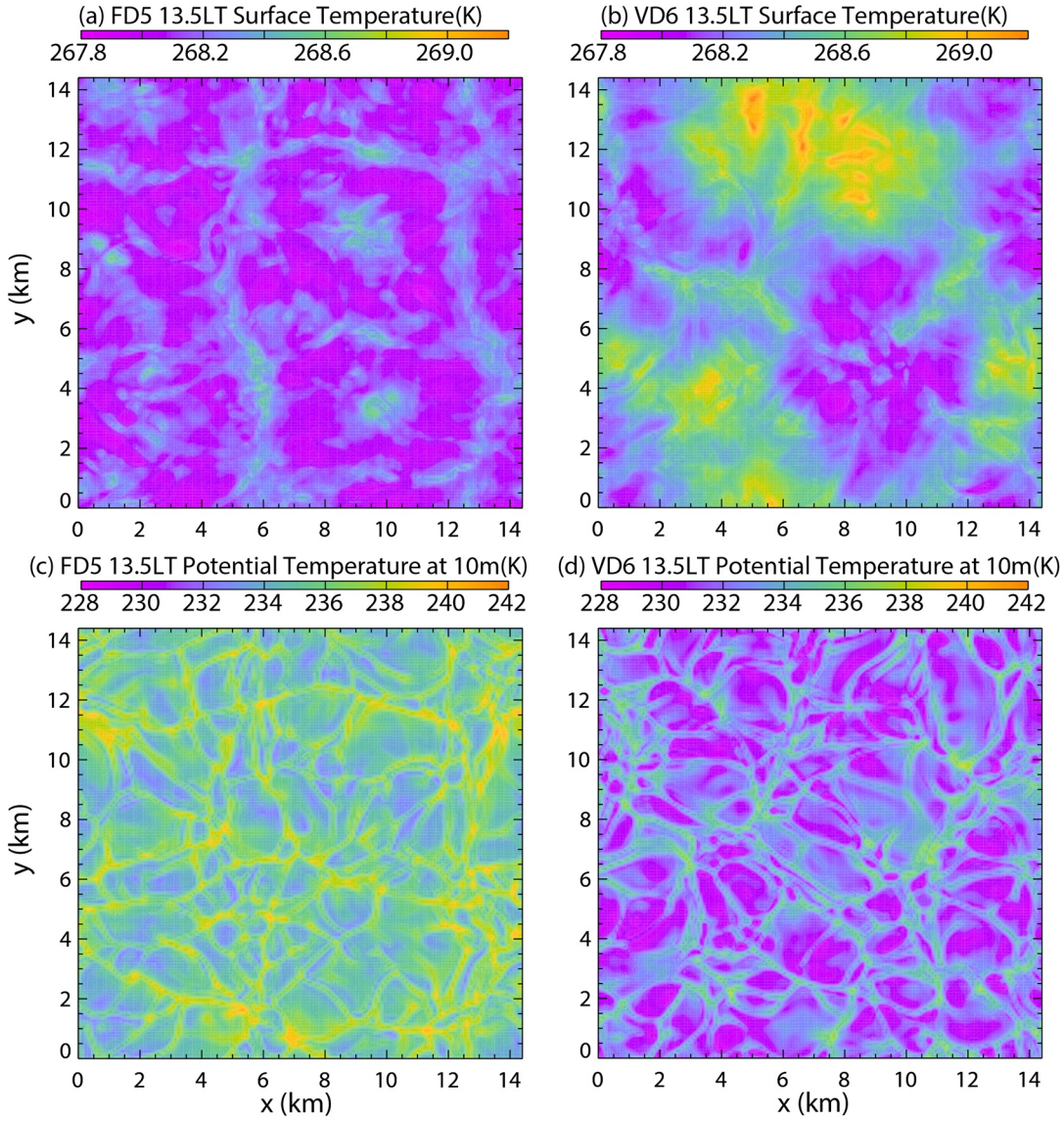

Figure 12. Surface temperatures (top row) and lowest layer air potential temperature (bottom row) at 13.5 LT for the FD5 (left column) and VD6 (right column) cases.

top of the CBL, the dust detrains and the mass mixing ratio of dust in the air decreases (e.g., Figure 6c). The decrease in dustiness means that the areas above the downwelling regions experience less solar radiative heating than do the upwelling plume sites (e.g., Figure 9b). Since the whole CBL increases in potential temperature over the Martian day (e.g., Figures 2g–2i), a relatively lower solar heating rate of the clearer air away from the upwelling plumes means that these nascent downwelling areas become *relatively* cooler despite not experiencing true net cooling (they are simply heating more slowly than the more recently arrived, dustier air). At any given moment, the potential temperature at the top of the CBL just before downwelling onset is comparable to that at the top of the super-adiabatic layer near the surface. But since the CBL temperature is not constant, but is in fact increasing rapidly throughout the period of strongly forced CBL motion, during the "circuit time" for air to descend (nearly isentropically) from the CBL top to the surface (about 10–15 Martian minutes) the near surface air potential temperature will increase by a few K. While the near surface air is diabatically heating because it is strongly radiatively (and convectively) coupled to the surface, the relatively clearer downwelling air is much less strongly radiatively heated. As such, it gets progressively relatively cooler by simply not heating as much as dustier air at the same level nor the near

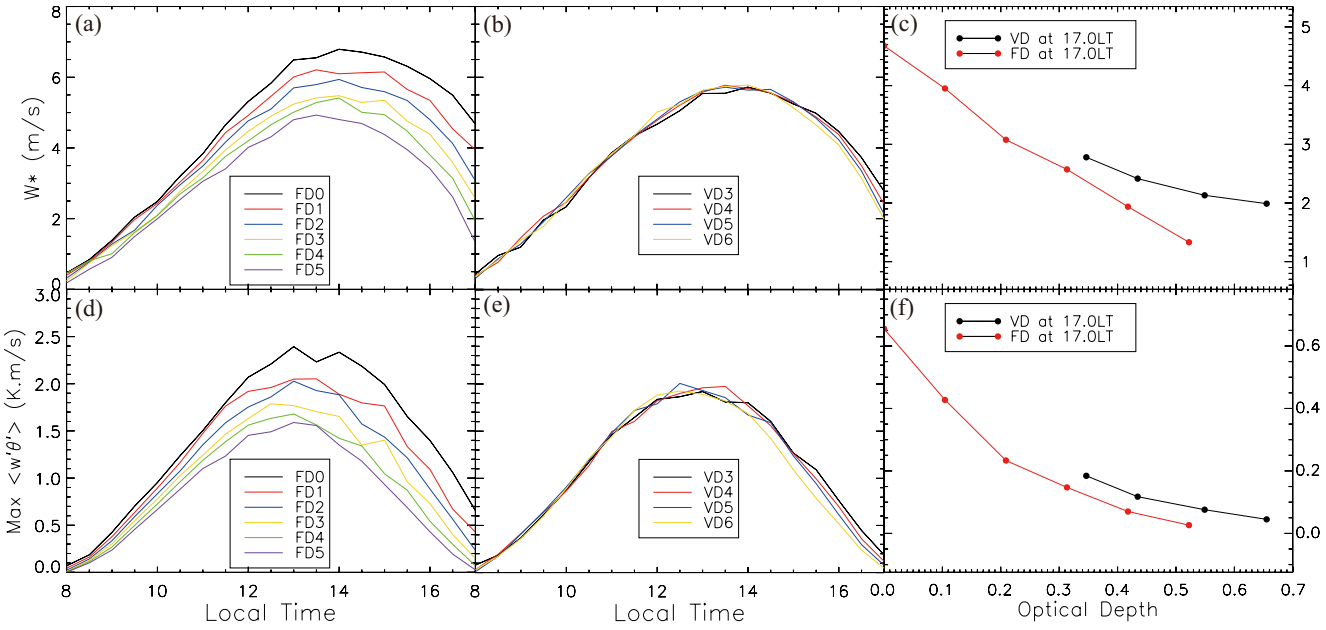

Figure 13. The evolution of (top row) the modified Deardorff velocity, W^*, and (bottom row) the maximum vertical turbulent heat flux. The meaning of the columns and of the line colors is otherwise the same as for Figure 2. W^* is a measure of the vertical turbulent wind scale, as defined in Section 5.2. Note that the y-axis ranges for the left and middle columns are the same but different from those of the right column.

surface air that is, more directly exposed to heating from the ground. As a result, recently arrived downwelling air is relatively cooler (and clearer) than near-surface air that has been at lower altitudes for longer. While more rapid downward motions tend to decrease this "time-lag" effective cooling of air brought down from the CBL top, the more rapid motions tend also to be associated with a deeper CBL and hence both a longer distance for those stronger downwelling plumes to traverse and a cooler CBL top. When the descending clear air final reaches and penetrates down into the superadiabatic lower portion of the CBL, the downwelling will also effectively "cool" relative to the surrounding air by warming (adiabatically) at a lesser "rate" than the superadiabtic air around it.

The difference between the surface temperature and the kinetic temperature of the lowest layer of the model is thus larger in the VD6 case (34.3 K vs. 30.7 K for FD5). This is about a 12% larger surface-atmosphere temperature contrast in the VD6 case than in FD5. The surface-atmosphere heat exchange is dominated by sensible and infrared heat exchange (both terms being about comparable in the simulations in this study, see Section 6.5) between these layers and for a given pressure, composition, and mean temperature, both depend strongly on the temperature difference. As such, the enhanced overturning of the cell driven by the direct heating of concentrated dust in the upwelling plumes (Section 5.2) and secondarily by the greater ground temperatures beneath the downwelling portions of the cell (Section 5.3) leads to cooler air over the surface and thus allows the cell to extract more energy from the surface. To be precise, the same energy is emitted from the surface (over the course of the simulations, the domain mean ground temperatures do not diverge significantly between FD5 and VD6), but more of this energy is deposited into the cellular motion in VD6. Inhomogeneous dust thus allows the CBL to convert more of the surface emission into turbulent kinetic energy.

The domain average modified Deardorff velocity, W^* (see Equation 6 and Section 5.2) for all the FD and VD cases is shown in Figures 13a and 13b as a function of local time, and in Figure 13c as a function of optical depth at 17 LT. These can be referenced to the difference between the surface temperature and the kinetic temperature of the lowest model layer shown in Figures 2j–2l. In these simulations, the surface-atmosphere temperature contrast is a good proxy for the net heat exchange between the surface and the atmosphere, dominated as it is by sensible and infrared heating of the atmosphere by the surface (where both depend on the difference between the surface temperature and the air temperature). Because all of the VD cases begin from an initial $\tau = 0.3$ state and significant differences in optical depth do not develop until the late

morning (after dust lifting has become significant), there are no differences in the surface/atmosphere temperature contrast evolution until just before noon (Figure 2k). This differs from the FD cases, for which the fixed optical depth differences between cases throughout the night and morning yield a steady-state shift of the diurnal surface temperature cycle to a lower mean value (for higher dust optical depths) and hence decreases the surface-atmosphere temperature contrast throughout the interval shown in Figure 2j. Once the increased optical depths start to influence the VD surface/atmosphere temperature contrasts after noon, the sign of the dependence on optical depth is the same of that as for FD, namely that the contrast decreases as the optical depth increases (Figure 2l).

The CBL velocity scale, W^*, decreases as the surface/atmosphere temperature contrast decreases for the FD cases (Figures 13a and 13c vs. Figures 2j and 2l). This suggests that as the near-surface forcing decreases, the vigor of convection also decreases, as we might expect. Comparing with Figure 2a, both the modified Deardorff velocity, W^*, and the CBL depth decrease with increasing optical depth (and hence decreasing surface-atmosphere temperature contrast). This is consistent with the idea that stronger forcing for thermal turbulence (in this case, near surface forcing) should lead to stronger vertical CBL motions and a deeper CBL.

However, Figure 13b shows a striking lack of sensitivity of the modified Deardorff velocity to the optical depth in the VD cases until early afternoon. A significant part of this seems likely traceable to the similarly striking insensitivity of the surface-atmosphere temperature contrast to dust optical depth for the VD cases (Figure 2k). In turn, part of this is due to the fact that the optical depth only begins to differ between the VD cases in the mid-to-late morning. However, W^* remains insensitive to the optical differences into the mid-afternoon (14.5–15 LT), at which time it starts to show the same sign of sensitivity as the FD cases, namely decreasing W^* with increasing optical depth (and decreasing surface/atmosphere temperature contrast). The fact that W^* has nearly identical trends with local time in the VD cases up to about 15 LT despite differences in the total optical depth suggests that when the dust can self-organize into plumes, increasing the domain-average optical depth (i.e., the lifting of dust at increasing rates) does not actually increase the vigor of the turbulence despite increasing the CBL depth. Note that this does not contradict our finding that at the same domain average optical depth, self-organized dust leads to more vigorous turbulence than a uniformly dusty atmosphere (e.g., Figures 10 and 11).

However, it must be cautioned that even the modified Deardorff velocity is defined assuming that the total heat input into the turbulence is based on heat transfer from the surface. When significant buoyancy is being added through visible radiative heating of the suspended dust in laterally inhomogeneous plumes, even the modified Deardorff velocity would decreasingly capture the true vigor of CBL turbulence. In this case, the turbulence is no longer free thermal convection, but has a forced component (the differential heating due to the dust) which becomes analogous in some ways—at least in terms of it not being pure free thermal convection—to moist convection.

5.5. Vertical Dust Distribution Differences Associated With Active Dust Lifting

The evolution of the domain average vertical potential temperature structure as a function of local time is shown for FD5 and VD6 in Figure 14. Comparing the two panels, Figure 14 clearly demonstrates the deeper extent and more rapid growth of the CBL in VD6. In both cases, the CBL depth can be estimated by finding the point in altitude where the isentropes (contours of constant potential temperature) are no longer nearly vertical (very near the surface, the isentropes transition to being nearly vertical from being nearly horizontal—this altitude, which illustrates the top of the superadiabatic layer, should not be confused with the higher-altitude CBL top). The thermal structure signatures of the CBL top are the basis for the FD5 and VD6 CBL depth curves in Figures 2a and 3a, respectively.

As well as being deeper than the FD5 CBL, the VD6 CBL is also cooler throughout its depth. This is consistent with the cooler near surface air temperatures discussed in Section 5.4. Despite the mean potential temperature in the CBL being slightly cooler in VD6, the difference between the updraft and downdraft potential temperatures in each simulation are quite similar (Figure 15).

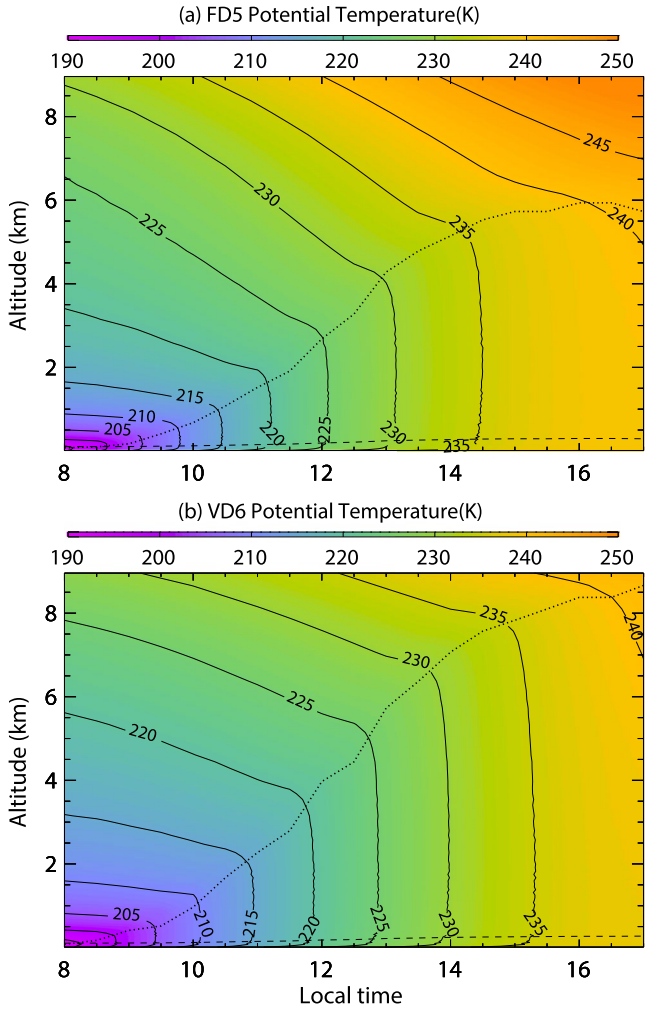

Figure 14. Domain average potential temperature as a function of altitude and local time for the (a) FD5 and (b) VD6 cases. Dashed lines and dotted lines indicate the super-adiabatic layer near the surface and the convective boundary layer top respectively.

At levels above the CBL, FD5 is warmer than VD6. This is attributable to the fact that the vertical distribution of dust prescribed in FD5 is more nearly vertically uniform than in VD6 (Figures 6a and 6b), which means that the heating of the atmosphere (primarily due to solar absorption by dust) is also greater above the CBL top in FD5 *vs.* VD6 (Figures 9a and 9b). The difference in heating rates above the CBL at 13.5 LT is about 0.7 K/h (Figures 9e vs. 9f).

5.6. Dependence of CBL Turbulence on Optical Depth and Local Time

Figure 16 shows the dependence of the surface-air temperature contrast, the CBL depth, the surface drag velocity, and the modified Deardorff velocity upon the domain-average optical depth at 13.5 LT and 15 LT. These plots complement Figures 2l, 2c, 3i and 13c, respectively, which show these values at 17 LT. The DII for the VD cases decreases from a maximum at 13.5 LT to nearly zero for all the VD cases after 17 LT (see Figure 4).

The surface-atmosphere temperature dependences upon optical depth at 13.5 LT and 15 LT (Figures 16a and 16b) both show the same sign of trend as at 17 LT (Figure 2l), with an increasing optical depth yielding a decreasing thermal contrast for both the FD and VD cases. However, the offset of the VD curves toward higher thermal contrast values for VD versus FD for the same optical depths is largest at the earliest local time and smallest at the latest local time. This is consistent with the difference in surface-atmosphere temperature being due to the dust inhomogeneity discussed in Sections 5.3 and 5.4, given that the DII decreases with time after 13.5 LT (Figure 4). The residual differences between FD and VD contrasts at 17 LT result from the differences in the time history of heating in the two sets of cases.

The CBL depth trend with optical depth is consistent at all three local times (Figures 2c, 16c and 16d). While across the FD cases, CBL depth decreases significantly with increasing optical depth, a strongly opposite trend is apparent at all three local times for the VD cases. The trend at 17 LT cannot be explained as a purely historical signature of earlier gains in CBL depth as the CBL is clearly still growing through to the end of this period, at least in the VD5 and VD6 cases (Figure 2b).

While the drag velocity (u^*) appears to have no difference in behavior with increasing optical depth in the VD and FD cases at 17 LT (Figure 3i), this is not the case at the earlier local times. In the midafternoon (15 LT, Figure 16f), while the mean drag velocity shows no difference between FD and VD, there is a very slight separation of trend in the one sigma deviation winds, and a higher maximum drag velocity in the VD versus the FD cases. At the time of peak DII (13.5 LT, Figure 16e), all three measures of the drag velocity are higher for the VD cases versus the FD cases. Thus, for the same domain average optical depth, dust inhomogeneity increases both the mean and extremum values of the drag velocity. The VD cases also do not show any meaningful trend with optical depth at this earlier local time, unlike the FD cases at this local time, and the FD and VD cases at the later local times. This suggests that the negative feedback of increasing dust optical depth upon dust lifting generated by convective wind stresses in the FD cases is not active in the VD cases when dust is most inhomogeneously distributed.

The modified Deardorff velocity (W^*) shows a change in trend with optical depth for the three local times examined (Figures 13c, 16g and 16h). At the two earlier local times, while for the FD cases W^* decreases as the optical depth increases, the VD cases are nearly independent of total optical depth. By 17 LT, the VD case W^* decreases with increasing optical depth, though at a slightly lower rate than the FD cases. These

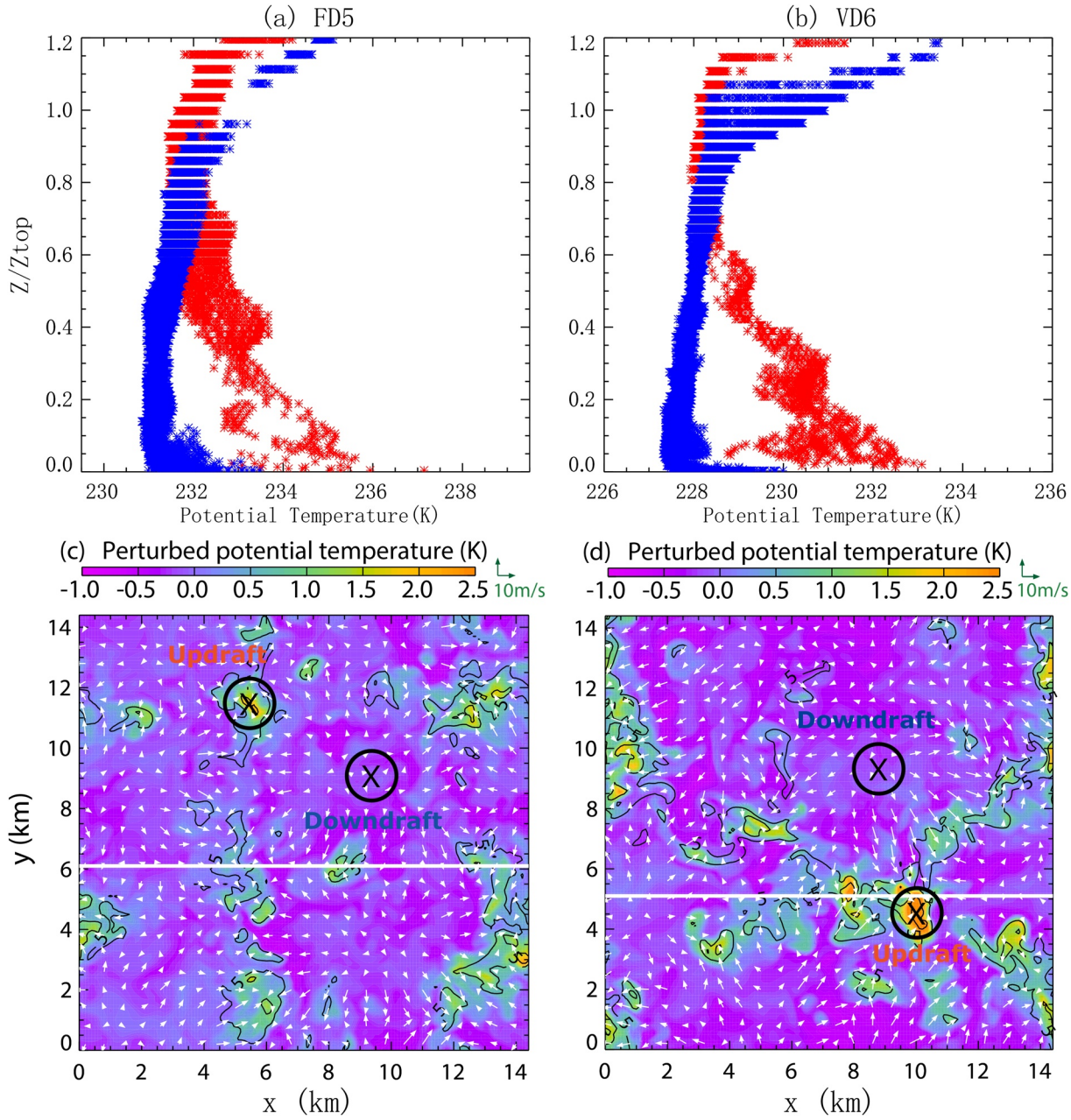

Figure 15. The potential temperature within (red) updrafts and (blue) downdrafts at 13.5 LT in the (a) FD5 fixed dust case and (b) the VD6 variable dust case. Updrafts are defined here as grid cells with updraft speeds exceeding 2.5X the standard deviation and downdrafts for which the downdraft speed excessed 0.5X the standard deviation. In both cases, only winds with the selected areas, indicated by black circles in panels (c) and (d), are included. The colored fields in panels (c) and (d) are the 2 km potential temperature with the white arrows indicating the horizontal wind at 70 m (these panels are the same as Figures 5c and 5d except for the updraft/downdraft labeling).

results suggest that when the DII is largest (and solar forcing the strongest), the effect of radiative heating of the self-organized dust distribution is able to compensate for the increased dust shading of the surface and hence maintain a near constant vigor of CBL turbulence (as diagnosed by W^*) as more dust is placed in the atmosphere.

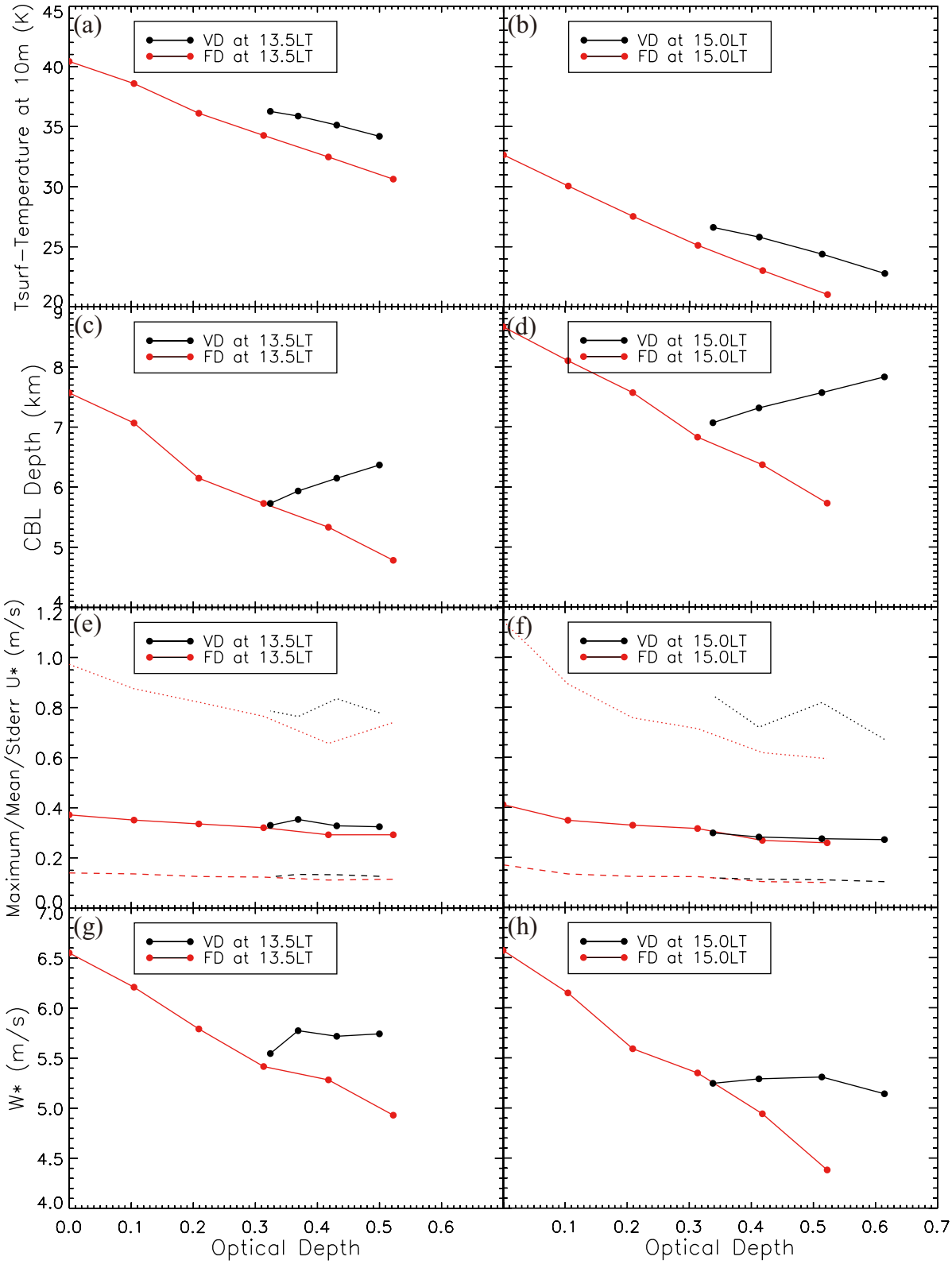

Figure 16. The dependence of various convective boundary layer (CBL) parameters upon optical depth for the Fixed Dust and Variable Dust cases at (left column) 13.5 LT and (right column) 15 LT. The parameters shown are (top row) the surface-atmosphere temperature contrast, (second row) the CBL depth, (third row) the drag velocity, and (bottom row) the modified Deardorff velocity. Values for these parameters and with the same plot-style are shown for 17 LT in Figures 2 and 3.

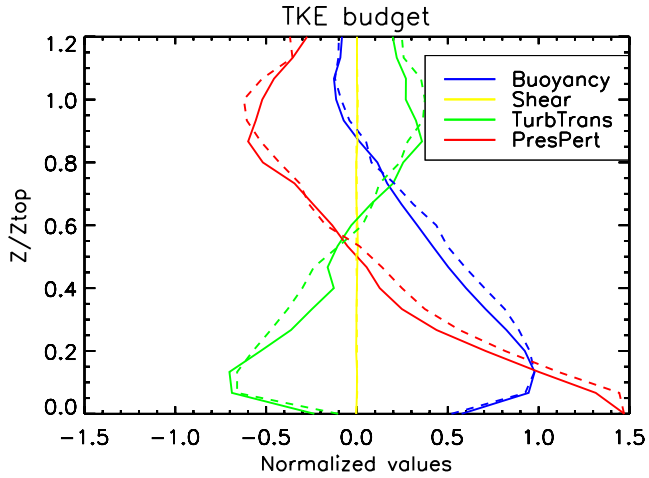

Figure 17. The four normalized turbulence kinetic energy budget terms. Solid lines for variable dust case and dashed lines for fixed dust case. All profiles are averaged between 9 and 16 LT (output every 30 min) and normalized by W^{*3}/z_{top}.

5.7. Modification of the TKE Budget Due to Inhomogeneous Dust Radiative Heating

The evolution of TKE is expected to follow the TKE tendency equation (written here following Equation 5.1b from Stull, 1988):

$$\frac{\partial\left(\langle \mathrm{TKE}\rangle\right)}{\partial t} = \frac{g}{\langle\theta\rangle}\langle w'\theta'\rangle - \langle u'w'\rangle\frac{\partial\langle u\rangle}{\partial z} - \frac{\partial\langle w'\cdot \mathrm{TKE}\rangle}{\partial z} - \frac{1}{\langle\rho\rangle}\frac{\partial\langle w'p'\rangle}{\partial z} - \varepsilon \tag{7}$$

The tendency equation says that the TKE at any level ought to evolve following the five terms on the right hand side of Equation 7, which are respectively, along with one letter labels we will use for these terms: (B) The buoyant production or consumption term, when the vertical heat flux $\langle w'\theta'\rangle$ is positive or negative, respectively; (S) The mechanical or shear production term; (T) The turbulent transport of TKE term; and, (P) The pressure correlation term. As we are mainly interested in the mechanisms by which TKE is generated, we have not calculated the dissipation, ε, which is the rate at which TKE is converted into thermal energy. Indeed, for steady state LES, ε is the usually calculated as the residual of the other terms necessary to have no net trend in TKE. With an evolving CBL (as in our simulations), it would be calculated from the model evolution of total TKE minus the sum B + S + T + P. It should be noted, however, that the functional form of turbulent dissipation is related to the deformation of the turbulent wind field and hence is inversely proportional to the length scale of the turbulent motions.

Figure 17 shows the vertical structure of the terms B, S, T, and P for FD5 and VD6 calculated over the period of growth of the CBL. All terms are normalized by W^{*3}/z_{top}. The relative trends and values of the terms compares very well with LES, convection tanks, and terrestrial field observations for strongly buoyantly driven turbulence (free convection), which can be seen by comparing Figure 16 with (e.g.) Figure 5 from Moeng and Wyngaard (1989) and Figure 11 from Moeng and Sullivan (1994). Specifically, Figure 17 shows that TKE in the lower CBL is generated by a combination of buoyancy generation (B) and the pressure correlation term (P), with the turbulent transport term (T) acting to reduce the TKE (i.e., by upward transport of the TKE). In the upper half of the CBL (i.e., for $z/z_{top} > 0.5$), B continues to decrease and becomes negative near the CBL top. Throughout the majority of the CBL, the T and P terms are anticorrelated, with the zero crossing of both occurring within the altitude range from $z/z_{top} = 0.5$–0.6. Thus, the vertical variation of TKE shows a significant net source of TKE in the lower CBL both from B and P, a net upward vertical transport of TKE by eddy motions (T), and finally a net sink of TKE in the upper CBL due to P as eddies are damped through interaction with the overlaying statically stable free atmosphere. Figure 17 shows that both the fixed and variable dust simulations are in the limit regime of free convection regime during the daytime (output were averaged from 9 to 16 LT), since the shear term (S) is negligible compared to the other terms. It also shows that the TKE vertical budgets, in both cases on Mars, have no major differences from those observed and modeled for the Earth during free convection (Moeng & Sullivan, 1994; Moeng & Wyngaard, 1989).

The value of TKE as a function of depth in the CBL is shown for both FD5 and VD6 at 13.5 LT in Figure 18a. In both cases, the TKE is nearly constant with height up to about $z/z_{top} = 0.8$ (due to the efficiency of turbulent mixing, term T, Figure 17), above which it decreases rapidly (due to the damping influence of the P term, Figure 17). However, Figure 18a shows that the absolute value of the TKE is much larger in the variable dust, VD6 case, with a peak value of about 16 m^2/s^2, while the fixed dust, FD5, exhibits a peak value nearer 11 m^2/s^2. There is thus about 45% more TKE within the VD6 CBL, and the factor is even higher when the influence of the higher CBL top in VD6 is also considered (i.e., when the TTKE in J/m^2 is considered rather than intensive TKE in $J/kg = m^2/s^2$). This confirms the analysis from Sections 5.2–5.4 that showed that more total energy is introduced into CBL motions when the dust distribution is inhomogeneous, even while the total dust optical depth remains similar.

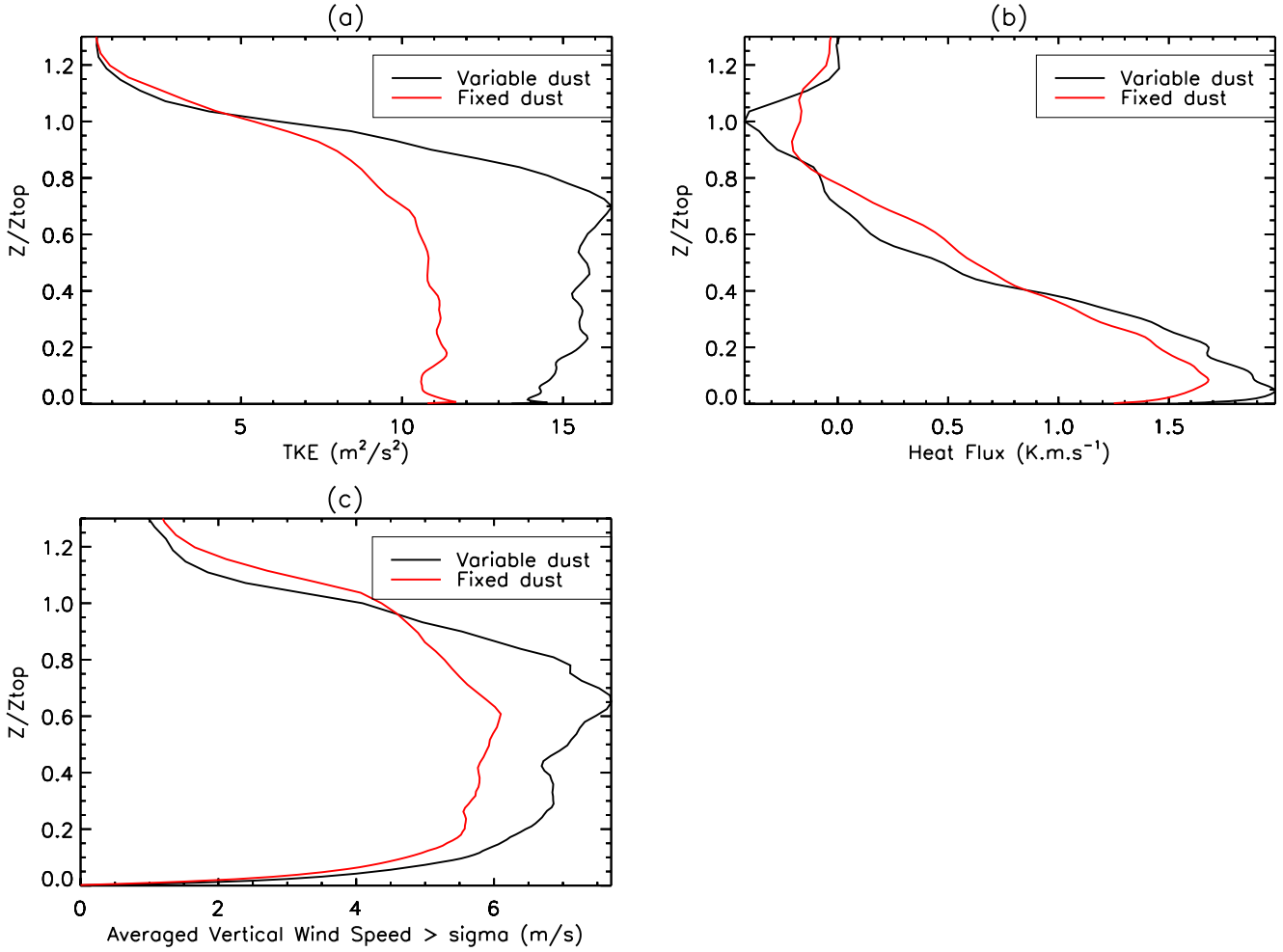

Figure 18. Variations of horizontally averaged (a) Turbulence kinetic energy (m^2/s^2), (b) Vertical eddy heat flux (Km/s), (c) Averaged vertical wind speed in the updraft (m/s) with altitude at local time 13.5 LT for fixed (red line) and variable (black line) dust cases. Updrafts are defined as locations where the vertical wind speed exceeds one standard deviation (or "sigma" as noted on the label to panel c).

Figure 18b shows the vertical heat flux for both FD5 and VD6 at 13.5 LT. While VD6 has a larger maximum to minimum range of heat flux (a change of 2.4 vs. 1.2 Km/s) the depth of the CBL is also significantly deeper for VD6 such that the dynamical heating rate (due to the vertical flux divergence in K/s) is much more similar in the two cases. It should be noted that because the VD6 CBL contains more total mass than the FD5 CBL, the total dynamical cooling rate in terms of energy is larger for VD6. Thus, the more vigorous VD6 CBL turbulence (in terms of TKE) indeed yields a more effective CBL dynamical cooling (in terms of energy per unit column of atmosphere per unit time). The relative vigor of the VD6 CBL versus that of FD5 is also illustrated in Figure 18c, which shows the average updraft speeds in VD6 are as much as 27% larger than in FD5.

The individual terms of the TKE budget is shown in Figure 19, which is analogous to Figure 17 except in Figure 19 only output from 13.5 LT is shown, and the components are rescaled in their own panels for clarity. As in Figure 17, we see that the buoyant production (B), pressure correlation (P), and the turbulent transport (T) are comparable in magnitude, while the shear or mechanical production (S) term is always negligible and thus at 13.5 LT both cases are in the free convective regime. Figure 18a shows that for VD6 the buoyant production of TKE is much larger than that in FD5 in the lower half of the CBL. The difference between the two cases is very similar to the difference in the vertical eddy heat flux (Figure 18b). This is not surprising as the buoyant production can be obtained from the vertical eddy heat flux by multiplying by $g/\langle\theta\rangle$, and where $\langle\theta\rangle$ (the lateral domain average potential temperature) differs by less than 2% between the

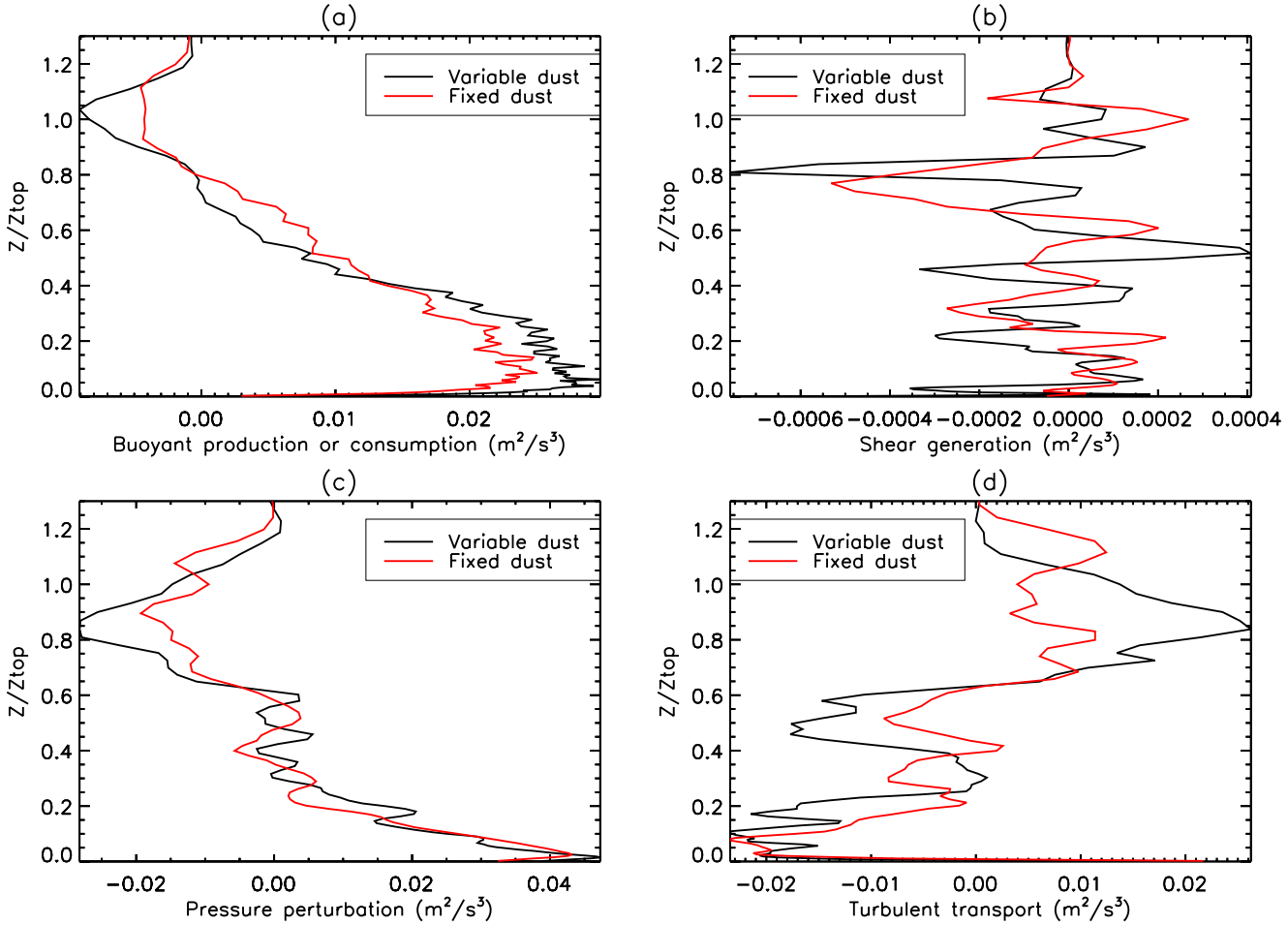

Figure 19. Same as Figure 18 but for the four turbulence kinetic energy budget terms.

two cases. Therefore, the difference in the CBL energy budget between the variable and the fixed dust cases is mainly driven by the difference in the vertical eddy heat flux $\langle w'\theta' \rangle$, which provides the quantification of the extra buoyancy introduced by the inhomogeneity of dust when it is allowed to be lifted and self-concentrates into the upwelling plumes. The $\langle w'\theta' \rangle$ is increased in the variable dust case because of the simultaneous enhancement of potential temperature θ' due to the extra visible heating by airborne dust concentrated into the upwelling plumes, and the enhancement of the upwelling wind speed, w', of these plumes due to their increased buoyancy.

6. Discussion

6.1. Lateral Dust Inhomogeneity and the Boosting of the Height of Dust Lifting

The most dramatic signature in the VD cases presented in this study is the strong growth of CBL depth with increasing optical depth and DII (Figure 2). The increase occurs due to the visible radiative heating of dust concentrated into the upwelling sheets and plumes of CBL Bénard-like open cellular convection. These results suggest a significant difference in the behavior of the CBL depth, and specifically the vertical extent of dust mixing when dust is being actively lifted. When dust is being lifted within the "feeding zone" of a CBL Bénard cell (defining a lateral scale of a few kilometers to at most 40 km), the cell will take on the character of the VD cases in this study, where there is a strong positive feedback between dust lifting (increasing dust optical depth and DII) and the depth of vertical mixing of the dust. Conversely, when there is no active dust lifting within a cell, an increase of dust optical depth (due to lateral advection of dust) tends to decrease the CBL depth and hence the depth of dust mixing. Even for moderate optical depths and the same average

optical depth over the cell, the difference in the mixing depth between active lifting and no active lifting can be several kilometers.

In reality, the difference is likely to be even larger. As the upwelling plumes ascend, the structure of the vertical motion field becomes increasingly dominated by the strongest plumes, usually those plumes originating from near surface "triple junctions" where three cellular walls meet. As a result of the concentration of the upwelling into focused plumes, the plumes generally ascend significantly higher even than the average CBL top. For example, at 13.5 LT in VD6, the CBL top is diagnosed to be at 6.4 km altitude, while the deepest plumes have injected dust almost up to 8 km altitude (or about 1.6 km or 25% overshoot, see Figures 6c and 16a). The FD case at the same optical depth and local time has a CBL top at 4.9 km, thus the plume overshoot is about 65% (or 3.1 km) higher than the CBL top with no dust lifting.

These simulations suggest that global models using radiatively and dynamically interactive dust that allow inline PBL schemes to vertically mix the dust are likely substantially underestimating the vertical depth to which surface-lofted dust can be spread (e.g., Newman & Richardson, 2015). Indeed, models using such an approach generally yield vertical thermal profiles that are excessively stable and vertical profiles of dust that exhibit too great of a decline with height compared with observations (e.g., Lee et al., 2011). The observed transport of dust to high altitudes also includes features with maxima of dust mass mixing ratio away from the surface (Heavens et al., 2011). The difference of maximum dust penetration heights between active dust lifting and non-active lifting area provides a mechanism for initiating layers of dust because strong CBL above active areas emplace dust to levels that cannot then be mixed down in later sols when the lifting has stopped, or when the dust has advected into surrounding non-active regions. While the typical CBL depths are not high enough in themselves to explain the observed altitude range of dust layers, when combined with variations in topography (Rafkin et al., 2002) and with the "solar escalator" mechanism (Daerden et al., 2015) the proposed mechanism for the creation of layers may be important (though proposed rocket dust storms, where dust clouds may ascend in altitude as coherent mesoscale dynamical structures, may also play a similar or more important role Spiga et al., 2013; Wang et al., 2018).

6.2. The Sensitivity of CBL Depth and Surface Frictional Velocity to DII

The competing factors damping and augmenting CBL turbulence as dust loading varies in the FD and VD simulations are (a) the shading of the surface by increasing dust optical depth causing the surface-atmosphere temperature to decline, and (b) lateral differences in the heating of the surface and atmosphere as dust is concentrated into CBL plumes. In the absence of the latter, as is the case in the FD simulations, an increase of optical depth leads to a rapid decrease in CBL depth and the energy contained in CBL turbulence. However, this study has shown that inhomogeneity of dust causes both a significant increase in the depth of CBL mixing and in the vigor of CBL mixing.

It will be important in future work to further explore how the CBL responds to a range of DII and optical depth combinations, which have not been exhaustively explored in this study due to time and page length limitations. However, an initial pilot exploration of the sensitivity of CBL depth and surface frictional velocity is shown in Figure 20. For this pilot, we performed dozens of LES cases with different initial dust optical depths and lifting rate parameters. Even though only a limit range of modest DII values were examined, the CBL depth shows a very clear dependence on DII. Significantly, the importance of the DII increases as the dust optical depth increases, with the CBL depth doubling for a change of DII from 0 to 0.15 when the total domain average visible dust optical depth is 0.5. This suggests that the inhomogeneity feedback becomes increasingly potent as the dust optical depth increases, which has a compounding effect on the feedback. The compounding effect in these simulations occurs after the DII exceeds about 0.125, after which increasing dust optical depth and increasing DII each separately lead to increasing CBL depth.

For the range of dust optical depth and DII considered in this pilot study, the feedback of dust optical depth and DII on frictional velocity (and hence surface wind shear stress) is more muted (Figures 20b–20d). For DII = 0, the frictional velocity dependence on optical depth is intuitive, with the value decreasing with increasing optical depth. However, for all but the smallest optical depths, there is a slight trend of mean, one-sigma, and maximum frictional velocity increasing with DII. Above DII = 0.15, there is also the hint of a reversal of the dependence of maximum frictional velocity upon total dust optical depth, such that

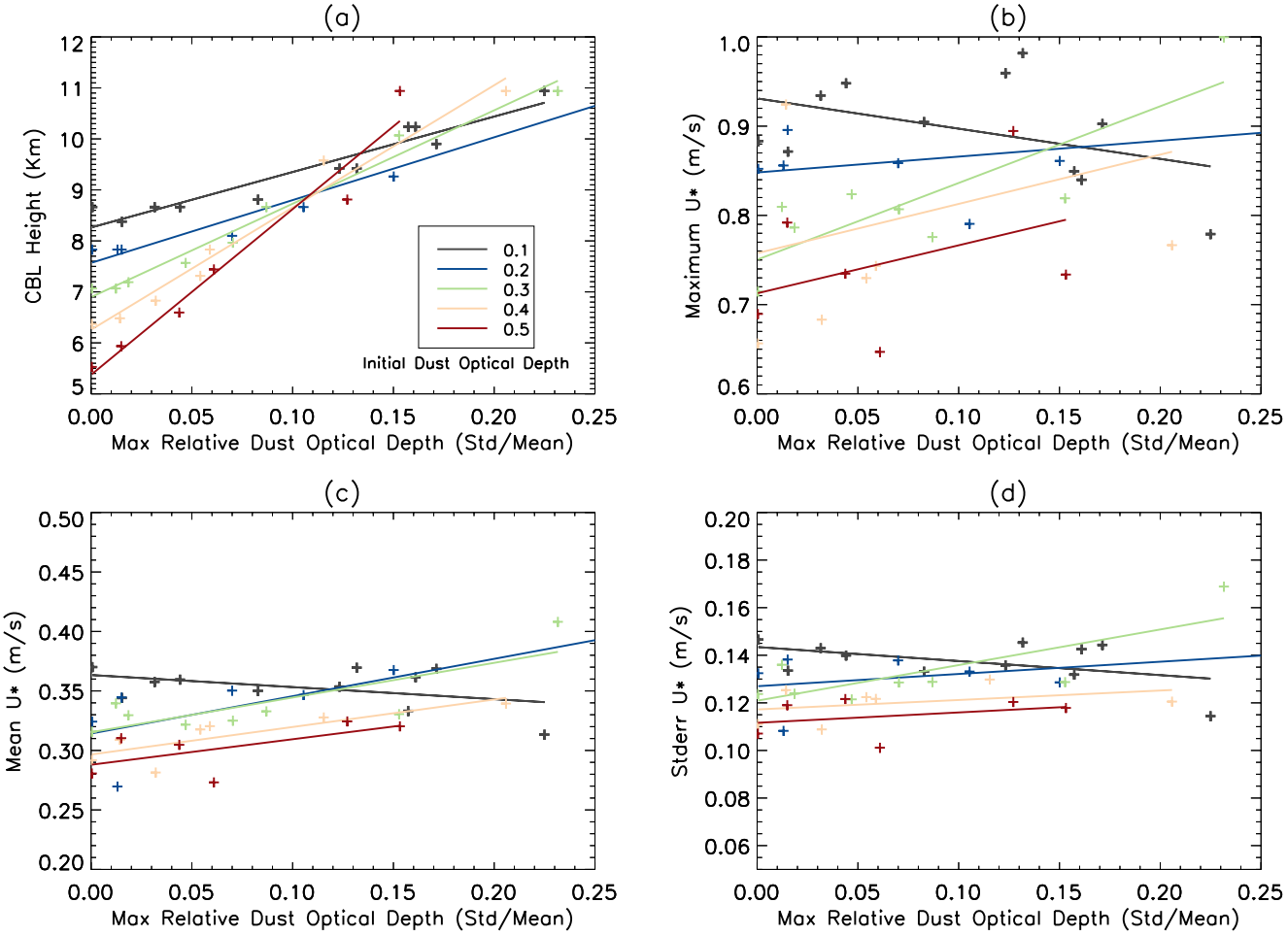

Figure 20. Variation of (a) convective boundary layer depths (km) at ~17 LT, and (b) maximum, (c) mean, (d) standard error of the friction velocity u* at 13–15 LT, with maximum dust inhomogeneity index values for different initial dust optical depth.

increasing optical depth might begin to yield increased wind stresses. If real, this would be important as it would suggest that above certain thresholds of optical depth and DII, there might exist a positive feedback for wind stress dust lifting that is, intrinsic to the CBL. There is clearly insufficient signal-to-noise in the pilot study output to address this suggestion, and thus here we simply note a tantalizing question that needs to be addressed in a future work.

6.3. Uncertainties Associated With the Vertical Distribution of Dust and Time Evolution

Controlling for differences in the dust vertical structure and hence in heating above the CBL is a tradeoff from the perspectives of both model implementation and the underlying physics we are trying to simulate. From the perspective of model implementation, we had to choose between comparing similar total optical depths versus comparing similar free atmosphere visible dust heating. Because the variable dust cases unavoidably involve active dust lifting from the surface, their dust distribution will always tend to be centered lower in the atmosphere than a "steady state" fixed dust case. If the experiments were to be designed in order to obtain similar heating in the free atmosphere, the dust column optical depth in a variable dust case would thus need to be larger. In our comparisons, we have decided to emphasize similar optical depths as these then correspond to similar dust shading of the surface and to similar total visible dust heating of the atmosphere.

Moreover, because dust lifting is always from the surface, it is a real physical effect that the vertical dust distribution will always be more steeply concentrated at the surface in this case rather than in an atmosphere

where no lifting occurs. When no lifting is occurring, dust will be well mixed to the daytime maximum CBL top or will even increase in layers well above the area average CBL top (Heavens et al., 2011). Therefore, the unavoidable differences in the vertical gradients of visible dust heating evident in Figures 9a and 9b are an additional way in which the processes responsible for laterally inhomogeneous dust (i.e., dust lifting and entrainment in CBL plumes) augment the strength of the CBL compared to a fixed dust case. The more bottom-heavy dust distribution in a CBL where dust is being actively lifted generates more heating both in the visible and the infrared in the lower portion of the CBL and less heating in the free atmosphere into which the CBL grows, and thus increases buoyancy relative to the fixed dust case.

6.4. Parameterization of PBL Properties for GCM and Mesoscale Models

Most of our focus in the discussion section so far has been on how inhomogeneous dust impacts the dust vertical distribution and dust lifting. However, these facets of the discussion rely on the primary result of this study that the CBL dynamics are fundamentally modified by the dust inhomogeneity radiative effects compared to cases with uniform dust. The inhomogeneity is only important in areas of active dust lifting. While the area of the planet involved in active dust lifting at any given time associated with local dust storms and dust devil activity is likely to be small (e.g., Cantor et al., 2001; Fisher et al., 2005), it is possible that the significant differences in the CBL in these locations might influence globally integrated heat, momentum, and water exchange with the atmosphere. Current PBL parameterizations in models that do not resolve the PBL do not include any representation of the effects of dust inhomogeneity on the CBL. Indeed, the influence of dust inhomogeneity upon predicted CBL depths suggests that there is likely need to revisit modeling of radio occultation-derived CBL depth (Hinson et al., 2008; Spiga et al., 2010). Specifically, for the Hinson/Spiga case i, when using uniform dust both the present model and the Spiga et al. (2010) LES underpredicted the observationally estimated CBL depth by about 2.5 km (see Table 2). However, for different combinations of dust loading and DII, the MarsWRF LES can plausibly match the observationally estimated CBL depth (Figures 2a and 20a). A more focused study looking specifically at the plausible optical depths and DII for each radio occultation profile would be needed to fully explore the DII effect in resolving discrepancies between extant LES predictions and radio occultation retrievals.

The LES output from this study will provide a resource from which a PBL parameterization that includes dust inhomogeneity could be developed. An attractive method of parameterization is the Eddy Diffusion/Mass Flux (EDMF) approach (Siebesma & Teixeira, 2000; Siebesma et al., 2007) in which the PBL motions are described in terms of the simultaneous effects of a local background eddy diffusion (ED) and a nonlocal mixing by deep plumes using a mass flux (MF) representation. The parameterizations are built by constraining the relationship between the mass and heat tendencies output from the MF scheme and the input resolved thermal and wind structure using the plume behaviors from LES (e.g., Witek et al., 2011). For the dry PBL, this approach has already been applied to Mars by Colaïtis et al. (2013). However, EDMF approaches are amenable to treating both “dry” and “moist” convection, where “dry” refers to the case of free convection resulting purely from heating of the atmospheric column at its base, and “moist” refers to the contribution of heat within the interior of the fluid in upwelling plumes and where the heating rate depends upon the vigor of that upwelling (e.g., Han & Bretherton, 2019). Moist convection is the process behind convective cloud formation, with the additional heating resulting from latent heating as atmospheric gases condense—on Earth this is water vapor, but it can also be methane (on Titan and the gas giant planets) and carbon dioxide (in the Martian atmosphere), *etc.*

However, the DII effect presented in this study demonstrates an additional form of interior heating that, unlike moist convection, is not due to latent heating but instead is due to visible radiative heating of suspended dust. In order to capture the combined effect of “dry” and “dusty” forcing upon convection, an MF scheme will need to be developed from dusty LES, such as that presented in this study, to be able to link large-scale forcing variables in order to properly predict the depth and vigor of CBL mixing when dust lifting is ongoing. Similarly, the close and bidirectional relationship between DII and dust lifting suggests that current separate dust lifting and PBL schemes in Mars GCM and mesoscale models would be improved with a unified model of PBL dynamics, mixing, and surface dust lifting.

6.5. Dust Devil Dust Lifting

While LES is capable of modeling convective vortices and dust devils, the model mesh chosen for the bulk of this project would not capture most of the dust devil spectrum (e.g., from the table of large dust devils in Amazonis measured from high resolution images by Fisher et al., 2005, only the very widest—at 459 m—could even barely be resolved with our 100 m mesh spacing), and orbital imaging itself cannot resolve the smaller dust devils regularly observed by surface missions. As such, there is a need to examine dust devil statistics within the context of a LES with radiatively and dynamically interactive dust in the future. However, we can examine what the implications of the inhomogeneous dust in the present CBL simulations using the thermodynamic efficiency theory of Renno et al. (1998).

Renno et al. (1998) provided a means of quantifying the level of dust devil activity based on the fact that "the flux of mechanical energy made available by the convective heat engine is equal to the flux of energy mechanically dissipated by friction." The Renno et al. (1998) dust devil activity (the energy available for convective vortices, Λ) is found to be:

$$\Lambda = \left(1 - b\right) F_{si} \tag{8}$$

and:

$$b \equiv \frac{P_s^{\kappa+1} - P_{\text{top}}^{\kappa+1}}{\left(P_s - P_{\text{top}}\right)\left(\kappa + 1\right) P_s^{\kappa}} \tag{9}$$

where F_{si} is the heat input to the CBL at the base, P_s is the surface pressure, P_{top} is the CBL top pressure, and κ is the ratio of the specific gas constant and the specific heat at constant pressure. F_{si} is the properly taken to be the sum of the sensible heat flux from the surface and the thermal infrared radiative heat flux between the surface and the lowest portion of the atmosphere (from Figures 9c and 9d, we take this depth to be 1 km).

Figure 21 shows the sensible and 1-km infrared heating terms (Figures 21a and 21b, respectively), the parameter (1-b) (Figure 21c), and the dust devil activity, Λ (Figure 21d), for the FD cases. These results show the roughly comparable contributions of the sensible and radiative heat flux to the heating of the bottom of the CBL, with the sensible heating peaking slightly later in local time than the radiative heating, and with the former also moving to progressively earlier local times as the optical depth increases. Both the sensible and radiative heating decreases with increasing optical depth, but the sensible heat decreases far more significantly, consistent with the dramatic decrease in CBL convection (c.f., Figure 2). The (1-b) parameter (Figure 21c) depends significantly upon the CBL depth, and thus it also decreases with optical depth increase and should be compared with Figure 2b. Also consistent with the CBL depth, (1-b) attains its greatest value in the late afternoon. As the linear product of (1-b) and the sum of the sensible and radiative heating, the dust devil activity, Λ, peaks in the early afternoon and then falls to near zero by the late afternoon (Figure 21d). Peak Λ decreases by about a factor of 2 as the dust optical depth increases from 0 to 0.5. Thus, there is a very strong negative feedback between increases in optical depth and Λ in the FD cases. This is reflected in the negative feedback for dust devil dust lifting reported in GCM simulations (e.g., Basu et al., 2004; Kahre et al., 2017; Newman & Richardson, 2015; Newman et al., 2002).

Figure 22 shows the same parameters as Figure 21, but instead for the VD cases. For these cases, the relative insensitivity of the result to dust optical depth is noticeable, even though the optical depth differences between the cases is large by 17 LT (see Figure 4). The reasons for the reduced sensitivity of the surface-atmosphere temperature contrast to changing optical depth when dust is inhomogeneous are mentioned in Section 5 (the sensible and radiative heat fluxes are largely controlled by the surface-atmosphere temperature contrast). The control of the (1-b) parameter by the CBL depth is illustrated in Figures 22c, which shows an opposite trend with increasing dust optical depth compared to the FD cases (Figure 21c). Specifically (1-b) now increases significantly as the optical depth is increased in the mid- and late afternoon. Indeed, the (1-b) parameter shows a larger sensitivity to changing optical depths than the lower CBL heating (Figures 22a and 22b), and thus the output suggest a slight positive feedback between increasing optical depth and increasing peak dust devil activity, Λ, for the VD cases (Figure 22d). If this positive feedback does exist—or even the relative lack of sensitivity of Λ to total dust optical depth compared to the traditional strong negative feedback exhibited in Figure 21d for the FD cases—this suggests that there might be very

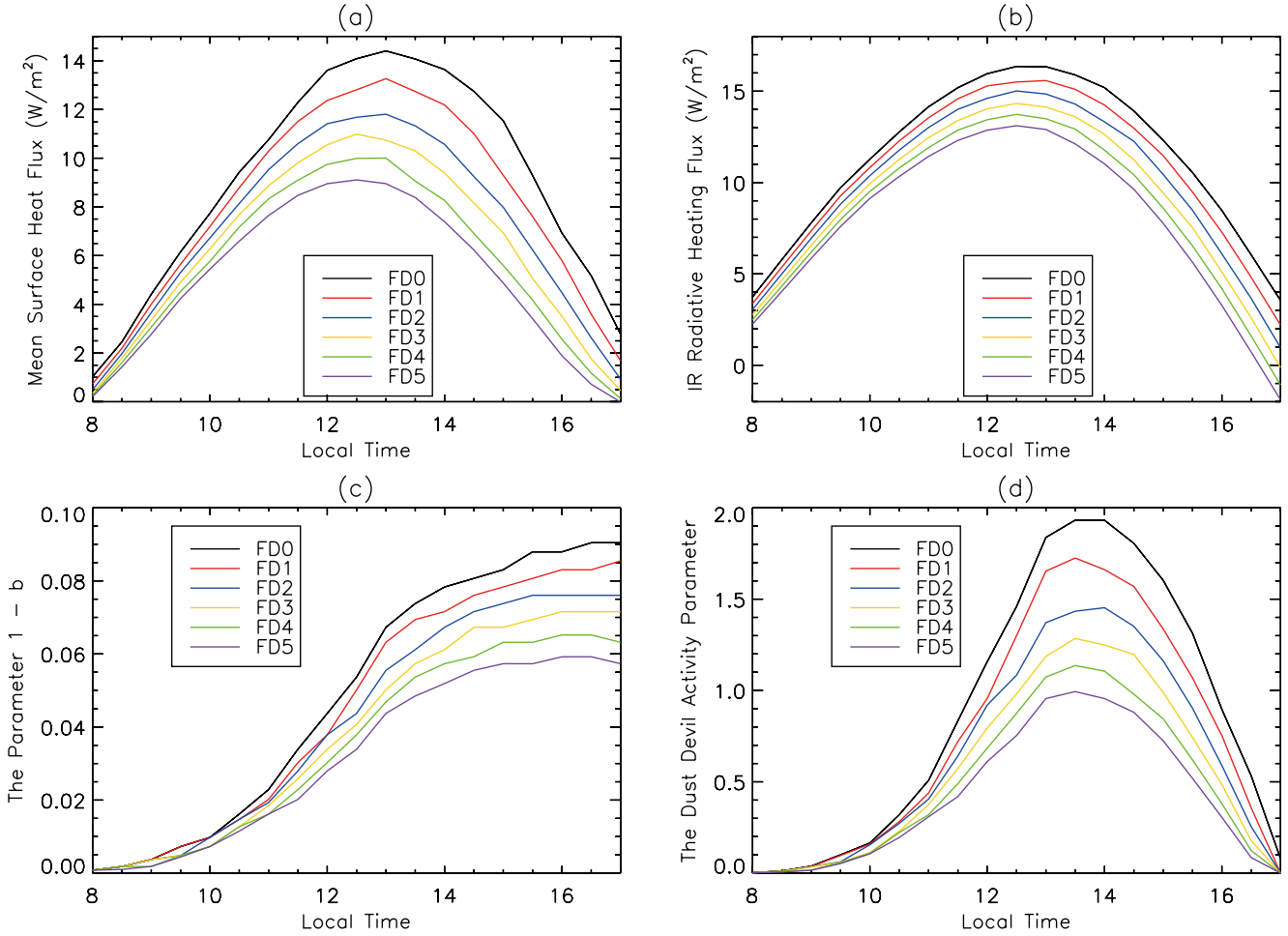

Figure 21. The evolution of (a) Sensible heat flux (W/m^2), (b) the infrared heating of the lowest 1 km of the convective boundary layer (CBL) (W/m^2), (c) the thermodynamic efficiency parameter for dust devils following Renno et al. (1998), and (d) the dust devil activity factor generated from the product (Newman et al., 2002) of the thermodynamic efficiency parameter and the sum of the sensible and radiative heating of the lower CBL (the sum of the quantities in panels a and b). The cases shown are from the fixed dust (FD) ensemble.

significant implications for GCM simulations of the global dust cycle, in which dust devils are thought to play a substantial role in maintaining the background haze of dust and in which the strong negative feedback of optical depth upon dust devil lifting is a feature of existing dust devil lifting parameterization (Basu et al., 2004; Kahre et al., 2017; Newman et al., 2002).

The LES cases shown in Figure 22 was not optimized to study dust devil activity. The noise apparent in the Figure, especially as regarding the weak positive feedback of dust optical depth upon Λ, could be rectified by generating much more frequent output from the LES cases thereby generating more data points at comparable local times (in this initial study, we had to balance the number of cases run against the volume of output needed for storage and processing). However, it would probably be more useful to undertake specific LES experiments designed to explicitly resolve a much larger fraction of the dust devil spectrum and to test the relationship between the simulated dust devil populations, the Λ diagnostic, and the influence of total optical depth and DII on both. Such LES experiments would need between a factor of 10 and 100 decrease in the grid spacing compared to the VD cases in this study, and thus is deferred to a subsequent study.

6.6. Reasonableness of DII Values Examined

Almost all of the VD cases conducted in this study were designed so as to obtain a range of moderate total optical depths to compare with the FD cases. These simulations yielded visible optical depths in the range

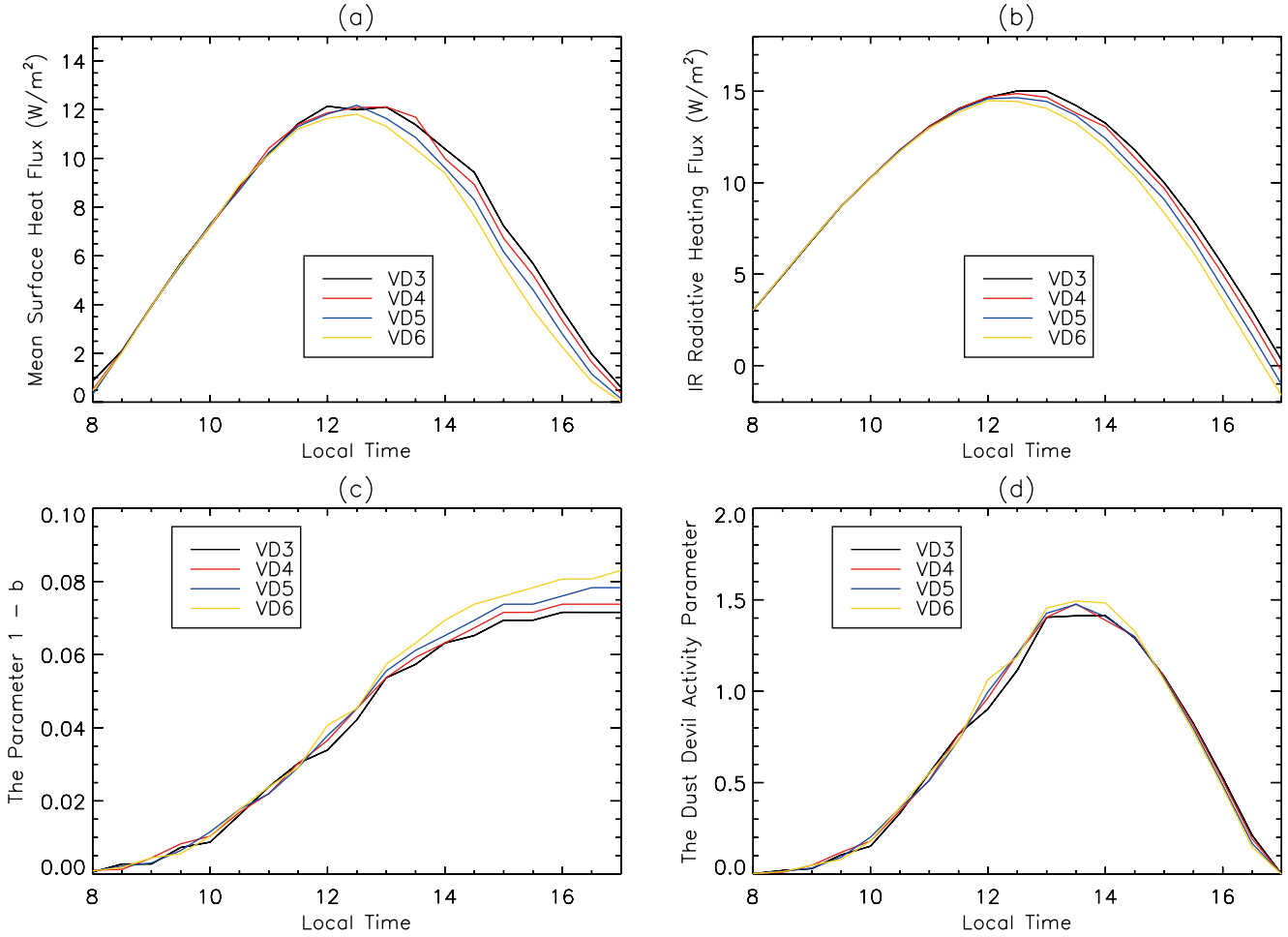

Figure 22. Same as Figure 21 but for the variable dust (VD) ensemble.

of about 0.3–0.6 over an area of about 14 km, with peaks in plumes up to about 0.8. In terms of the DII, the main ensemble of VD cases yielded a peak value of DII <0.1. In order to initially probe the effect of larger amounts of dust inhomogeneity, dust lifting was modified in simulations required to generate Figure 20 such that a maximum value of DII = 0.23 at $\tau = 0.3$ was simulated. It is thus natural to ask how representative these cases are of real dust lifting situations on Mars.

There are few observations of opacity within dust storms at resolutions close enough to LES for good comparison, but those that do exist find significant dust inhomogeneities at the low end of the mesoscale (thus at the scales of the whole extent of the LES domains considered in this study). Määttänen et al. (2009) observed a local dust storm with OMEGA that appeared to consist of at least "rounded plumes" of dust with $\tau > 6$ that were 5–10 km in diameter, and that alternated with areas of much clearer air of similar scale. This yields an equivalent DII > 0.5. Heavens (2017) describes large local dust storms in the northern mid-latitudes in Mars Orbiter Camera (MOC) and Mars Color Imager (MARCI) images that consist of alternating bands of dustier and clear air of 15–50 km thickness with opacities ranging from 0.4 to 1.4, implying a DII of ~0.4. On somewhat shorter length scales, the dust lifting plumes capture in THEMIS visible images and shown by Inada et al. (2007) yield sharp optical depth variations on scales as a short as 650 m. While the optical depths were not retrieved from these images, the dust clouds obscure the surface below the convective roll plumes, suggesting DII values at least as large as OMEGA, MOC, and MARCI image locations. The THEMIS images also suggest that the primary mechanism causing dust inhomogeneity—namely concentration of dust into upwelling plumes and sheets—is actually at play in the real atmosphere. An example of the structure of dust lifted in convective rolls from THEMIS imagery is shown in Figure 23a. Given that

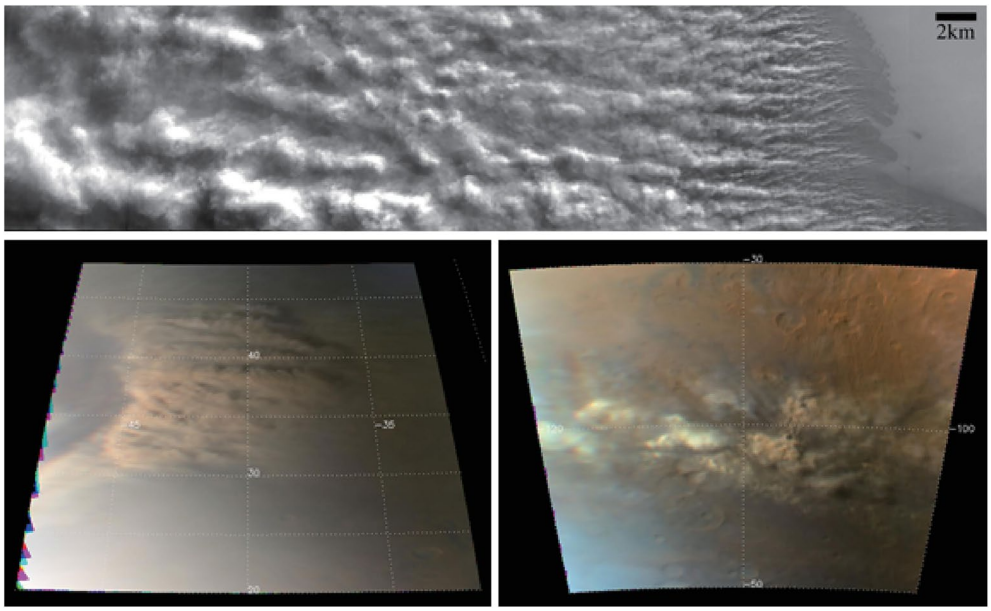

Figure 23. Images of lateral dust inhomogeneity in the Martian atmosphere on various scales. (Top) THEMIS visible image of dust lifting in the high southern latitudes. Plume structures on scales from several km down to a few 100 m are visible. THEMIS image number V00874006. (Bottom left) Color composite image derived from Mars Color Imager (MARCI) image G06_020693_2052_MA_00N029W showing dust lifting on 10–100 km scale at $Ls = 205.2$ MY = 30. (Bottom right) Color composite created from MARCI image B16_015883_0243_MA_00N109W ($Ls = 24.3$ MY = 30).

dust inhomogeneity has been observed on scales down to a few 100 m in orbital observations, it raises the question as to whether they can be detected in much weaker dust lifting environments sampled by rovers and landers. This would be an important question likely answerable with image processing applied to rover and lander imaging.

The very much higher values of DII implied by the observations and for large values of optical depth suggest that the strength of positive dust feedback on the augmentation of CBL turbulence and the lifting of dust may be underestimated in this study, although it is possible that at very large dust optical depths the shadowing of the surface—or indeed, the self-shadowing of much of the thermals—may come to dominate over the augmenting differential heating. This is an interesting question that requires further study in more extreme dust injection rate LES cases designed to simulate very small-scale dust storms and dust lifting plumes, such as those shown in Figure 23a. However, the observations also suggest that the simulations and the DII values and results of this study are probably not excessive for moderate dust lifting, such as might be associated with modest dust devil activity and/or putative wind gust dust lifting that does not lead to distinct local storms identifiable in imagery.

6.7. The Dust Opacity/Dust Lifting Feedback on Larger Scales

This study has examined dust lifting and dust concentration in isolation at the microscale (i.e., on scales equal to and shorter than that of the largest CBL convection cells). However, spacecraft imagery provides ample evidence of various types of "textures" on the topside of dust storms at scales that extend continuously from hundreds of meters to hundreds of kilometers (Figure 23). Texture elements within dust storms are common in MOC and MARCI wide-angle camera images (a few km/pix) (Guzewich et al., 2017; Kulowski et al., 2017; Toigo et al., 2018) and are also corroborated by opportunistic narrow-angle camera images (down to a few m/pix) (Inada et al., 2007; Määttänen et al., 2009).

These observed textures at micro- and mesoscales are potentially indicative of the dynamics operating within dust storms from the very smallest of scales. The LES examined in this work suggest that even at relatively low optical depths and relatively modest DII, positive feedback exists between optical depth and vertical dust mixing and potentially dust lifting from the surface. Ultimately, larger scale storm systems are initially

composed of individual PBL plumes, cells, and rolls, as visually exemplified in Figure 23a, where the growth from small scale plumes to larger consolidated dust clouds can be seen from image right to image left (which is almost certainly the downstream wind direction). Thus, an important question for future work is how the microscale feedbacks demonstrated here might influence the mesoscale and larger dust clouds observed in the atmosphere. Are such feedbacks important at the tops and/or at the periphery of local storm systems and are they involved in storm growth? And to what degree are the microscale mechanisms of storm growth responsible for the growth of dust up to the extent where distinct mesoscale modes of growth become important? Are there mechanisms of storm expansion that involve individual dusty cells/plumes causing the excitation of neighboring cells through the lateral leakage of momentum and/or dust? The existence of some feedback at microscales demonstrated in this study suggests that further LES experiments with larger domains that cross the micro/mesoscale boundary are warranted.

7. Summary

In this study, we employed a validated version of the MarsWRF in LES mode to examine the differences in CBL dynamics between: (a) idealized uniform distributions of radiatively active dust (the "fixed dust" or FD cases in this study) and (b) more realistic dust distributions that would occur when dust lifting is ongoing in which the dust is self-consistently concentrated into upwelling plumes (the "variable dust" or VD cases in this study). The FD cases are also likely to represent reality in cases where no active dust lifting is occurring, and the dust distribution has been largely homogenized by CBL mixing over several prior sols if raised locally, and/or imported via lateral transport.

The CBL behavior for the FD cases was found to agree with expectations based upon the effect of atmospheric dust in shading the surface. With increasing optical depth, the surface-atmosphere temperature decreases and hence the heat flux (both sensible and radiative) from the surface into the lower portion of the CBL also decreases. This causes a decrease in the energy injected into the CBL (a reduction in the TKE), a reduction in both the Deardorff (convection) velocity scale and maximum vertical plume speeds, a reduction of the surface layer wind stresses associated with the turbulent motions, and a reduction in the depth of the CBL. This influence of dust optical depth upon the CBL dynamics has previously been widely noted, and if it represented the whole story as applied to dust lifting would produce a negative feedback (e.g., Kahre et al., 2006; Newman et al., 2002). Specifically, increased dust optical depth would decrease CBL wind stresses (reducing lifting due to gusts in the CBL) and would also decrease the energy input to and thermodynamic efficiency (related to CBL depth) of the convective vortices that form dust devils (Renno et al., 1998). In both cases, dust lifting potential would decrease as the optical depth increases, and the depth of the dust lifting would become shallower as dust optical depth increases.

With fully interactive dust (the VD cases) the CBL exhibits quite difference behavior relative to the FD cases. Comparing FD and VD cases at similar total optical depths in the mid-afternoon, the differences in the dust distribution are twofold: (a) there are significant lateral differences in dust optical depth, which can be characterized with a Dust Inhomogeneity Index, $\mathrm{DII} = \sigma_\tau/\tau_{\mathrm{avg}}$ (see also Equation 5), where σ_τ is the lateral standard variation of the dust opacity and τ_{avg} is the lateral average, and (b) there are differences in the vertical dust distribution due to the process of active dust lifting tending to have more of the dust near the surface in the VD cases vs. FD cases for the same total optical depth. Both aspects of the dust distribution influence the CBL dynamics when comparing FD and VD cases. Specifically, for the same mid-afternoon optical depth, the VD cases exhibit larger surface-atmosphere temperature contrasts, larger heat fluxes into the CBL, larger TKE in the CBL, larger Deardorff and updraft plume speeds, larger near-surface wind stresses, and deeper CBL. The mechanisms of augmentation of the VD cases are found to be threefold: (a) the laterally inhomogeneous dust distribution causes visible radiative heating to be preferentially concentrated within the upwelling plumes, injecting additional buoyancy and hence TKE directly into CBL convection, (b) relatively smaller total dust optical depth within CBL downwelling regions allows higher surface temperatures, higher surface-atmosphere temperature contrasts, and hence greater surface-atmosphere exchange of heat, and (c) the relatively clearer atmosphere above the CBL top in the VD versus the FD cases means slightly cooler free atmospheric temperatures and hence greater ease of vertical penetration of the CBL as it grows.

The impact of dust lifting rates on the DII and on the CBL dynamics were also examined within the VD ensemble of runs. As the lifting rate—and hence afternoon optical depths—increase, the surface temperature does decrease, but to a much lesser degree than for comparable changes of opacity between FD runs. This reduced efficacy of shading appears to be due to the concentration of the dust optical depth into the plumes, leaving relatively clear air over much of the surface. With the surface-atmosphere temperature contrast response to increased domain-average opacity very much muted compared to similar changes within the FD ensemble, the surface-atmosphere heat flux is little changed and hence the expected CBL vigor, in terms of the modified Deardorff vertical velocity is also muted. Indeed, until the later afternoon, the Deardorff vertical velocity, the vertical maximum plume speeds, the surface frictional velocities, and the TKE per unit mass of air are insensitive to the optical depth, such that there appears to be no negative feedback of optical depth on the CBL vigor. However, there is a notable increase in the CBL depth with the rate of dust injection and/or total optical depth. If one were to use the Renno et al. (1998) heat engine scaling to assess the activity of dust devil dust lifting (e.g., Newman et al., 2002), the insensitivity of the surface-atmosphere heat flux to increased optical depth and the significant positive feedback of CBL depth with optical depth would suggests that there will be in fact be a positive feedback for dust devil lifting when the dust is not uniformly distrib-

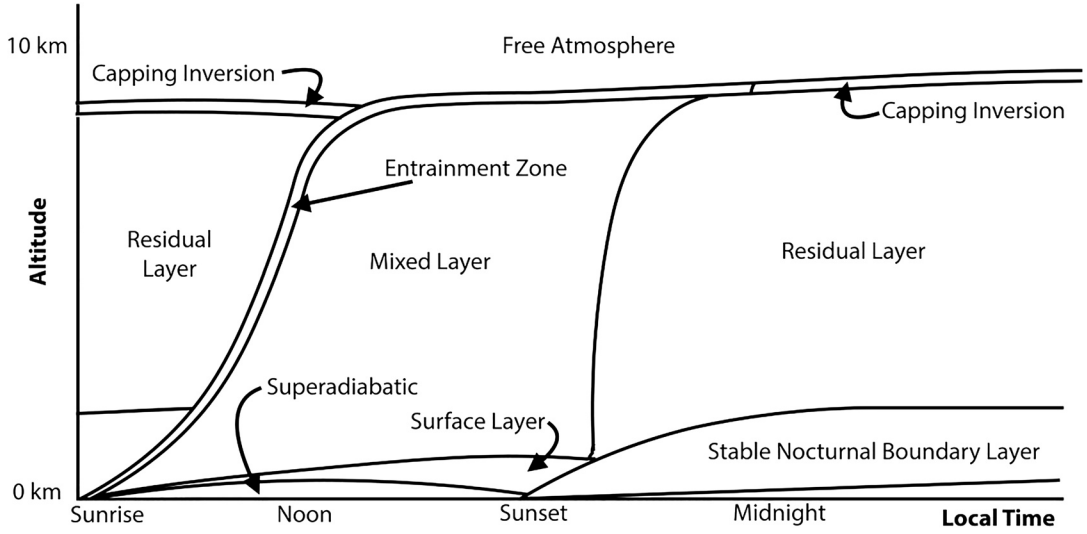

Figure A1. Cartoon of the conceptual structure of the planetary boundary layer (PBL) as used in this study. See text for details.

uted. The increased CBL depth also suggests that even for moderate lifting rates and moderate DII values, dust is lifted several kilometers deeper into the atmosphere than predicted by models using uniform dust.

Appendix A: Conceptual Structure of the Martian Planetary Boundary Layer (PBL)

This study uses common terrestrial terminology regarding the diurnally evolving planetary boundary layer (e.g., Spiridonov & Ćurić, 2021; Stull, 1988). As an aid for the reader, Figure A1 provides a summary cartoon of the layers referred to in this study and places them in a potentially more familiar terrestrial context. Starting at sunrise, and momentarily ignoring the layers substantially above the surface, the heating of the ground by the sun causes an unstable near surface thermal profile, generating thermally unstable, "free" convection that begins to mix upward into the overlaying air, entraining this overlaying air into a growing boundary layer. Due to the relative inefficiency of thermal convection relative to the terrestrial case, near surface radiative heat exchange is much more important than on the Earth, and there develops a significant superadiabatic layer upward from the surface and that can ultimately extend a few hundred meters from the surface. This superadiabatic layer is part of the deeper surface layer that is, dominated by interactions with the surface. Above the surface layer, a well-mixed layer develops that is, capped by the entrainment

zone that continues to ascend until the early afternoon. This daytime, free-convective PBL, from the surface to the top of the entrainment zone is referred to as the convective boundary layer (CBL) and is the focus of the present study. The CBL collapses around sunset, but the atmosphere well mixed by the daytime CBL often remains as a residual layer during the night. The residual layer is no longer convectively coupled to the surface but may retain a distinct thermal structure as compared with the free atmosphere, which was never entrained in the CBL. Overnight, the near surface thermal structure is inverted with respect to that during the daytime, with minimum temperatures right at the ground. The evolution of the residual layer over night depends strongly upon lateral advection and nighttime radiative heating/cooling. When the CBL begins anew the next day, it grows upward into the residual layer left over—and potentially modified—from the prior day.

Appendix B: The Sub Grid Scale/Sub Filter Scale Parameterization

A significant difference between the microscale LES and the meso- and synoptic-scale application of Mars-WRF is in the treatment of sub grid scale (SGS) mixing and dissipation. In meso-/synoptic-scale application, the SGS parameterization provides a representation of the mixing of heat, momentum, and tracers due to all microscale motions (i.e., the full spectrum of PBL eddies) from the largest Bénard cell down to dissipation length scales. The numerical mesh for meso/synoptic scale modeling is always at least an order of magnitude more tightly spaced vertically than it is horizontally (i.e., $\Delta x > 10\Delta z$). The reason for this is that atmospheric motions are approximately hydrostatic at synoptic- and the larger mesoscales, with the characteristic horizontal wavelength being much longer than the vertical wavelength. Thus, for synoptic and hydrostatic mesoscale models, a simple local model of diffusion in the horizontal is always paired with a more complex model of vertical PBL mixing that often involves nonlocal contributions. For nonhydrostatic motions that are much more important at the microscales of the CBL, the horizontal scale becomes comparable with vertical scale. Thus, for LES the model mesh is more similarly spaced (perfect isotopy is not required, but the grid spacing will generally be $\Delta x = k\Delta z$, where k is roughly $O[1]$) in the horizontal and the vertical, and unresolved mixing and dissipation is treated with three-dimensional parameterization. Since the dominant PBL eddies are resolved by design in LES, the PBL parameterization is deactivated.

The reason that any SGS parameterization is needed in LES is that while LES captures most of the microscale dynamical length scales, it is not direct numerical simulation and thus does not capture the motions all the way down to the length scales of dissipation (i.e., the Kolmogorov length scale) at about 0.1–10 mm (e.g., Stull, 1988). In practice, for reasons of computational efficiency, LES is generally implemented with a mesh spacing of roughly 1–100 m. As such, LES still requires SGS parameterization of eddy diffusion for scales between the grid scale and the dissipation scale (it should be noted that the term sub filter scale (SFS) parameterization is often more accurately used instead of SGS since representation of motions on scales below those *fully resolved* by the model is actually what is required, and that the effective numerical filter scale of the mesh is always larger than the grid scale due to numerical discretization error.)

WRF contains several different SGS parameterizations, with some significantly more complex than others. The two least complex and most widely used SGS parameterizations available within WRF are three-dimensional local eddy diffusivity models in which the diffusivity/viscosity is calculated from either (a) the resolved wind field deformation and static stability (in the "Smagorinsky scheme"), or (b) the prognostic SGS turbulence kinetic energy (TKE, in the "SGS TKE scheme"). In this study, we specifically use the SGS TKE scheme.

In this appendix, we describe the relationship between the calculation of diffusivity/viscosity in the Smagorinsky and SGS TKE schemes (Lilly, 1966; Moeng, 1984). We also provide a formulation for diagnosing the subgrid scale TKE from the Smagorinsky scheme.

Appendix B.1. Relationship Between Diffusivity/Viscosity and TKE Within the Smagorinsky and TKE SGS Parameterizations

For understanding the evolution of the PBL (and for many approaches to parameterizing PBL mixing) an understanding of the total budget of TKE is required. In LES, the total PBL TKE must be constructed as the sum of the resolved-scale TKE and the SGS parameterized TKE. In the case of the widely used "3D Smagorinsky" scheme (Smagorinsky, 1963), and unlike the SGS TKE scheme, the TKE on unresolved scales is not prognostic and must be diagnosed from the model. In the remainder of this section, we provide a discussion of what processes influence the SGS TKE budget and how the subgrid scale TKE, the 3D flow deformation, and the static stability are related; and how each relates to the viscosity/diffusivity.

The formulation of both the Smagorinsky and TKE SGS schemes is based on the assumption that subgrid scale eddies act analogously to molecular viscosity (Lilly, 1966). As such, subgrid-scale stresses can be treated as a viscous response to the deformation of the model-resolved motion. The deformation is given by the strain rate tensor calculated from the model-resolved winds (Lilly, 1966; Moeng, 1984):

$$S_{ij} = \frac{1}{2}\left(\frac{\partial u_i}{\partial x_j} + \frac{\partial u_j}{\partial x_i}\right) \tag{B1}$$

where the indices i and j refer to orthogonal coordinate directions and may have values 1, 2, or 3, with the distance in each of these directions given by x_i, and the components of the resolved wind field in each of these directions by u_i. The strain rate itself can be visualized as being composed of two parts, a component of net radial expansion or compression of the flow, and a component of volume conservative shearing of the flow. The subgrid-scale stresses, which build up within the fluid as a result of this resolved strain and act to oppose the strain, depend on the eddy viscosity of the fluid. Within a completely inviscid fluid, no stress would develop at all. In general, the eddy viscous stress (or more accurately, the stress per unit fluid density) is given by:

$$\tau_{ij} = -2\nu S_{ij} \tag{B2}$$

where τ_{ij} is the stress acting upon the resolved flow due to the subgrid scale eddies, and ν is the kinematic eddy viscosity. Once calculated, the stresses are used within the model to calculate resolved wind field tendencies:

$$\left(\frac{\partial u_i}{\partial t}\right)_{\text{eddy visc}} = -\sum_j \frac{\partial \tau_{ij}}{\partial x_j} \tag{B3}$$

The two schemes differ in their estimate of eddy viscosity. The 3D Smagorinsky scheme (Lilly, 1966; Smagorinsky, 1963) determines the viscosity from the strain rate tensor and from the static stability:

$$\nu_{\text{smag}} = \left(c_s l\right)^2 \left(\sqrt{\left(\sum_{i,j} S_{ij} S_{ij}\right) - \frac{N^2}{P_r}}\right) \tag{B4}$$

where c_s is a constant (taken to be 0.25), l is a length scale set by the model grid spacing, with $l = (\Delta x_i \Delta x_j \Delta x_k)^{1/3}$, N is the Brunt–Väisälä frequency:

$$N = \sqrt{\frac{g}{\theta}\frac{\partial \theta}{\partial z}} \tag{B5}$$

with g being the acceleration due to gravity, θ being the potential temperature, and z being the vertical distance ($z = x_k$ by convention) and P_r is the turbulent Prandtl number—the unitless ratio of the momentum diffusivity (i.e., the viscosity, ν) and the thermal diffusivity, α, $P_r \equiv \nu/\alpha$, which is taken to have a constant value of 1/3 (i.e., once the viscosity, ν, is calculated for either the Smagorinsky or SGS TKE scheme, the diffusivity is then simply the viscosity divided by the Prandtl number). The square root in Equation B4 is only taken when the value would not result in an imaginary number, otherwise it is set to zero. In order to maintain computational stability, a lower limit of 10^{-6} m^2/s is imposed for ν_{smag} when modeling the atmospheres of Earth and Mars.

The formulation of Equation B4 suggests that the eddy viscosity has two sources. The first source is the mechanical generation of turbulence due to the resolved fluid deformation and captured by the first term in the square toot in Equation B4. The second source corresponds to the thermal generation of turbulence and is due to buoyancy, which we identify as $-N^2$ in Equation B4. Note that the buoyancy can be negative (i.e., if the Brunt-Väisälä frequency is a real number and hence N^2 is positive), in this case the static stability of the air tends to damp turbulence. In the limit of strong static stability (strongly negative buoyancy), ν_{smag} is limited to its minimum value given in the prior paragraph.

The SGS TKE scheme is similar in its closure approach to 1.5 order (also known as 2.5 *level* closure) TKE PBL schemes used in meso- and synoptic scale modeling, except that diffusion is applied in all three spatial dimensions in the SGS scheme. The TKE SGS scheme carries a prognostic subgrid scale TKE (i.e., the value of the unresolved component of the total TKE) but the scheme does not prognose any other second order subgrid variables (the subgrid TKE is second order as it is the product of the subgrid scale wind perturbations with themselves, i.e., $\Sigma ui'ui'$ for $i = 1, 2, 3$). The viscosity is estimated from the subgrid scale TKE as (Lilly, 1966; Klemp & Wilhelmson, 1978):

$$\nu_{\text{tke}} = c_e l\left(\sqrt{\left(\text{TKE}_{\text{SGS}}\right)}\right) \tag{B6}$$

where c_e is a constant taken to be 0.15. The TKE_{SGS} is prognosed by calculation of TKE_{SGS} generation due to buoyancy and flow deformation, through local vertical and horizontal diffusion, and dissipative loss to heat. The TKE_{SGS} is advected by the resolved three-dimensional wind field. The TKE_{SGS} tendency is calculated as (Klemp & Wilhelmson, 1978):

$$\begin{aligned}\frac{\partial\left(\text{TKE}_{\text{SGS}}\right)}{\partial t} = &\left[-\nu_{\text{tke}}N^2 + \frac{g}{\theta}\frac{\text{HFX}}{\rho c_p}\right] + \left[\nu_{\text{tke}}\left(\sum_{i,j} S_{ij}S_{ij}\right) - \frac{u_*^2}{U}\left(\sum_{i=1}^{2} u_i S_{i3}\right)\right] \\ &+ \left[\sum_{i=1}^{3}\frac{\partial}{\partial x_i}\left(\nu_{\text{tke}}\frac{\partial\left(\text{TKE}_{\text{SGS}}\right)}{\partial x_i}\right)\right] - \frac{c_e}{l}\left(\text{TKE}_{\text{SGS}}\right)^{3/2}\end{aligned} \tag{B7}$$

where HFX is the heat flux from the surface into the atmosphere, which is either prescribed or calculated from the model surface layer parameterization (HFX is a two dimensional field representing the flux at the bottom boundary of the atmosphere), ρ is the air density, c_p is the atmospheric specific heat capacity at constant pressure, u_* is the frictional or drag velocity, which is either prescribed or calculated from the surface layer parameterization (like HFX, u_* is zero in all but the lowest model layer), and U is the magnitude of the total resolved horizontal wind speed. The surface layer scheme used in the microscale/LES simulations in this study is the same one used when the MarsWRF mesoscale or global model is run (i.e., the MRF/YSU PBL scheme Hong et al., 2006; Toigo et al., 2012). For LES, we only use the surface layer component (Jiménez et al., 2012), with the rest of the PBL scheme inactive.

Diffusion of tracers is assumed to operate with the same diffusivity as heat. TKE_{SGS} is a useful metric of the subgrid scale turbulence and although it is not explicitly used in the 3D Smagorinsky scheme, it can be inferred for the 3D Smagorinsky scheme from the viscosity, and hence from the deformation and static stability due to the equivalency of Equations B3 and B5 (note again that this is the inferred SGS TKE):

$$\text{TKE}_{\text{infer}} = \left(\frac{\nu_{\text{smag}}}{c_e l}\right)^2 = \left(\frac{c_s^2 l}{c_e}\right)^2\left[\left(\sum_{i,j} S_{ij}S_{ij}\right) - \frac{N^2}{P_r}\right] \tag{B8}$$

Data Availability Statement

The derived data from MarsWRF model output used in this study have been archived on data.mendeley.com (Wu, 2021). The MarsWRF code used to provide the results described here is not publicly available due to proprietary concerns. We therefore do not provide a link to a software repository. However, in this study, we fully describe the model, the setup for its use in this work, and provide archived model output as described above.

Acknowledgments
Z. Wu, T. Li, and J. Cui would like to acknowledge supports from the B-type Strategic Priority Program of the Chinese Academy of Sciences, Grant XDB41000000 and the National Natural Science Foundation of China through grants 42004147, 41525015, 41774186, and 41974175. M. I. Richardson, N. G. Heavens, C. E. Newman, and M. L. Witek would like to acknowledge support from NASA grant NNX-15AI33G to Hampton University. X. Zhang acknowledges support from NSF grant AST174092. C. Lee acknowledges support from the University of Toronto Faculty of Arts & Science Tri-Council Bridge Funding. O. Temel acknowledges support from the Research Foundation—Flanders (FWO). Resources supporting this work were provided by the NASA High-End Computing (HEC) Program through the NASA Advanced Supercomputing (NAS) Division at Ames Research Center.

References

Basu, S., Richardson, M. I., & Wilson, R. J. (2004). Simulation of the Martian dust cycle with the GFDL Mars GCM. *Journal of Geophysical Research*, *109*(E11). https://doi.org/10.1029/2004je002243

Cantor, B. A., James, P. B., Caplinger, M., & Wolff, M. J. (2001). Martian dust storms: 1999 Mars orbiter camera observations. *Journal of Geophysical Research*, *106*(E10), 23653–23687. https://doi.org/10.1029/2000je001310

Colaïtis, A., Spiga, A., Hourdin, F., Rio, C., Forget, F., & Millour, E. (2013). A thermal plume model for the Martian convective boundary layer. *Journal of Geophysical Research*, *118*(7), 1468–1487. https://doi.org/10.1002/jgre.20104

Conrath, B. J. (1975). Thermal structure of Martian atmosphere during dissipation of dust storm of 1971, *Icarus*, *24*(1), 36–46. https://doi.org/10.1016/0019-1035(75)90156-6

Couvreux, F., Hourdin, F., & Rio, C. (2009). Resolved versus parametrized boundary-layer plumes. Part I: A parametrization-oriented conditional sampling in large-eddy simulations. *Boundary-Layer Meteorology*, *134*(3), 441–458. https://doi.org/10.1007/s10546-009-9456-5

Daerden, F., Whiteway, J. A., Neary, L., Komguem, L., Lemmon, M. T., Heavens, N. G., et al. (2015). A solar escalator on Mars: Self-lifting of dust layers by radiative heating. *Geophysical Research Letters*, *42*, 7319–7326. https://doi.org/10.1002/2015GL064892

Fisher, J. A., Richardson, M. I., Newman, C. E., Szwast, M. A., Graf, C., Basu, S., et al. (2005). A survey of Martian dust devil activity using mars global surveyor Mars Orbiter Camera images. *Journal of Geophysical Research*, *110*. https://doi.org/10.1029/2003JE002165

Fuerstenau, S. D. (2006). Solar heating of suspended particles and the dynamics of Martian dust devils. *Geophysical Research Letters*, *33*, L19S03. https://doi.org/10.1029/2006GL026798

Gierasch, P., & Goody, R. (1968). A study of the thermal and dynamical structure of the Martian lower atmosphere. *Planetary and Space Science*, *16*, 615–646. https://doi.org/10.1016/0032-0633(68)90102-5

Goody, R., & Belton, M. J. S. (1967). A discussion of Martian atmospheric dynamics. *Planetary and Space Science*, *15*(2), 247–256. https://doi.org/10.1016/0032-0633(67)90193-6

Guzewich, S. D., Toigo, A. D., Kulowski, L., & Wang, H. (2015). Mars Orbiter Camera climatology of textured dust storms. *Icarus*, *258*, 1–13. https://doi.org/10.1016/j.icarus.2015.06.023

Guzewich, S. D., Toigo, A. D., Richardson, M. I., Newman, C. E., Talaat, E. R., Waugh, D. W., & McConnochie, T. H. (2013). The impact of a realistic vertical dust distribution on the simulation of the Martian general circulation. *Journal of Geophysical Research: Planets*, *118*(5), 980–993. https://doi.org/10.1002/jgre.20084

Guzewich, S. D., Toigo, A. D., & Wang, H. (2017). An investigation of dust storms observed with the Mars Color Imager. *Icarus*, *289*, 199–213. https://doi.org/10.1016/j.icarus.2017.02.020

Han, J., & Bretherton, C. S. (2019). TKE-based moist eddy-diffusivity mass-flux (EDMF) parameterization for vertical turbulent mixing. *Weather and Forecasting*, *34*(4), 869–886. https://doi.org/10.1175/waf-d-18-0146.1

Heavens, N. G. (2017). Textured dust storm activity in northeast Amazonis-southwest Arcadia, Mars: Phenomenology and dynamical interpretation. *Journal of the Atmospheric Sciences*, *74*(4), 1011–1037. https://doi.org/10.1175/jas-d-16-0211.1

Heavens, N. G., Richardson, M. I., Kleinböhl, A., Kass, D. M., McCleese, D. J., Abdou, W., et al. (2011). The vertical distribution of dust in the Martian atmosphere during northern spring and summer: Observations by the Mars climate sounder and analysis of zonal average vertical dust profiles. *Journal of Geophysical Research*, *116*(E4). https://doi.org/10.1029/2010je003691

Hinson, D. P., Pätzold, M., Tellmann, S., Häusler, B., & Tyler, G. L. (2008). The depth of the convective boundary layer on Mars. *Icarus*, *198*(1), 57–66. https://doi.org/10.1016/j.icarus.2008.07.003

Hinson, D. P., Tyler, D., Lewis, S. R., Pätzold, M., Tellmann, S., Häusler, B., & Tyler, G. L. (2019). The Martian daytime convective boundary layer: Results from radio occultation measurements and a mesoscale model. *Icarus*, *326*, 105–122. https://doi.org/10.1016/j.icarus.2019.02.028

Hong, S.-Y., Noh, Y., & Dudhia, J. (2006). A new vertical diffusion package with an explicit treatment of entrainment processes. *Monthly Weather Review*, *134*(9), 2318–2341. https://doi.org/10.1175/mwr3199.1

Inada, A., Richardsona, M. I., McConnochie, T. H., Strausberg, M. J., Wang, H., & Bell, J. F., III (2007). High-resolution atmospheric observations by the Mars Odyssey thermal emission imaging system. *Icarus*, *192*, 378–395. https://doi.org/10.1016/j.icarus.2007.07.020

Jiménez, P. A., Dudhia, J., González-Rouco, J. F., Navarro, J., Montávez, J. P., & García-Bustamante, E. (2012). A revised scheme for the WRF surface layer formulation. *Monthly Weather Review*, *140*(3), 898–918. https://doi.org/10.1175/mwr-d-11-00056.1

Kahre, M. A., Murphy, J. R., & Haberle, R. M. (2006). Modeling the Martian dust cycle and surface dust reservoirs with the NASA Ames general circulation model. *Journal of Geophysical Research: Planets*, *111*(E6). https://doi.org/10.1029/2005je002588

Kahre, M. A., Murphy, J. R., Newman, C. E., Wilson, R. J., Cantor, B. A., Lemmon, M. T., & Wolff, M. J. (2017). The Mars dust cycle. *The atmosphere and climate of Mars*, *18*, 295.

Kieffer, H. H., Christensen, P. R., Martin, T. Z., Miner, E. D., & Palluconi, F. D. (1976). Infrared thermal mapping of the Martian surface and atmosphere: Viking observation of diurnal and geometric observation. *Science*, *194*, 1346–1351. https://doi.org/10.1126/science.194.4271.1346

Klemp, J. B., & Wilhelmson, R. B. (1978). The simulation of three-dimensional convective storm dynamics. *Journal of the Atmospheric Sciences*, *35*(6), 1070–1096. https://doi.org/10.1175/1520-0469(1978)035<1070:tsotdc>2.0.co;2

Kulowski, L., Wang, H., & Toigo, A. D. (2017). The seasonal and spatial distribution of textured dust storms observed by Mars Global Surveyor Mars Orbiter Camera. *Advances in Space Research*, *59*, 715–721. https://doi.org/10.1016/j.asr.2016.10.028

Lee, C., Lawson, W. G., Richardson, M. I., Anderson, J. L., Collins, N., Hoar, T., & Mischna, M. (2011). Demonstration of ensemble data assimilation for Mars using DART, MarsWRF, and radiance observations from MGS TES. *Journal of Geophysical Research*, *116*(E11). https://doi.org/10.1029/2011je003815

Lee, C., Richardson, M. I., Newman, C. E., & Mischna, M. A. (2018). The sensitivity of solsticial pauses to atmospheric ice and dust in the MarsWRF general circulation model. *Icarus*, *311*, 23–34. https://doi.org/10.1016/j.icarus.2018.03.019

Lettau, K., & Lettau, H. H. (1978). Experimental and micro-meteorological field studies of dune migration. In H. H. Lettau, & K. Lettau (Eds.), *Exploring the world's driest climate* (Vol. 101, pp. 110–147). University of Wisconsin-Madison, Institute for Environmental studies, IES report.

Lilly, K. (1966). *The representation of small-scale turbulence in numerical simulation experiments*. IBM Form.

Määttänen, A., Fouchet, T., Forni, O., Forget, F., Savijärvi, H., Gondet, B., et al. (2009). A study of the properties of a local dust storm with Mars express OMEGA and PFS data. *Icarus*, *201*(2), 504–516. https://doi.org/10.1016/j.icarus.2009.01.024

Martinez, G. M., Newman, C. N., De Vicenteretortillo, A., Fischer, E., Renno, N. O., Richardson, M. I., et al. (2017). The modern near-surface Martian climate: A review of in-situ meteorological data from Viking to curiosity. *Space Science Reviews*, *212*(1), 295–338. https://doi.org/10.1007/s11214-017-0360-x

Michaels, T. I., & Rafkin, S. C. (2004). Large-eddy simulation of atmospheric convection on Mars. *Quarterly Journal of the Royal Meteorological Society*, *130*(599), 1251–1274. https://doi.org/10.1256/qj.02.169

Mischna, M. A., Lee, C., & Richardson, M. (2012). Development of a fast, accurate radiative transfer model for the Martian atmosphere, past and present. *Journal of Geophysical Research*, *117*(E10). https://doi.org/10.1029/2012je004110

Moeng, C.-H. (1984). A large-eddy-simulation model for the study of planetary boundary-layer turbulenc. *Journal of the Atmospheric Sciences*, *41*(13), 2051–2062. https://doi.org/10.1175/1520-0469(1984)041<2052:alesmf>2.0.co;2

Moeng, C. H., & Sullivan, P. P. (1994). A comparison of shear-and buoyancy-driven planetary boundary layer flows. *Journal of the Atmospheric Sciences*, *51*(7), 999–1022. https://doi.org/10.1175/1520-0469(1994)051<0999:acosab>2.0.co;2

Moeng, C.-H., & Wyngaard, J. C. (1989). Evaluation of turbulent transport and dissipation closures in second-order modeling. *Journal of the Atmospheric Sciences*, *46*, 2311–2330. https://doi.org/10.1175/1520-0469(1989)046<2311:eottad>2.0.co;2

Montmessin, F., Forget, F., Rannou, P., Cabane, M., & Haberle, R. M. (2004). Origin and role of water ice clouds in the Martian water cycle as inferred from a general circulation model. *Journal of Geophysical Research*, *109*(E10). https://doi.org/10.1029/2004je002284

Neakrase, L. D., Greeley, R., Iversen, J. D., Balme, M. R., & Eddlemon, E. E. (2006). Dust flux within dust devils: Preliminary laboratory simulations. *Geophysical Research Letters*, *33*(19). https://doi.org/10.1029/2006gl026810

Neakrase, L. D. V., Balme, M. R., Esposito, F., Kelling, T., Klose, M., Kok, J. F., et al. (2016). Particle lifting processes in dust devils. *Space Science Reviews*, *203*, 347–376. https://doi.org/10.1007/s11214-016-0296-6

Newman, C. E., Gómez-Elvira, J., Marin, M., Navarro, S., Torres, J., Richardson, M. I., et al. (2017). Winds measured by the Rover Environmental Monitoring Station (REMS) during the Mars Science Laboratory (MSL) rover's Bagnold Dunes Campaign and comparison with numerical modeling using MarsWRF. *Icarus*, *291*, 203–231. https://doi.org/10.1016/j.icarus.2016.12.016

Newman, C. E., Lewis, S. R., Read, P. L., & Forget, F. (2002). Modeling the Martian dust cycle, 1. Representations of dust transport processes. *Journal of Geophysical Research*, *107*(E12), 6-1–6-18. https://doi.org/10.1029/2002je001910

Newman, C. E., & Richardson, M. I. (2015). The impact of surface dust source exhaustion on the Martian dust cycle, dust storms and interannual variability, as simulated by the MarsWRF general circulation model. *Icarus*, *257*, 47–87. https://doi.org/10.1016/j.icarus.2015.03.030

Nishizawa, S., Odaka, M., Takahashi, Y. O., Sugiyama, K.-I., Nakajima, K., Ishiwatari, M., et al. (2016). Martian dust devil statistics from high-resolution large-eddy simulations. *Geophysical Research Letters*, *43*(9), 4180–4188. https://doi.org/10.1002/2016GL068896

Petrosyan, A., Galperin, B., Larsen, S. E., Lewis, S. R., Määttänen, A., Read, P. L., et al. (2011). The Martian atmospheric boundary layer. *Reviews of Geophysics*, *49*, RG3005. https://doi.org/10.1029/2010RG000351

Powers, J. G., Klemp, J. B., Skamarock, W. C., Davis, C. A., Dudhia, J., Gill, D. O., et al. (2017). The weather research and forecasting model: Overview, system efforts, and future directions. *Bulletin of the American Meteorological Society*, *98*(8), 1717–1737. https://doi.org/10.1175/bams-d-15-00308.1

Rafkin, S. C. R. (2009). A positive radiative-dynamic feedback mechanism for the maintenance and growth of Martian dust storms. *Journal of Geophysical Research*, *114*(E1). https://doi.org/10.1029/2008JE003217

Rafkin, S. C. R., Maria, M. R. V. S., & Michaels, T. I. (2002). Simulation of the atmospheric thermal circulation of a Martian volcano using a mesoscale numerical model. *Nature*, *419*(6908), 697–699. https://doi.org/10.1038/nature01114

Renno, N. O., Burkett, M. L., & Larkin, M. P. (1998). A simple thermodynamical theory for dust devils. *Journal of the Atmospheric Sciences*, *55*(21), 3244–3252. https://doi.org/10.1175/1520-0469(1998)055<3244:asttfd>2.0.co;2

Richardson, M. I., & Newman, C. E. (2018). On the relationship between surface pressure, terrain elevation, and air temperature. Part I: The large diurnal surface pressure range at Gale Crater, Mars and its origin due to lateral hydrostatic adjustment. *Planetary and Space Science*, *164*, 132–157. https://doi.org/10.1016/j.pss.2018.07.003

Richardson, M. I., Toigo, A. D., & Newman, C. E. (2007). PlanetWRF: A general purpose, local to global numerical model for planetary atmospheric and climate dynamics. *Journal of Geophysical Research*, *112*(E9). https://doi.org/10.1029/2006je002825

Savijarvi, H. (1999). A model study of the atmospheric boundary layer in the Mars pathfinder lander conditions. *Quarterly Journal of the Royal Meteorological Society*, *125*(554), 483–493. https://doi.org/10.1002/qj.49712555406

Savijärvi, H., Määttänen, A., Kauhanen, J., & Harri, A.-M. (2004). Mars Pathfinder: New data and new model simulations. *Quarterly Journal of the Royal Meteorological Society*, *130*(597), 669–683. https://doi.org/10.1256/qj.03.59

Siebesma, A. P., Soares, P. M. M., & Teixeira, J. (2007). A combined eddy-diffusivity mass-flux approach for the convective boundary layer. *Journal of the Atmospheric Sciences*, *64*, 1230–1248. https://doi.org/10.1175/JAS3888.1

Siebesma, A. P., & Teixeira, J. (2000). An advection-diffusion scheme for the convective boundary layer: Description and 1d-results. Paper presented 14th Symposium on Boundary Layers and Turbulence (Vol. 4.16). American Meteorological Society. Retrieved from https://ams.confex.com/ams/AugAspen/techprogram/paper_14840.htm

Smagorinsky, J. (1963). General circulation experiments with the primitive equations, *Monthly Weather Review*, *91*, 99–164. https://doi.org/10.1175/1520-0493(1963)091<0099:gcewtp>2.3.co;2

Spiga, A. (2019). The planetary boundary layer of Mars. In *Oxford Research Encyclopedia Planetary Science*. https://doi.org/10.1093/acrefore/9780190647926.013.130

Spiga, A., Faure, J., Madeleine, J.-B., Määttänen, A., & Forget, F. (2013). Rocket dust storms and detached dust layers in the Martian atmosphere. *Journal of Geophysical Research: Planets*, *118*(4), 746–767. https://doi.org/10.1002/jgre.20046

Spiga, A., & Forget, F. (2009). A new model to simulate the Martian mesoscale and microscale atmospheric circulation: Validation and first results. *Journal of Geophysical Research*, *114*(E2). https://doi.org/10.1029/2008je003242

Spiga, A., Forget, F., Lewis, S. R., & Hinson, D. P. (2010). Structure and dynamics of the convective boundary layer on Mars as inferred from large-eddy simulations and remote-sensing measurements. *Quarterly Journal of the Royal Meteorological Society*, *136*, 414–428. https://doi.org/10.1002/qj.563

Spiridonov, V., & Ćurić, M. (2021). Atmospheric boundary layer (ABL). In V. Spiridonov, & M. Ćurić (Eds.), *Fundamentals of meteorology* (pp. 219–228). Springer. https://doi.org/10.1007/978-3-030-52655-9_14

Stull, R. B. (1988). *An introduction to boundary layer meteorology*. Kluwer Academic Publisher.

Toigo, A. D., Lee, C., Newman, C. E., & Richardson, M. I. (2012). The impact of resolution on the dynamics of the Martian global atmosphere: Varying resolution studies with the MarsWRF GCM. *Icarus*, *221*(1), 276–288. https://doi.org/10.1016/j.icarus.2012.07.020

Toigo, A. D., Richardson, M. I., Ewald, S. P., & Gierasch, P. J. (2003). Numerical simulation of Martian dust devils. *Journal of Geophysical Research*, *108*(E6). https://doi.org/10.1029/2002je002002

Toigo, A. D., Richardson, M. I., Wang, H., Guzewich, S. D., & Newman, C. E. (2018). The cascade from local to global dust storms on Mars: Temporal and spatial thresholds on thermal and dynamical feedback. *Icarus*, *302*, 514–536. https://doi.org/10.1016/j.icarus.2017.11.032

Tomasko, M. G., Doose, L. R., Lemmon, M., Smith, P. H., & Wegryn, E. (1999). Properties of dust in the Martian atmosphere from the Imager on Mars Pathfinder. *Journal of Geophysical Research: Planets*, *104*(E4), 8987–9007. https://doi.org/10.1029/1998je900016

Wang, C., Forget, F., Bertrand, T., Spiga, A., Millour, E., & Navarro, T. (2018). Parameterization of rocket dust storms on Mars in the LMD Martian GCM: Modeling details and validation. *Journal of Geophysical Research: Planets*, *123*(4), 982–1000. https://doi.org/10.1002/2017je005255

Willis, G. E., & Deardorff, J. W. (1979). Laboratory observations of turbulent penetrative-convection planforms. *Journal of Geophysical Research*, *84*(C1), 295–302. https://doi.org/10.1029/jc084ic01p00295

Witek, M. L., Teixeira, J., & Matheou, G. (2011). An integrated TKE-based eddy diffusivity/mass flux boundary layer closure for the dry convective boundary layer. *Journal of the Atmospheric Sciences*, *68*(7), 1526–1540. https://doi.org/10.1175/2011jas3548.1

Wolff, M. J., & Clancy, R. T. (2003). Constraints on the size of Martian aerosols from thermal emission spectrometer observations. *Journal of Geophysical Research*, *108*(E9). https://doi.org/10.1029/2003je002057

Wu, Z. (2021). *Large eddy simulations of the dusty Martian convective boundary layer with MarsWRF*. Mendeley Data. https://doi.org/10.17632/4m96z77k4c.3

Wu, Z., Li, T., Zhang, X., Li, J., & Cui, J. (2020). Dust tides and rapid meridional motions in the Martian atmosphere during major dust storms. *Nature Communications*, *11*(1), 614. https://doi.org/10.1038/s41467-020-14510-x

Zhou, B., Simon, J. S., & Chow, F. K. (2014). The convective boundary layer in the terra incognita. *Journal of the Atmospheric Sciences*, *71*(7), 2545–2563, https://doi.org/10.1175/jas-d-13-0356.1